



저작자표시-비영리-변경금지 2.0 대한민국

이용자는 아래의 조건을 따르는 경우에 한하여 자유롭게

- 이 저작물을 복제, 배포, 전송, 전시, 공연 및 방송할 수 있습니다.

다음과 같은 조건을 따라야 합니다:



저작자표시. 귀하는 원저작자를 표시하여야 합니다.



비영리. 귀하는 이 저작물을 영리 목적으로 이용할 수 없습니다.



변경금지. 귀하는 이 저작물을 개작, 변형 또는 가공할 수 없습니다.

- 귀하는, 이 저작물의 재이용이나 배포의 경우, 이 저작물에 적용된 이용허락조건을 명확하게 나타내어야 합니다.
- 저작권자로부터 별도의 허가를 받으면 이러한 조건들은 적용되지 않습니다.

저작권법에 따른 이용자의 권리는 위의 내용에 의하여 영향을 받지 않습니다.

이것은 [이용허락규약\(Legal Code\)](#)을 이해하기 쉽게 요약한 것입니다.

[Disclaimer](#)

공학박사 학위논문

**Wire Rope Contact Model and Crane Control
Method for the Advanced Simulation and
Automation of Block Erection**

블록 탑재 자동화 및 시뮬레이션 고도화를 위한
와이어 로프 접촉 모델 및 크레인 제어 방법

2020년 2월

서울대학교 대학원
조선해양공학과
이 혜 원

Abstract

Wire Rope Contact Model and Crane Control Method for the Advanced Simulation and Automation of Block Erection

The block erection operations in the shipyards generally include block lifting, transporting, turnover, and lowering procedure. During the operation, there are potential risks such as interferences with wire ropes, overweight, collision, which can lead to severe accidents. To check such risks in advance, the physics-based simulations are often required before the actual operation. For this, detailed modeling of the equipment and the operation is necessary to reflect the real situation accurately, which is impossible with conventional modeling methods. Meanwhile, in the actual operation, the position and the orientation of the block should also be precisely controlled to avoid any risks. However, the actual operations are performed manually by the operator, and the cranes used for the erection of the block consist of sophisticated equipment, which makes them difficult to control.

In this study, the detailed modeling of the operation situation and the equipment are introduced for accurate simulation. Then, the control method of the crane is suggested for reliable and efficient control. Firstly, the block turnover operation by one floating crane and two crawler cranes is modeled considering the interferences between wire ropes and the block. For this, the interaction model between wire rope and the block, including

contact and friction, is suggested. Then, the contact forces exerted on the block are calculated. Secondly, the block lifting by the floating crane is analyzed considering the coupling motion of the floating crane and the mooring system. The interaction among the floating crane, the mooring line, and the seabed is introduced under the various sea condition. Lastly, the control of the gantry crane and the floating crane is performed for block lifting, transporting, and turnover operation. As the gantry crane and the floating crane consist of complicated equipment such as trolleys, booms, equalizers, and wire ropes, the control theory of the underactuated mechanical system is adopted.

For the verification, the comparison of the suggested interference model and the analytic solution is conducted. As the proposed model has been divided into three; contact model, friction model, and sliding model, each model is verified independently. Then, for the verification of the suggested mooring line model, the tension and the deflection of the mooring line are compared with that of the commercial software, OrcaFlex. The convergence test was also performed according to the number of the element, to find a proper number of the element of the mooring line. Lastly, the inverse dynamics model formulated in this study is verified by applying it to the dynamic model of gantry crane and check if the block tracks the desired trajectory.

To evaluate the effectiveness and applicability of the proposed methods, they were applied to the dynamic analysis of various kinds of block erection operations by using cranes. Three representative applications are provided, such as block turnover operation by floating crane and crawler cranes, block lifting operation by floating crane, and block erection operation by gantry crane and a floating crane. As a result, the proposed method could reflect the actual operation situation accurately, and the block was controlled to the desired trajectory. We conclude that the developed simulation and control methods are applicable to actual operation in ships and offshore structures.

Keywords: Block erection operation; Crane; Physics-based simulation; Multibody dynamics; Constraint-based wire rope; Interference; Frictional contact; Mooring system; Seabed interaction; Underactuated system; Control;

Student number: 2014-22655

Contents

Abstract.....	i
1. Introduction	1
1.1. Research backgrounds.....	1
1.2. Requirements for advanced simulation and control method.....	4
1.2.1. Requirements for multibody dynamics.....	4
1.2.2. Requirements for advanced simulation method	6
(1) Interference between wire rope and body during block turnover.....	6
(2) Coupled analysis of floating crane and mooring system.....	8
1.2.3. Requirements for automated crane control.....	10
1.3. State of the art	13
1.3.1. Block turnover simulation considering interference with wire rope	13
1.3.2. Dynamic analysis of the floating crane and mooring system.....	15
1.3.3. Control of cranes in shipyards.....	19
1.4. Research objectives and work scope.....	21
2. Theoretical backgrounds	22
2.1. Multibody dynamics	24
2.1.1. Multibody dynamics for rigid bodies	26
(1) Equations of motion for rigid bodies	26
(2) Discrete Euler-Lagrange equation.....	27
2.1.2. Flexible multibody dynamics for deformable bodies (1D beam element).....	31
(1) Kinematic description of a 1D beam element.....	31

(2) The strain energy of the 1D beam element	33
(3) External forces	37
(4) Equations of motion for 1D beam element	39
2.1.3. Kinematic constraints	43
(1) Kinematic constraints between rigid bodies.....	43
(2) Kinematic constraints between rigid and 1D flexible bodies	44
2.2. Modeling of the wire rope	47
2.2.1. Constraint-based wire rope model	47
(1) Stretching constraint.....	47
(2) Bending constraint.....	48
(3) Torsion constraint.....	49
(4) Wire rope with multiple segments	50
2.2.2. Mooring line model	53
(1) Catenary mooring line.....	53
(2) Initial position calculation.....	56
(3) External forces	60
2.3. Interaction between wire rope and body	64
2.3.1. Contact model	64
(1) Contact detection and node insertion.....	65
(2) Contact force calculation and node removal.....	71
2.3.2. Sliding model	74
2.3.3. Friction model	77
(1) Friction along the wire rope.....	78
(2) Friction along the edge.....	80
2.3.4. Case studies	81
(1) Tilted box dropping.....	81
(2) Body sliding along the wire rope.....	84
(3) Dropping of a body between wire ropes	85
2.4. Contact between mooring line and the seabed	87
2.4.1. Collision.....	87
(1) Non-interpenetration constraint.....	87
(2) Slope constraint.....	90
(3) Penetration depth.....	93
2.4.2. Friction	94

2.4.3. Case studies	95
(1) Mooring line under the current.....	95
(2) Mooring line with periodic motion	97
2.5. Control of the underactuated system	100
2.5.1. Underactuated mechanical system	100
2.5.2. Trajectory tracking control.....	102
(1) Servo constraint.....	102
(2) Motion planning.....	103
2.5.3. Dynamic equations.....	106
(1) Gantry crane.....	106
(2) Floating crane	119
2.5.4. Inverse dynamics control	126
(1) Inverse dynamics	126
(2) Index reduction method.....	127
(3) Feedforward control.....	130
(4) Feedback control.....	131
3. Verification	133
3.1. Verification of the interaction between wire rope and body	133
3.1.1. Verification of collision.....	133
3.1.2. Verification of sliding.....	136
3.1.3. Verification of friction	142
3.2. Verification of the mooring line model and interaction with the seabed	147
3.2.1. Convergence test	147
3.2.2. Comparison with the analytic solution	148
3.2.3. Verification of static analysis.....	150
3.2.4. Verification of dynamic analysis.....	152
3.3. Verification of the inverse dynamics of the underactuated system	155

4. Applications.....	157
4.1. Block turnover using floating crane and crawler cranes.	157
4.2. Block lifting by a floating crane	167
4.3. Crane control for block erection	172
4.3.1. Gantry crane control.....	172
4.3.2. Floating crane control	184
5. Conclusions and future works.....	194
5.1. Summary.....	194
5.2. Contributions (Originality).....	197
5.2.1. Theoretical contributions	197
5.2.2. Numerical contributions.....	197
5.2.3. Contributions for application	198
5.2.4. Other contributions.....	198
5.3. Future works.....	199
Reference	200
국문 초록	205

Figures

Figure 1-1. Process of the block erection operation.....	1
Figure 1-2. Necessity of the physics-based simulation.	2
Figure 1-3. Necessity of the automated control of the crane.	3
Figure 1-4. Bodies and constraints of the floating crane and the gantry crane.....	5
Figure 1-5. Interferences between the wire rope and the block.	7
Figure 1-6. Interaction of the seabed, mooring system, and the crane.....	9
Figure 1-7. Control of the gantry crane.....	11
Figure 1-8. Control of the floating crane.....	12
Figure 2-1. Overview of the requirements for advanced simulation and control methods.	23
Figure 2-2. Action integral J and the discretized action integral J_d	28
Figure 2-3. A kinematic description of an ANCF beam.	32
Figure 2-4. Stretching of the beam element.	34
Figure 2-5. Bending of the beam element.	36
Figure 2-6. Ball joint between the beam and rigid body.	45
Figure 2-7. Constraint-based wire rope with stretching.	48
Figure 2-8. Constraint-based wire rope with bending.....	49
Figure 2-9. Constraint-based wire rope with torsion.	50
Figure 2-10. The wire rope split into several segments.....	51
Figure 2-11. The wire rope split due to the contact with the body.....	52
Figure 2-12. The wire rope winding pulleys.	52
Figure 2-13. The configuration of a floating crane and the mooring system.	53
Figure 2-14. The configuration of a multibody system with multiple beam elements.....	54
Figure 2-15. The necessity of the calculation of the initial position.	56
Figure 2-16. Buckling of the mooring line at the initial stage.	57
Figure 2-17. The mooring line considering the length on the seabed.	58
Figure 2-18. The initial position of each beam element.	59
Figure 2-19. The distributed force exerted on a flexible beam element.....	61

Figure 2-20. The interaction between the wire rope and the body.	64
Figure 2-21. The contact process between the body and the wire rope.....	65
Figure 2-22. Broad phase and narrow phase for contact detection.	66
Figure 2-23. The intersection point of the triangle and the straight line.	68
Figure 2-24. Contact node insertion.....	70
Figure 2-25. The contact node calculation with the intersection points.....	70
Figure 2-26. Tangential plane and normal vector at the edge.....	71
Figure 2-27. Attachment and detachment of the body and the wire rope.....	73
Figure 2-28. Node removal of the wire rope.	74
Figure 2-29. Relative motion between the wire rope and the body.....	74
Figure 2-30. A body sliding along the wire rope.	75
Figure 2-31. A wire rope sliding along the edge of the body.....	76
Figure 2-32. A wire rope sliding to the other edges.	77
Figure 2-33. Static frictional force exerted on the body sliding along the wire rope.....	78
Figure 2-34. Kinetic frictional force exerted on the body sliding along the wire rope.	80
Figure 2-35. Contact node sliding along the edge with frictional force.....	81
Figure 2-36. Motion of a tilted box dropped on the wire rope.	82
Figure 2-37. Motion of a bunny dropped on the wire rope.	83
Figure 2-38. Motion of a box sliding along the wire rope.....	84
Figure 2-39. Motion of a sphere dropped between two wire ropes.	85
Figure 2-40. Motion of a bunny dropped between two wire ropes.....	86
Figure 2-41. Non-interpenetration constraint.	88
Figure 2-42. The configuration of the non-interpenetration constraint.....	88
Figure 2-43. Slope constraint.....	90
Figure 2-44. The configuration of the slope constraint.....	91
Figure 2-45. Comparison between the existing and suggested contact model.	93
Figure 2-46. Modified Coulomb friction model and the friction model with stick.....	94
Figure 2-47. Friction model for sticking.....	95
Figure 2-48. The motion of the mooring line under the current.	96
Figure 2-49. The tension of the mooring line under the current.....	97
Figure 2-50. The motion of the mooring line connected to the floating barge with periodic	

motion.....	98
Figure 2-51. Tension at the fairlead of the floating barge with periodic motion.	99
Figure 2-52. Two-dimensional inverted pendulum with different control inputs.	100
Figure 2-53. Examples of the underactuated crane system in shipyards.....	102
Figure 2-54. Application of the servo constraint.	103
Figure 2-55. Interpolation function for motion planning.	104
Figure 2-56. Rotational motion of the block from initial to final orientation.....	105
Figure 2-57. Configuration of the gantry crane system.....	107
Figure 2-58. Redundant coordinates of the crane system.....	109
Figure 2-59. Constraints of the crane system.	112
Figure 2-60. Wire rope vector between trolley and hook.....	113
Figure 2-61. The equalizers and slings of the gantry crane.....	116
Figure 2-62. Sling vector between hook and block.....	117
Figure 2-63. Configuration of the floating crane system.	120
Figure 2-64. Coordinates of the floating crane.	121
Figure 2-65. Wire rope vector between boom and block.	123
Figure 2-66. Diagram of the Gauss-Newton method.	130
Figure 2-67. Diagram for feedforward control.	130
Figure 2-68. Hybrid control merging feedforward and feedback control method.	131
Figure 3-1. Simple box-dropping simulation and analytic solution.	134
Figure 3-2. Result of the box-dropping simulation.....	135
Figure 3-3. The box model with different composition of mesh.	136
Figure 3-4. Dropping of an unbalanced block on two wire ropes.....	137
Figure 3-5. Motion of the box sliding on the wire rope.	138
Figure 3-6. Sliding of the wire rope along the edge of the box.	139
Figure 3-7. Position of the box dropped on two wire ropes.	140
Figure 3-8. Tension of the wire ropes during the dropping of an unbalanced box.	141
Figure 3-9. Simulation of the wire rope sliding along the edge with friction.....	142
Figure 3-10. Simulation result for validating the friction along the edge.	143
Figure 3-11. Simulation of the body sliding along the wire rope with friction.	144
Figure 3-12. Simulation result for validating the friction along the wire rope.	145

Figure 3-13. Acceleration of the boxes with different friction coefficients.....	146
Figure 3-14. Tension and the length on the seabed of the mooring line from the convergence test.	148
Figure 3-15. Profile of the mooring line compared with the analytic solution.	149
Figure 3-16. Profile of the mooring line with different axial stiffness.....	150
Figure 3-17. Simulation cases for the verification of static analysis with OrcaFlex.....	151
Figure 3-18. Test case for the verification of the dynamic analysis.	152
Figure 3-19. Result of the dynamic analysis compared with OrcaFlex.	154
Figure 3-20. Configuration of the control of the block using gantry crane.	155
Figure 3-21. The desired and actual trajectory of the block with feedforward control. .	156
Figure 4-1. Configuration of the block turnover operation using floating crane and crawler cranes.	157
Figure 4-2. Principal dimensions of the block.	158
Figure 4-3. Three phases of the block turnover operation.	159
Figure 4-4. Simulation result of case 2 in block turnover operation.	161
Figure 4-5. Interferences between the block and the wire ropes.	162
Figure 4-6. Sliding of the contact nodes in case 5.	163
Figure 4-7. Contact forces exerted on the contact nodes in cases 1 to 3.	164
Figure 4-8. Contact forces exerted on the contact nodes in cases 4 and 5.	165
Figure 4-9. Configuration of floating crane lifting a block and its mooring system.....	167
Figure 4-10. The motion of the floating crane under the irregular wave and current.	169
Figure 4-11. The tension of the mooring lines under the irregular wave and current.	170
Figure 4-12. Configuration of the gantry crane and the block.....	173
Figure 4-13. Gantry crane system with modeling uncertainties.	174
Figure 4-14. Motion of the block with modeling uncertainty.....	175
Figure 4-15. Control inputs of the gantry crane with modeling uncertainty.....	176
Figure 4-16. Length of the wire rope and the motion of the trolley with modeling uncertainty.	177
Figure 4-17. Gantry crane system with external disturbances.....	178
Figure 4-18. Irregular wind speed from the NPD spectrum.	179
Figure 4-19. Motion of the block with wind load.	181

Figure 4-20. Control inputs of the gantry crane with external disturbances.....	182
Figure 4-21. Length of the wire rope and the motion of the trolley with external disturbances.	183
Figure 4-22. Configuration of the floating crane and the block.	184
Figure 4-23. Desired trajectory of the block lifted by a floating crane.	185
Figure 4-24. Motion of the floating crane in case 1.....	186
Figure 4-25. Position of the block controlled by the floating crane in case 1.	187
Figure 4-26. Boom angle and the length of the wire ropes of the floating crane in case 1.	188
Figure 4-27. Total tension of the wire ropes connected to the block in case 1.	189
Figure 4-28. Motion of the floating crane in case 2.....	190
Figure 4-29. Position of the block controlled by the floating crane in case 2.	191
Figure 4-30. Boom angle and the length of the wire ropes of the floating crane in case 2.	192
Figure 4-31. Total tension of the wire ropes connected to the block in case 2.	193

Tables

Table 1-1. Related works for the interference during block turnover operation.	14
Table 1-2. Related works for the coupled analysis of the multibody system and mooring system.	17
Table 1-3. Related works for the control of the cranes in shipyards.	19
Table 2-1. Joint types and the allowable relative motion.	43
Table 3-1. Comparison of the box-dropping simulation with the analytic solution.	135
Table 3-2. Properties of the mooring line for the convergence test.	147
Table 3-3. Properties of the mooring line for the comparison with the analytic solution.	148
Table 3-4. Result of the static analysis compared with OrcaFlex.	152
Table 3-5. Properties of the barge and the mooring line for dynamic analysis.	153
Table 4-1. Properties of the floating crane in block turnover operation.	158
Table 4-2. Test cases for the block turnover operation.	160
Table 4-3. Properties of the barge and the mooring line for block lifting by a floating crane.	167
Table 4-4. Simulation cases with different environmental conditions.	168
Table 4-5. Properties of the floating crane for the control of block erection.	185
Table 4-6. Test cases of the block erection control by a floating crane.	186
Table 5-1. Verification examples for suggested models.	196

1. Introduction

1.1. Research backgrounds

In the shipyards, ships and offshore structures are constructed by joining several blocks, which are basic units for shipbuilding. The joining process is called block erection operation. As shown in Figure 1-1, the block erection operation generally includes block lifting, transporting, and lowering procedure, and block turnover operation which rotates the blocks is often included.



Figure 1-1. Process of the block erection operation.

During the actual operation, there are possible dangers due to the environmental loads such as wind and wave, which induce the dynamic motion of the block and equipment. The dynamic motion of the block can cause unpredictable tensions of the wire ropes, and loads on lugs, which are the structures on the block to connect the wire rope, as presented in Figure 1-2. They can lead to serious accidents or failure during the operation. Therefore, the physics-based simulation for the production of ships and offshore structures are required to check the potential risks in advance. To improve the safety and efficiency of the process, detailed modeling of the operation is necessary, which reflects actual situations accurately.

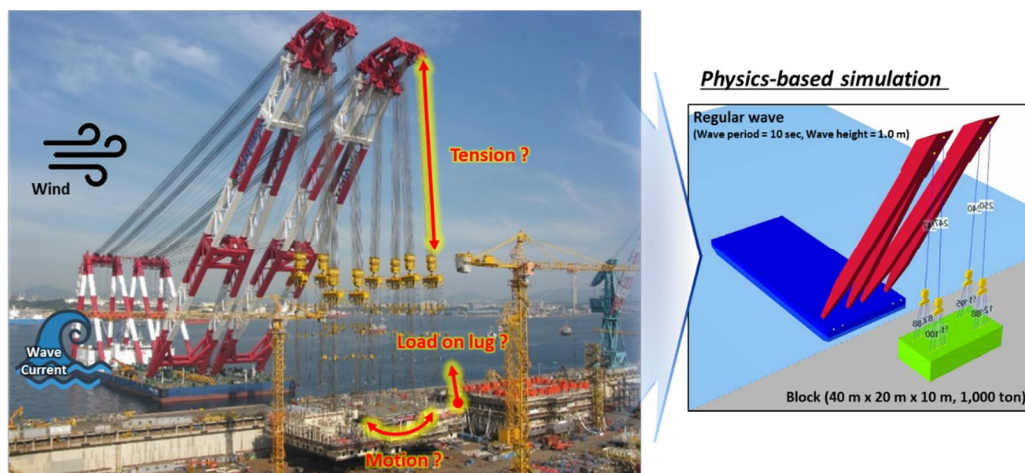


Figure 1-2. Necessity of the physics-based simulation.

Meanwhile, the block erection operations are commonly conducted by using gantry crane or floating crane with block loaders and equalizers. In the block erection operation, the position and orientation of the block should be precisely controlled to avoid collision with other structures and to be located in an accurate position. However, the block is

generally connected to the cranes through crane girder, trolleys, booms, hooks, equalizers, and wire ropes. Therefore, the crane cannot control the motion of the block directly, and the external loads should be taken into account when controlling the motion of the block. In the shipyard, the actual operation is controlled manually by the operators and outside workers (Figure 1-3), and the accuracy and the efficiency of the operation cannot be ensured accordingly. Furthermore, for the physics-based simulation, it is hard to simulate the actual control operation method, and there are some limitations in applying the traditional control method. Therefore, for a more safe and reliable operation, the automated control of the cranes are required.



Figure 1-3. Necessity of the automated control of the crane.

1.2. Requirements for advanced simulation and control method

In this section, the details about the requirements for the advanced simulation and the automated control method is presented.

1.2.1. Requirements for multibody dynamics

The block erection operations are generally conducted by cranes such as gantry crane and a floating crane. For the physics-based simulation, the dynamic of the cranes consist of sophisticated equipment should be analyzed considering the external loads. The cranes are multibody systems, which have multiple bodies connected with joints. Figure 1-4 shows the configuration of the floating crane and the gantry crane. The floating crane consists of the crane barge, boom, and mooring system, which are connected by hinge joints and ball joints. If the environmental loads such as wave and current are exerted to the crane, the induced motion of the barge, boom, and mooring system can all affect the motion of the connected block. The gantry crane consists of crane girder and upper and lower trolleys. The crane girder can slide along the ground, and the trolleys can move on the crane girder in the same way. They can be modeled as slider joints in the multibody system.

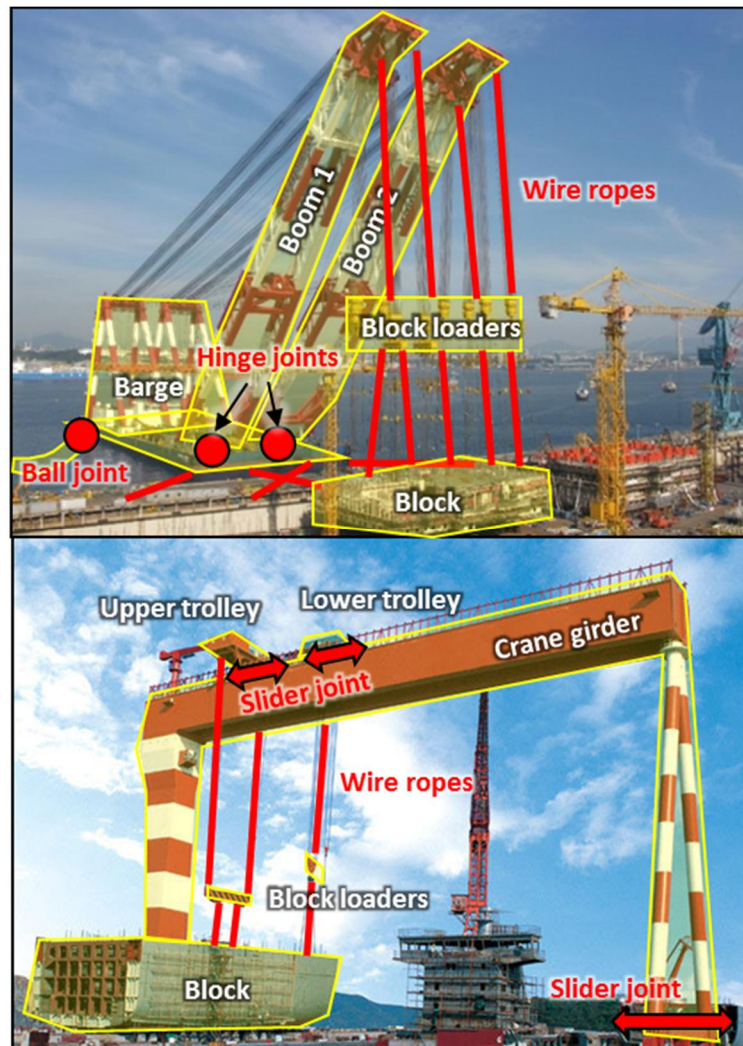


Figure 1-4. Bodies and constraints of the floating crane and the gantry crane.

Additionally, the block is connected to each crane by wire ropes and block loaders. The block loader consists of a hook and equalizer, which are connected with a hinge joint. Consequently, the whole system for block erection can be regarded as a multibody system. To analyze the motion of the multibody system, the multibody system dynamics formulation is required.

1.2.2. Requirements for advanced simulation method

For the reliable physics-based simulation, the advanced simulation method is required to reflect actual operation, which is impossible with conventional methods. This section describes the requirements for the detailed modeling of the block erection operation.

(1) Interference between wire rope and body during block turnover

For the convenient production and outfitting operation, several blocks are constructed rotated or upside down. The block turnover process is often necessary in block erection operation, in case of the rotation of such block is required. The block turnover is conducted by one crane, or by co-work of several cranes to rotate the block upside down. In such a procedure, the interferences between the wire rope and the body often occur (Figure 1-5).

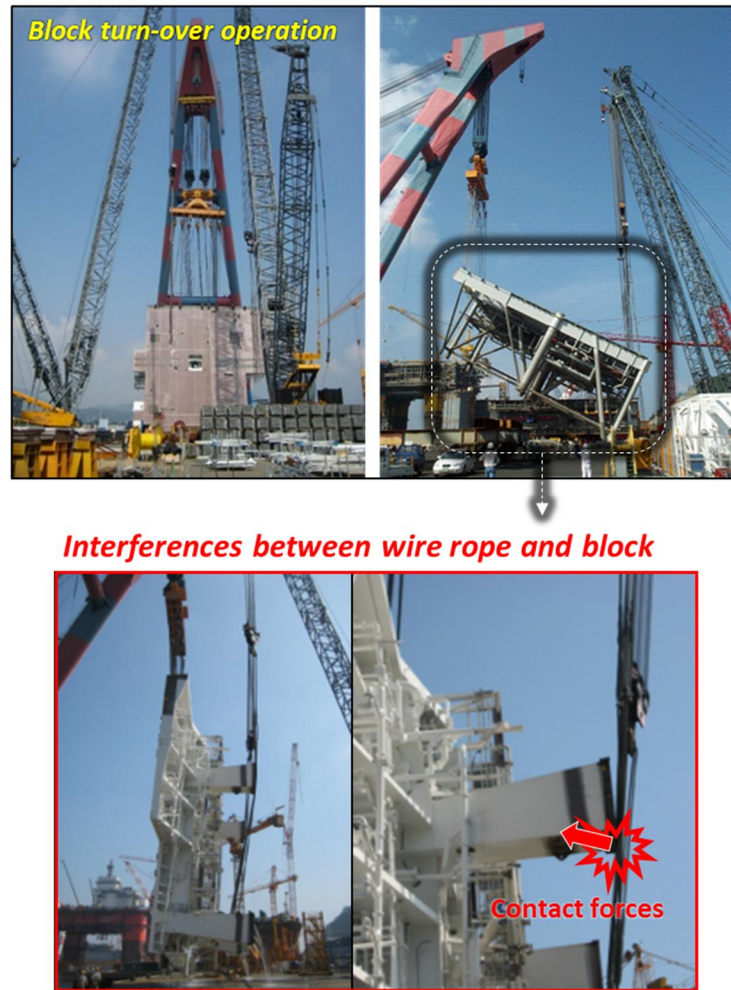


Figure 1-5. Interferences between the wire rope and the block.

The interferences between the wire rope and the block can cause severe problems. Firstly, as the block with outfitting has intricate structures, it is hard to predict the interferences with wire ropes. Moreover, the motion of the block induced by the interferences is almost unpredictable even when there are environmental loads. Secondly, the forces exerted by the contact with the wire rope can damage the vulnerable structures in the block.

Generally, if the interferences are expected, the design of the lug arrangement of the block or the operation method is changed to avoid them. If the interferences are unavoidable, the structural analysis of the block should be performed to check the structural stability in advance. If the block cannot support the exerted force, the structural reinforcement is necessary. With these reasons, the detection of the interferences and the analysis of exerted force due to interferences should be performed in the physics-based simulation of block turnover operation.

(2) Coupled analysis of floating crane and mooring system

The mooring system is a system including the mooring line and anchor, which maintains the position of the floating bodies in the ocean under the environmental loads. The floating crane keeps its position by the mooring system during the operation. The mooring lines are connected to the barge of the floating crane at the fairleads and fixed to the quay or the seabed through the anchor. The dynamic analysis of the mooring line is very important to predict the motion response and dynamic loads of the floating crane. However, there are only a few types of research deal with the coupled analysis of the mooring system and the multibody system. The dynamic motion of the mooring line itself should be analyzed integrated with not only the dynamic motion of the crane barge but also other bodies connected to the barge. Therefore, the integrated analysis of the mooring system and the multibody system dynamics is required for reasonable simulation.



Interaction of seabed-mooring-crane system

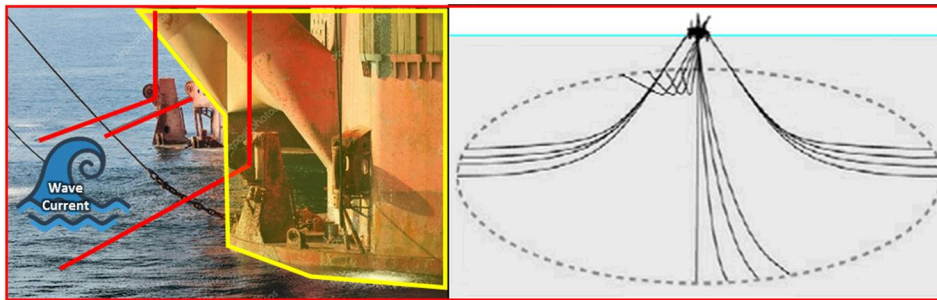


Figure 1-6. Interaction of the seabed, mooring system, and the crane.

As depicted in Figure 1-6, the catenary mooring line is laid down to the seabed. A catenary mooring system, which generally connects the floating crane to the seabed, keeps the position of the crane with its own weight and the friction along the seabed. The friction between the mooring line and the seabed plays an important role in keeping the position of the floating body. Therefore, the interaction of the seabed and the mooring system should also be analyzed. Consequently, the integrated motion of the seabed, mooring system, and floating crane induced by the wave and current needs to be considered.

1.2.3. Requirements for automated crane control

The control of the crane is required to erect the block to a certain position and orientation. The operators conduct the control operation manually by controlling the motion of the crane girder, trolleys, booms, and the length of the wire ropes. The precise control of each equipment depends on the experience of the operators and the direction of the outside workers. Furthermore, as the environmental loads are exerted on the crane and the block, the operation is conducted slowly for safety. Thus, the automated control method is required to give the guideline to the operators and to automate the actual operation in the future. The traditional control methods such as PID (Proportional-Integral-Differential) control have been used for the simulation of the operation so far, but there are some limitations for the control of the cranes for block erection operation.

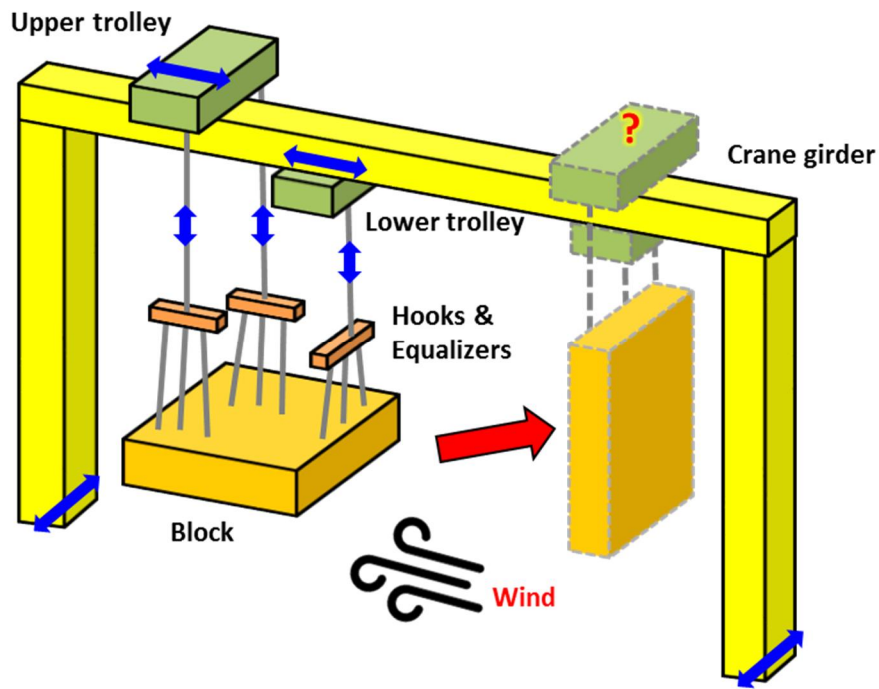


Figure 1-7. Control of the gantry crane.

A gantry crane, also known as Goliath crane, is one of the representative cranes in the shipyards. It consists of crane leg and girder, upper and lower trolleys, hooks, equalizers, and wire ropes. In block erection operation, the gantry crane controls the motion of the block through the translational motion of the crane girder and two trolleys, and the hoisting of the winch of the wire ropes (Figure 1-7). As the wind load can induce the motion of the block, the motion of the trolleys and the wire ropes should be precisely controlled to make sure the block tracks the desired trajectory properly.

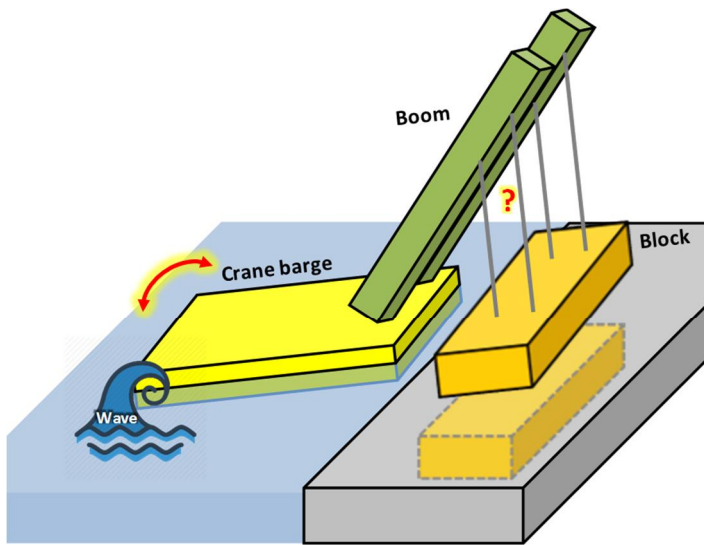


Figure 1-8. Control of the floating crane.

The floating crane is one of the most commonly used cranes in the shipyards to lift and transport the block on the quay or the dock. The operators of the floating crane rotate two booms and winch the wire ropes connected to the block for block lifting and transporting. Unlike the gantry crane, the external loads from wave and current directly affect the floating crane itself (Figure 1-8). It induces the dynamic motion of the block, which makes the erection operation difficult. Thus, the automated control method considering the motion of the floating crane itself, which is a drive system, is required.

1.3. State of the art

1.3.1. Block turnover simulation considering interference with wire rope

Servin et al. [1] modeled the wire rope with the number of the lumped mass combined with distance constraints to consider the interference between wire rope and body. The frictional contact nodes are inserted in the wire rope when collides with the body, and the stick and slide friction along the wire rope and the edges are provided at each node. The suggested wire rope model was included in the augmented formulation of the multibody system. However, as it considered the relationship between each lumped mass in one wire rope as constraint, the size of the matrix is relatively big. As numerous wire ropes are generally used in operation in the shipyards, the model is not appropriate for the block erection operation. Moreover, the static friction model has some limitations that the stick-slip transitions are not realized properly.

In the ship and offshore engineering field, a number of researchers analyzed the block turnover operation using various cranes. However, there are only a few works considered the interferences between the wire rope and the block during the operation. Ha et al. [2] performed block turnover simulation by using two gantry cranes. The event-based scenario was created for the simulation, and the recursive formulation is used for the motion analysis of the system. However, the wire ropes were modeled with incompressible springs, and the interference with the block was not considered. The block turnover operation using one floating crane and two crawler cranes were simulated by Li et al. [3]. In this work, the collaborative simulation was performed by integrating the dynamic analysis, virtual reality, and control devices. In the same way, the contact of the

block and the wire rope was ignored.

There are several kinds of research considering the interferences between the wire ropes and the block. Jo et al. [4] suggested a wire rope model consists of lumped mass with elastic bodies connecting them. Then, the contact node was inserted into the wire rope model after calculating the position of the interference. Then, the frictional force along the edge was calculated. However, the friction along the wire rope was neglected, and the geometry of the block is simplified in the application. Lee et al. [5] performed the block turnover simulation using gantry crane considering interferences. The wire rope was modeled as constraint, and included in the Discrete Euler-Lagrange Equation, DELE, for the analysis with the multibody system. However, there are some limitations that the frictional forces between the body and the wire ropes are not considered. The wire rope can also be modeled as an elastic body, and the interferences can be considered as collisions between bodies. Nevertheless, the simulation cost will be enormous as there are many wire ropes in operation, and the procedures for collision detection between bodies are costly.

Table 1-1. Related works for the interference during block turnover operation.

	Multibody formulation	Wire rope model	Wire interference		Environmental loads	Applications
			Contact	Friction		
Servin et al.	Augmented formulation	Lumped mass combined with distance constraint	O	O	X	Load transporting
Ha et al.	Recursive formulation	Incompressible spring	X	X	X	Block turnover operation
Li et al.	DELE	Constraint-based wire rope	X	X	X	Block turnover operation
Jo et al.	Augmented formulation	Lumped mass with the elastic body	O	Δ (friction along the	X	Block turnover operation

				edge)		
Lee at al.	DELE (Discrete Euler-Lagrange Equation)	Constraint-based wire rope	O	X	O (wind)	Block turnover operation
This study	DELE	Constraint-based wire rope	O	O	O (wave)	Block turnover operation

In this study, we modeled the wire rope using constraints to consider the interferences, which is cost-effective for the simulation. Then, the contact and friction model was suggested considering the sliding along the wire ropes and the edges of the block. For this, the static and kinetic friction model was introduced for the reasonable stick-slip transition. Finally, the motion analysis was performed using Discrete Euler Lagrange Equation including the wire rope constraints. For the application, the block turnover operation by floating crane and crawler cranes was simulated considering wave load exerting on the floating barge.

1.3.2. Dynamic analysis of the floating crane and mooring system

The floating barges are connected to the seabed by a mooring system to maintain the position. The modeling of the mooring system plays an important role in the prediction of the responses of the floating unit and the loads on the mooring lines. There exist two types of the mooring system, depending on the environmental condition and the purpose of the units: taut mooring and catenary mooring. Taut mooring is generally modeled as a massless wire rope, as it uses the tension of the line rather than its weight. In contrast, the catenary mooring exerts forces based on its weight. The three primary model types for the mooring analysis are as follows: analytic catenary model, lumped-mass model, and finite element model [6].

The analytic catenary model is a quasi-static model that calculates the profile and the tension of the mooring line using analytical equations. This model is based on the assumption that the mooring line is at the static equilibrium state. The static approach assumes that the acceleration and velocity of the mooring line are ignorable, and the system already reached the steady-state. Faltinsen [7] introduced the analytic approach for the calculation of the mooring force. It is a popular, simple approach for the modeling of the mooring system, but it is hampered by some usage restrictions. The main disadvantage is that the hydrodynamic and inertial forces on the mooring line cannot be considered.

Another approach to model the mooring line is the lumped-mass approach. The lumped-mass approach concentrates the mass and hydrodynamic forces at the nodes that are located at the end of each mooring-line segment. Then, the nodes are connected by massless springs that can simulate the stretching of the mooring line. This approach was first suggested by Walton and Polacheck [8] and was later developed by Khan and Ansari [9] in three dimensions. However, for a system with multiple mooring lines, the lumped-mass approach appears as an inopportune approach for programming [10].

With these disadvantages, the finite element method (FEM) has become more popular. A FEM for the mooring system that considers the elastic deformation was presented by Bathe [11]. It was developed to the elastic-rod finite element model with linear elasticity, and the elastic-rod method has been widely used in the analysis of slender components such as the mooring line, riser, and pipeline.

The dynamic analysis of the mooring system is one of the active areas under investigation in ship and offshore engineering field. There are various researches on the dynamic analysis of the moored floating bodies. Part of them is presented in Table 1-2.

Related explanations of these works are also illustrated in Lee et al. [12].

Table 1-2. Related works for the coupled analysis of the multibody system and mooring system.

	Mooring line model	Beam shape function	Application to multibody	Stretching	Bending	Contact with seabed	Simulation cost
Tang et al.	Linear spring	-	O	O	X	X	Very low
Ham et al.	Analytic solution		O	X	X	O	Low
Kim et al.	FEM	1st order	X	O	X	O (Spring on the node)	Very high
Kim et al.	FEM	1st order	X	O	O	O (Spring on the node)	Very high
Ku et al.	FEM	1st order	O	O	X	O (Spring on the node)	Very high
This study	FEM	3rd order	O	O	O	O (Constraint)	high

Tang et al. [13] analyzed the dynamic behavior of the dual-pontoon floating structure using a massless spring model for the mooring lines. As the catenary mooring line exerts forces based on its weight, the massless spring model has some limitations for the exact analysis. Nevertheless, it has some advantages that it can reduce simulation cost and be easily adapted to a multibody system as an external force.

Ham et al. [14] developed the safety evaluation program for the mega-floating crane based on the multibody dynamics. For the taut mooring line, which keeps the position of the floating body by its tension from stretching, the massless spring model is adopted. In contrast, the analytic catenary model is used for the catenary mooring line, which only provides tension by its weight, and neglects elasticity. Moreover, the model can only consider the static load on the mooring line. Here, the contact between the mooring line and the seabed is considered for the analytic catenary model.

Several studies performed mooring line analysis based on FEM as it can consider the dynamics of the mooring line, its elasticity, and weight altogether. Kim et al. [15] analyzed the behavior of the catenary mooring line, considering elastic deformation employing FEM. The researchers then compared the motion of the floating body and the mooring line to the linear spring model. Gutiérrez-Romero et al. [16] presented the non-linear dynamic FEM mooring model to analyze the response of a moored floating wind turbine. For the interaction with the seabed, a spring-damper system is used. Then, the suggested model is validated against several experimental results. Despite the reliable simulation result of the FEM based mooring model, most studies are not applicable to the multibody system, as the floating body was considered as a single body.

Based on this necessity, Jeong et al. [17] suggested the FEM-based mooring line model, which applies to the multibody system. He used linear beam elements to model the mooring line considering stretching. To reflect the contact with the seabed, the linear springs are adopted that connect each node of the mooring line and the seabed. In this research, the equation of motion of the floating body and the mooring line was solved separately. Therefore, an iteration process is required to match the boundary condition between the floating body and the mooring line at every time interval, which leads to very high simulation costs.

There are several commercial software such as MOSES and OrcaFlex, which provide a motion analysis system for the floating body and the mooring system based on FEM. However, the floating body connected to the mooring lines is considered as a single body, not a multibody system. Therefore, the analysis of the multibody system such as a floating crane, cannot be performed integrated with the FEM-based mooring line model using commercial software.

In this study, the FEM-based mooring line model was adopted applicable to the multibody system. The 3rd-order shape function was used for the beam elements, which considers both stretching and bending of the mooring line. The contact with the seabed was then realized using the constraints. Finally, the equations of motion of the floating body and the mooring lines were formulated together for a fully coupled analysis.

1.3.3. Control of cranes in shipyards

Table 1-3 shows related works deals with the control of the cranes mostly used in shipyards, such as a gantry crane and a floating crane. The control purpose can be divided into three; trajectory tracking, step value tracking, and set-point regulation. The trajectory tracking is to control the target to track the desired trajectory, which is the function of time. The step value tracking is to control to track the target value, regardless of the trajectory and time. The set-point regulation is to maintain a certain position or the orientation of the target.

Table 1-3. Related works for the control of the cranes in shipyards.

Authors	Target crane model	Control inputs	Control method	Control purpose	Application
Liu and Guo (2012) [1]	2D Gantry crane (3-DOF)	1 trolley and a wire rope	Sliding mode control (SMC) with fuzzy tuning algorithm	Trajectory tracking	Lifting and transporting of a payload (point mass)
Bakhtiari-Nejad et al. (2013) [2]	2D Gantry crane (2-DOF)	1 trolley	Optimal feedback control	Step value tracking	Transporting of a payload (point mass)
Mehra et al. (2014) [3]	Gantry crane (4-DOF)	1 trolley, girder	Passivity based control (PBC)	Set-point regulation	Payload (point mass) sway control
Sun et al. (2015) [4]	Floating crane (with heave compensation)	Wire rope	Adaptive genetic algorithm	Set-point regulation	Payload (point mass) lifting with constant velocity

	system)		(GA) PID control		
Nam et al. (2018) [5]	Floating crane	Wire rope	Proportional control	Set-point regulation	Roll and pitch control during dual lifting
This study	Gantry crane (6-DOF), and floating crane	2 trolleys, girder, and wire rope	Hybrid control (feedforward + feedback control)	Trajectory tracking	Trajectory tracking control during lifting, transporting and turnover operation

Most researches for the control of the gantry crane simplified the crane model to have four or lower degrees of freedom. Additionally, the block was modeled as a point mass mostly, which ignores the orientation of the body. Liu and Guo [18] performed trajectory-tracking control of a payload using a two-dimensional gantry crane with one trolley and a wire rope. The sliding mode control with a fuzzy tuning algorithm was applied for the control. Bakhtiari-Nejad et al. [19] controlled a payload using a two-dimensional gantry crane by the translational motion of the trolley, with constant length of the wire rope. In this work, the step value tracking was performed by using the optimal feedback control method. A set-point regulation control of the block was conducted by Mehra et al. [20], using passivity based control. The sway motion of the block was controlled during lifting by gantry crane with four degrees of freedom.

For the control of the floating crane, a set-point regulation control was mainly performed while lifting the block. Sun et al. [21] performed payload lifting with constant velocity using floating crane under environmental loads. The research focused on the heave compensation system in the floating crane, which can affect the control of the block. Nam et al. [22] considered the block as a three-dimensional body with rotation and controlled the roll and pitch motion of the block during lifting. In their study, two different floating cranes collaborated for the lifting of one block. Therefore, this study

mainly gave priority to the coupled motion of two floating cranes for dual lifting.

In this study, we selected two target cranes, which are a gantry crane with six degrees of freedom and a floating crane. The trajectory-tracking control of the block was performed during lifting, transporting, and turnover operations. For the reliable control of the block, a hybrid control, which combines feedforward and feedback control method was adopted.

1.4. Research objectives and work scope

The research objective is to develop advanced simulation methods to solve the problems that have not been analyzed in previous studies, and an automated control method of cranes for block erection operation. The work scopes of this study are as follows.

- 1) Analysis of the interferences between the block and the wire ropes for block turnover simulation
- 2) Integrated simulation of the crane barge and the mooring system considering interaction with the mooring line and the seabed
- 3) Construction of the inverse dynamics solver for the automated control of cranes in the shipyard

2. Theoretical backgrounds

Figure 2-1 shows the overall requirements of the advanced simulation and automated crane control method for block erection operation. The first layer, simulation core, formulates the equation of motion considering rigid and flexible multibody dynamics. Then, the motion of each body is calculated as a result. The simulation components layer includes force and constraint calculation, which is necessary to formulate the equations of motion. The interferences between the wire rope and the body or collision between bodies are also simulation components, and the resultant forces are calculated. For the control of the crane, the inverse dynamics solver is required to calculate the control forces exerted on the crane. With the external forces and constraints obtained from the inverse dynamics solver and the simulation components, the simulation core constructs the final form of the equation of motion for a given system. Finally, it is applied to various erection operation including several types of equipment in shipyards such as crane and equalizer.

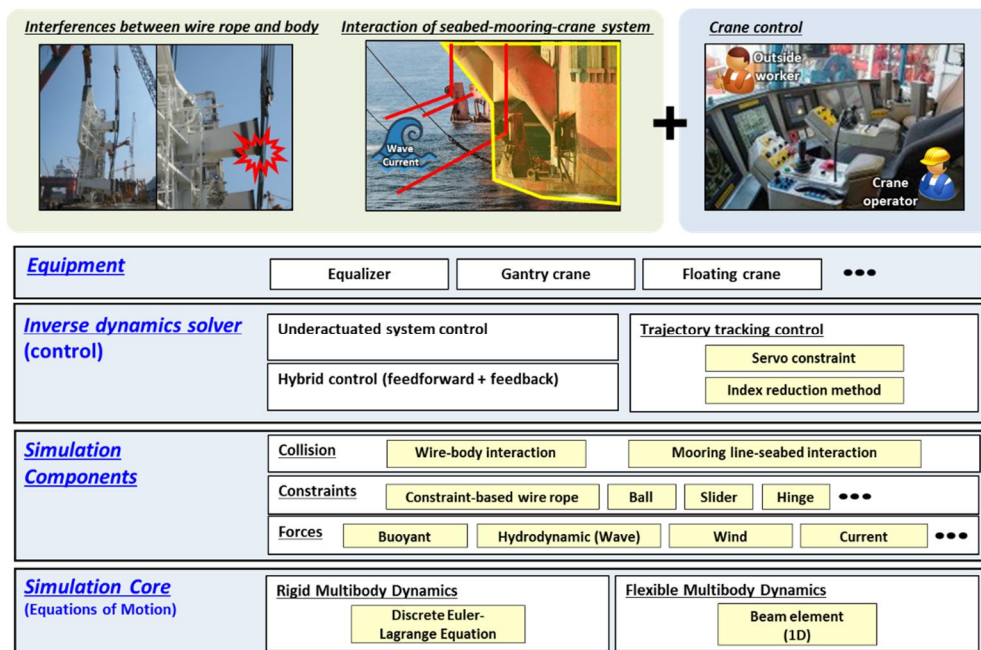


Figure 2-1. Overview of the requirements for advanced simulation and control methods.

In this section, the theoretical backgrounds for the advanced simulation and automated crane control method are introduced. In section 2.1, the multibody dynamics for rigid and flexible bodies for the simulation core is derived. Section 2.2 presents the modeling of the wire ropes, constraint-based wire rope, and the flexible body. Then, the collision analysis of each wire rope model with the rigid body is described in section 2.3. Finally, section 2.4 explains the inverse dynamics solver for the control of the crane.

2.1. Multibody dynamics

Multibody dynamics is a discipline describing the dynamic behavior of mechanical systems that consist of multiple bodies connected via joints, which represents a kinematic constraint between two bodies. The body can be divided into a rigid and flexible body, depending on whether it is deformable. The multibody system composed of both rigid and flexible bodies is called a flexible multibody system.

The following nomenclature has been used in this section:

D_i : Partial differential operator

\mathbf{g} : Constraint equations

\mathbf{G} : Constraint Jacobians

g_j : j th constraint equation

h : Timestep

J : The action integral of Lagrangian L , which is related to the expenditure of energy during motion

L : Lagrangian, defined as kinetic energy (T) – potential energy (V)

\mathbf{M} : Mass matrix

\mathbf{q} : Generalized coordinates of position and orientation

\mathbf{q}_k : Position and orientation at time t_0+kh

\mathbf{r}_P : The position vector from the origin O to point P

\mathbf{S} : Shape function of beam

T : Kinetic energy

t : Time

t_0 : Start time of the motion

t_n : End time of the motion

V : Potential energy

δ : Change in the value of the function resulting from a change of all arguments except for the time

ε : Error term

λ : Lagrange multipliers

$$\bar{\lambda} : \frac{\bar{\lambda}_{k+1}}{h^2} = \frac{\lambda_{k-1} + 2\lambda_k + \lambda_{k+1}}{4}, \quad \bar{\lambda}_{k+1} = \frac{\bar{\lambda}_{k+1}}{h}$$

λ_j : Lagrange multiplier for j th constraint

τ : Dissipation rate parameter

$$\Gamma : \Gamma = 1 / \left(1 + \frac{4\tau}{h} \right)$$

2.1.1. Multibody dynamics for rigid bodies

(1) Equations of motion for rigid bodies

The multibody system is a system that consists of joint-connected multiple bodies. To analyze the dynamic behavior of the multibody system, the equations of the motion containing the multiple bodies and the joints should be constructed and solved with external forces. In a multibody system, the joints restrain the motion of each body by exerting constraint forces to the connected bodies. Therefore, it is very difficult to apply the Newton-Euler equation, which is the basic form for the dynamic analysis, directly. The changed form of the equation of motion is then suggested including the constraint equations describing the joints.

To describe the motion of the multibody system, various formulations have previously been suggested. Since the step of the finding of the constraint forces regarding multibody dynamics is very complicated, Shabana [23] divided the formulations into two according to the constraint-force consideration method, as follows: embedding technique [24], [25] and augmented formulation [24], [26] [25]. Besides, Lacoursière [27] formulated the Discrete Euler–Lagrange (DEL) equation that is derived from the discretization of the Euler–Lagrange equation. Other alternative approaches for the formulation of the motion equations of the multibody system are recursive methods [28], [29], [30], [31].

In this study, a Discrete Euler-Lagrange Equation (DELE) formulated by Lacoursière [27] is applied, which is proven numerically stable for the case of linear holonomic constraints. The DEL equation is derived from the discretization step of the Euler–Lagrange equation, together with the application of the finite differential method. Wendlandt et al. [32], Marsden et al. [33], and Lew [34] explained the derivation of the DELE in their works, and Ham[35] dealt with more detailed process to obtain the DELE.

In this study, the brief process to derive the DELE is described.

(2) Discrete Euler-Lagrange equation

According to Hamilton's principle, in a system, the motion of the body follows the trajectory that minimizes the expenditure of energy during the motion at time $t_0 \sim t_n$. The action integral J is defined as

$$J = \int_{t_0}^{t_N} L dt = \int_{t_0}^{t_N} (T - V) dt . \quad (1)$$

Following Hamilton's principle, the trajectory of the body should satisfy the following equation.

$$\delta J = \delta \int_{t_0}^{t_N} L dt = 0 \quad (2)$$

As the Lagrangian L is the function of the generalized coordinate q and \dot{q} , equation (2) then yields

$$\frac{d}{dt} \left(\frac{\partial L}{\partial \dot{\mathbf{q}}} \right) - \frac{\partial L}{\partial \mathbf{q}} = 0, \quad (3)$$

which is known as the Euler-Lagrange equation.

Meanwhile, in the discrete Euler-Lagrange equation, the action integral J , which is

represented as a blue area in Figure 2-2 (a), is approximately calculated with the sum of small rectangular areas shown in Figure 2-2 (b), which are divided according to the time step h between the end time t_n and start time t_0 .

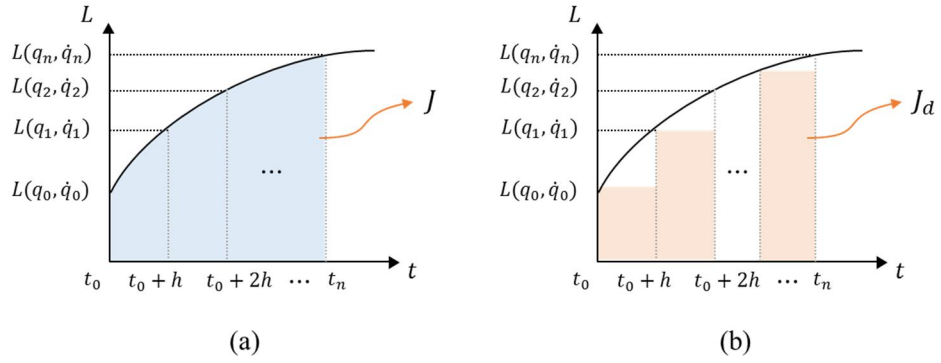


Figure 2-2. Action integral J and the discretized action integral J_d .

Approximate $\dot{\mathbf{q}}_{k+1}$ to $\frac{\mathbf{q}_{k+1} - \mathbf{q}_k}{h}$, where q_k is the position and orientation at time $t_0 + kh$.

The discretized action integral is expressed as

$$J_d = \sum_{k=0}^{N-1} L_d(\mathbf{q}_k, \mathbf{q}_{k+1}, h). \quad (4)$$

Following equation (2), the next equation is obtained:

$$\begin{aligned}
\delta J_d &= \sum_{k=0}^{N-1} \delta L_d(\mathbf{q}_k, \mathbf{q}_{k+1}, h) \\
&= \sum_{k=1}^{N-1} [D_2 L_d(\mathbf{q}_{k-1}, \mathbf{q}_k, h) + D_1 L_d(\mathbf{q}_k, \mathbf{q}_{k+1}, h)] \delta \mathbf{q}_k = 0
\end{aligned} \tag{5}$$

The equation above then yields the discrete Euler-Lagrange equation (DELE) as follows:

$$D_2 L_d(\mathbf{q}_{k-1}, \mathbf{q}_k, h) + D_1 L_d(\mathbf{q}_k, \mathbf{q}_{k+1}, h) = 0 \tag{6}$$

Meanwhile, as the bodies in the multibody system are connected with wire ropes or joints, the appropriate constraint equations should be included in their equations of motion above. Constraints are kinematic restrictions on the variables in the system. The modified Lagrangian including the constraints can be written as

$$\bar{L} = L + L_C = L + \sum_{j=1}^m \lambda_j g_j(\mathbf{q}) = L + \boldsymbol{\lambda}^T \mathbf{g}(\mathbf{q}). \tag{7}$$

With the modified Lagrangian, the DELE with constraints can be obtained directly:

$$\left(\mathbf{G}_k^T = \begin{bmatrix} \frac{\partial \mathbf{g}_1}{\partial \mathbf{q}_k} & \frac{\partial \mathbf{g}_2}{\partial \mathbf{q}_k} & \dots & \frac{\partial \mathbf{g}_m}{\partial \mathbf{q}_k} \end{bmatrix}^T \right). \tag{8}$$

Approximating the modified Lagrangian, and the constraints using the Stömer-Verlet method [36], [37] and the Taylor series expansion, the DELE with matrix form is obtained as follows:

$$\begin{bmatrix} \mathbf{M} & -\mathbf{G}_k^T \\ \mathbf{G}_k & 0 \end{bmatrix} \begin{bmatrix} \mathbf{q}_{k+1} \\ h^2 \boldsymbol{\lambda}_k \end{bmatrix} = \begin{bmatrix} \mathbf{M}(2\mathbf{q}_k - \mathbf{q}_{k-1}) - h^2 \frac{\partial V}{\partial \mathbf{q}_k} \\ -\mathbf{g}(\mathbf{q}_k) + \mathbf{G}_k \mathbf{q}_k \end{bmatrix}. \quad (9)$$

However, the equation above has an ill-posed problem, as the constraint equations can be violated due to the error of approximation. Applying the regularization method introduced by Baumgarte [38], and Eich and Hanke [39]], the regularized DELE is as follows:

$$\begin{bmatrix} \mathbf{M} & -\mathbf{G}_k^T \\ \mathbf{G}_k & \frac{\boldsymbol{\varepsilon}}{h^2} \end{bmatrix} \begin{bmatrix} \mathbf{q}_{k+1} \\ h^2 \boldsymbol{\lambda}_k \end{bmatrix} = \begin{bmatrix} \mathbf{M}(2\mathbf{q}_k - \mathbf{q}_{k-1}) - h^2 \frac{\partial V}{\partial \mathbf{q}_k} \\ -\mathbf{g}(\mathbf{q}_k) + \mathbf{G}_k \mathbf{q}_k \end{bmatrix}. \quad (10)$$

The error term $\boldsymbol{\varepsilon}$ is related to the violence of the constraint, and indicates the strength of the constraint. With smaller $\boldsymbol{\varepsilon}$, the constraints become stronger. The equations with the form of velocity are then derived as follows:

$$\begin{bmatrix} \mathbf{M} & -\mathbf{G}_k^T \\ \mathbf{G}_k & \Gamma \frac{4\boldsymbol{\varepsilon}}{h^2} \end{bmatrix} \begin{bmatrix} \mathbf{v}_{k+1} \\ \boldsymbol{\lambda}_{k+1} \end{bmatrix} = \begin{bmatrix} \mathbf{M}\mathbf{v}_k - h \frac{\partial V}{\partial \mathbf{q}_k} + h\mathbf{f}(\mathbf{q}_k, \mathbf{v}_k) \\ -\frac{4\Gamma}{h} \mathbf{g}_k + \Gamma \mathbf{G}_k \mathbf{v}_k \end{bmatrix}. \quad (11)$$

2.1.2. Flexible multibody dynamics for deformable bodies (1D beam element)

The flexible multibody system, which is composed of both rigid and flexible bodies, can be divided into linearly and nonlinearly, elastic multibody systems [40]. For the linearly elastic system, it is assumed that the strain of the flexible bodies is very small and that it has a linear relationship with the displacement at all times. For the nonlinearly elastic system, the strain can become large, or there can be a nonlinear relationship with displacement. The mechanical system that contains the mooring lines can be regarded as a nonlinearly elastic multibody system, as the flexible bodies have large deformations. For this purpose, the Absolute Nodal Coordinate Formulation (ANCF), well described by Berzeri and Shabana [41] and Shabana [42] is adopted for the flexible body. The following description to obtain equations of motion of the beam element is also well explained in Ham [43].

(1) Kinematic description of a 1D beam element

The mooring line can be modeled as a set of ANCF beam elements connected to the floating barge. In ANCF, the nodal coordinates and slope are defined in the inertial frame. These nodal coordinates are used with a global shape function that has a complete set of rigid body modes. Therefore, the global position vector of an arbitrary point on the beam can be described by using the global shape function \mathbf{S} and the absolute nodal coordinates

e. To describe an ANCF beam, information is required about the displacement and the slope at each node, as shown in Figure 2-3.

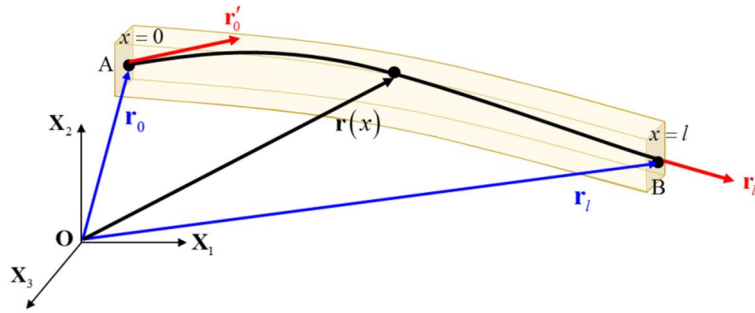


Figure 2-3. A kinematic description of an ANCF beam.

Absolute nodal coordinates (\mathbf{e}) can be expressed by displacement node vectors ($\mathbf{r}_0, \mathbf{r}_1$) and slope vectors ($\mathbf{r}'_0, \mathbf{r}'_1$) at displacement nodes. Finally, the global position vector of an arbitrary point on the beam can be written as

$$\mathbf{r}(x) = \mathbf{S}\mathbf{e} = \begin{bmatrix} s_1\mathbf{I} & s_2\mathbf{I} & s_3\mathbf{I} & s_4\mathbf{I} \end{bmatrix} \begin{bmatrix} \mathbf{r}_0 \\ \mathbf{r}'_0 \\ \mathbf{r}_1 \\ \mathbf{r}'_1 \end{bmatrix}, (0 \leq x \leq l). \quad (12)$$

\mathbf{I} is a 3×3 identity matrix, and s_i ($i = 1, 2, 3,$ and 4) are Hermite-shape functions defined as

$$\begin{aligned}
s_1(\xi) &= 1 - 3\xi^2 + 2\xi^3 \\
s_2(\xi) &= l(\xi - 2\xi^2 + \xi^3) \\
s_3(\xi) &= 3\xi^2 - 2\xi^3 \\
s_4(\xi) &= l(\xi^3 - \xi^2)
\end{aligned} \tag{13}$$

where $\xi = x/l$; l is the length of the beam, and x is the parameter of the arc length of the beam defined from 0 to 1. The Hermite-shape function interpolates the beam as a cubic polynomial. Other details about ANCF, including the mass matrix \mathbf{M} and the stiffness matrix \mathbf{K}_l , \mathbf{K}_t due to the longitudinal and the transversal deformations, are well described by Berzeri and Shabana [41].

(2) The strain energy of the 1D beam element

The one-dimensional beam element stores the strain energy in the body when deformed. The deformation of a one-dimensional beam element can be divided into longitudinal stretching and bending. The equations of motion for the flexible multibody is then can be obtained by including the internal strain energy to the DELE (11).

① Axial strain energy

The axial strain energy is the energy stored due to the longitudinal stretching. To stretch the beam element for small displacement δ as Figure 2-4, the exerted force can be calculated by the relationship between the strain ε and the stress σ as follows.

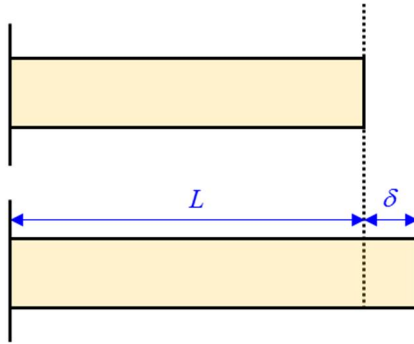


Figure 2-4. Stretching of the beam element.

$$\begin{aligned}
 \sigma &= E\varepsilon \\
 \frac{F}{A} &= E \frac{\delta}{L}, \\
 F &= \frac{EA}{L} \delta
 \end{aligned} \tag{14}$$

where E is Young's modulus, A is the sectional area, and L is the initial length of the beam element. With large deformation, the Green-Lagrange strain is calculated as follows.

$$\varepsilon = \frac{\delta}{L} + \frac{1}{2} \left(\frac{\delta}{L} \right)^2 \tag{15}$$

Then, the work done by the force can be obtained by the integral of the displacement.

$$\begin{aligned}
U &= \int_0^{\delta} \frac{EA}{L} x dx \\
&= \int_0^{\varepsilon_a} EA\varepsilon(Ld\varepsilon), \quad \left(\begin{array}{l} \varepsilon = \frac{x}{L} \\ \varepsilon_a = \frac{\delta}{L} \end{array} \right) \\
&= \frac{1}{2} EAL\varepsilon_a^2
\end{aligned} \tag{16}$$

The strain energy density, which is a strain energy per unit volume, can be calculated as the following equation.

$$u = \frac{U}{AL} = \frac{1}{2} E\varepsilon_a^2 = \frac{1}{2} \sigma\varepsilon_a \tag{17}$$

The strain energy can vary along the bar as Young's modulus and the cross-sectional area changes. Therefore, the total strain energy stored inside the beam element can be expressed by the integral form

$$\begin{aligned}
U_a &= \iiint_V u dV \\
&= \int_0^L \frac{1}{2} E\varepsilon_a^2 (A dx) \\
&= \frac{1}{2} \int_0^L EA\varepsilon_a^2 dx
\end{aligned} \tag{18}$$

② Bending strain energy

The bending strain energy is the energy stored due to bending. If a beam element is

bent, we can obtain the radius ρ of the curve of the neutral surface of the beam element (Figure 2-5).

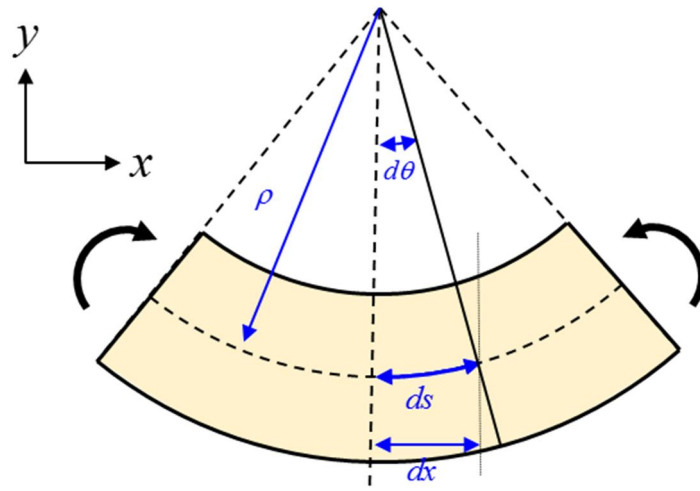


Figure 2-5. Bending of the beam element.

Then, the bending strain ε_b at y from the neutral surface can be calculated as follows by the definition.

$$\varepsilon_b = \frac{(\rho - y) \cdot d\theta - \rho d\theta}{ds} = -y \frac{d\theta}{ds} = -\frac{y}{\rho} \quad (19)$$

In the same way with the axial strain energy, the bending strain energy density is as follows.

$$u = \frac{1}{2} E \varepsilon_b^2 = \frac{1}{2} E \left(-\frac{y}{\rho} \right)^2 = \frac{1}{2} E \frac{y^2}{\rho^2} = \frac{1}{2} E \kappa^2 y^2 \quad (20)$$

κ is curvature, which is inverse of the radius ρ . The total strain energy due to bending can be obtained by the integral along the length.

$$\begin{aligned} U_b &= \iiint_V u \, dV = \int_0^L \left(\iint u \, dA \right) dx = \int_0^L \left(\iint \frac{1}{2} E \kappa^2 y^2 \, dA \right) dx \\ &= \frac{1}{2} \int_0^L E \left(\iint y^2 \, dA \right) \kappa^2 dx = \frac{1}{2} \int_0^L EI \kappa^2 dx \end{aligned} \quad (21)$$

I is the second moment of inertia of the section area.

(3) External forces

The external force acts at the arbitrary point \mathbf{r} on the 1D beam element is calculated as follows. Let the external force expressed by the inertial frame is \mathbf{F}_{nc}^e . Then, from the non-conservative generalized external force, the force at the point is obtained as

$$\mathbf{Q}_{nc} = \left(\frac{\partial \mathbf{r}}{\partial \mathbf{q}} \right)^T \mathbf{F}_{nc}^e = \left(\frac{\partial (\mathbf{S} \mathbf{q})}{\partial \mathbf{q}} \right)^T \mathbf{F}_{nc}^e = \mathbf{S}^T \mathbf{F}_{nc}^e \quad (22)$$

If constantly distributed force is exerted on the beam element, the integration is required to obtain the external force. With distributed force per volume \mathbf{w} , the generalized force is calculated as follows.

$$\begin{aligned}
\mathbf{Q}_{nc} &= \iiint_V \mathbf{S}^T \mathbf{w}^e dV \\
&= \int_0^l \mathbf{S}^T \mathbf{w}^e A dx \\
&= \int_0^1 \mathbf{S}^T \mathbf{w}^e A l d\xi \\
&= A l \left(\int_0^1 \mathbf{S}^T d\xi \right) \mathbf{w}^e \\
&= A l \bar{\mathbf{S}}^T \mathbf{w}^e
\end{aligned} \tag{23}$$

A damping force acting on the beam is proportional to the velocity, which varies along with the beam element. The damping force $d\mathbf{F}_{damping}^e$ at x ($0 < x < l$) is obtained as follows, with damping coefficient C_d .

$$\begin{aligned}
d\mathbf{F}_{damping}^e &= -C_d \cdot \mathbf{v}(x) dx \\
&= -C_d \cdot \{ \mathbf{S}(\xi) dx \} \dot{\mathbf{q}}(t) \\
&= -C_d l \cdot \{ \mathbf{S}(\xi) d\xi \} \dot{\mathbf{q}}(t)
\end{aligned} \tag{24}$$

The generalized damping force integrated over the beam yields the following equation.

$$\begin{aligned}
\mathbf{Q}_{damping} &= \int_0^1 d\mathbf{Q}_{damping} \\
&= \int_0^1 \left(\frac{\partial \mathbf{r}}{\partial \mathbf{q}} \right)^T d\mathbf{F}_{damping}^e \\
&= \int_0^1 \mathbf{S}^T d\mathbf{F}_{damping}^e \\
&= \int_0^1 \mathbf{S}^T \cdot [-C_d l \cdot \{\mathbf{S}(\xi) d\xi\} \dot{\mathbf{q}}(t)] \\
&= -C_d l \left(\int_0^1 \mathbf{S}^T \mathbf{S} d\xi \right) \dot{\mathbf{q}}(t) \\
&= -C_d l \bar{\mathbf{S}} \dot{\mathbf{q}}(t)
\end{aligned} \tag{25}$$

(4) Equations of motion for 1D beam element

For the equations of motion for the beam element, we adopt ANCF. From the kinematic description and the strain energy of the beam element derived previously, the equations of motion of the ANCF beam are obtained.

Firstly, the kinetic energy T of the beam element is obtained as follows with mass matrix \mathbf{M} , which is expressed with the mass of the beam element m and the shape function s_i ($i = 1, 2, 3,$ and 4) defined in Eq. (13).

$$\frac{d}{dt} \left(\frac{\partial T}{\partial \dot{\mathbf{q}}} \right) = \mathbf{M} \ddot{\mathbf{q}} \tag{26}$$

$$\begin{aligned}
\mathbf{M} &= m \int_0^l \begin{bmatrix} s_1 \mathbf{I} \\ s_2 \mathbf{I} \\ s_3 \mathbf{I} \\ s_4 \mathbf{I} \end{bmatrix} [s_1 \mathbf{I} \quad s_2 \mathbf{I} \quad s_3 \mathbf{I} \quad s_4 \mathbf{I}] d\xi \\
&= m \begin{bmatrix} \frac{13}{35} \mathbf{I} & \frac{11l}{210} \mathbf{I} & \frac{9}{70} \mathbf{I} & -\frac{13l}{420} \mathbf{I} \\ & \frac{l^2}{105} \mathbf{I} & \frac{13l}{420} \mathbf{I} & -\frac{l^2}{140} \mathbf{I} \\ & & \frac{13}{35} \mathbf{I} & -\frac{11l}{210} \mathbf{I} \\ \text{sym.} & & & \frac{l^2}{105} \mathbf{I} \end{bmatrix} \quad (27)
\end{aligned}$$

The strain energy of the beam element due to stretching and bending is as follows.

$$\begin{aligned}
U &= U_a + U_b \\
&= \frac{1}{2} \int_0^l EA \varepsilon_a^2 dx + \frac{1}{2} \int_0^l EI \kappa^2 dx \quad (28)
\end{aligned}$$

U_a is axial strain energy, U_b is bending strain energy, and ε_a and κ are a longitudinal strain and a curvature, which are a function of $\mathbf{r}(x)$. By definition, the axial longitudinal strain and curvature can be obtained as follows.

$$\begin{aligned}
\varepsilon_a &= \frac{d\mathbf{u}}{dx} = \frac{d}{dx}(\mathbf{r}(x) - \mathbf{r}(0)) \\
&= \frac{d\mathbf{r}}{dx} = \frac{d\mathbf{S}}{dx} \mathbf{q} \\
&= \frac{d\mathbf{S}}{d\xi} \frac{d\xi}{dx} \mathbf{q} = \frac{d\mathbf{S}}{d\xi} \frac{\mathbf{q}}{l} = \mathbf{S}_{,\xi} \frac{\mathbf{q}}{l} \\
\kappa &= \frac{d^2\mathbf{r}}{dx^2} = \frac{d^2\mathbf{S}}{dx^2} \mathbf{q} = \frac{d^2\mathbf{S}}{d\xi^2} \frac{\mathbf{q}}{l^2} = \mathbf{S}_{,\xi\xi} \frac{\mathbf{q}}{l^2}
\end{aligned} \tag{29}$$

Then, by substituting U_a and U_b into the Euler-Lagrange equation (Eq. (3)), we obtain the following result.

$$\begin{aligned}
\frac{\partial U_a}{\partial \mathbf{q}} &= \frac{EA}{l} \bar{\mathbf{S}}_{,\xi} \mathbf{q} = \mathbf{K}_a \mathbf{q} \\
\frac{\partial U_b}{\partial \mathbf{q}} &= \frac{EI}{l^3} \bar{\mathbf{S}}_{,\xi\xi\xi} \mathbf{q} = \mathbf{K}_b \mathbf{q}
\end{aligned} \tag{30}$$

\mathbf{K}_a is the axial stiffness matrix, and \mathbf{K}_b is the bending stiffness matrix. The axial and bending stiffness matrices can be calculated explicitly as follows. For the application to the large deformation, we used the Green-Lagrange strain defined in Eq. (33) to derive the stiffness matrix.

$$\mathbf{K}_a = \frac{EA}{l} \begin{bmatrix} \mathbf{AI} & \mathbf{BI} & -\mathbf{AI} & \mathbf{CI} \\ & \mathbf{DI} & -\mathbf{BI} & \mathbf{EI} \\ & & \mathbf{AI} & \mathbf{CI} \\ \text{sym.} & & & \mathbf{FI} \end{bmatrix} \tag{31}$$

$$\begin{aligned}
A &= \frac{3}{70l^2} (a^2 + b^2 - 14l^2 - 6a_x d_x - 6b_x d_x - 6a_y d_y - 6b_y d_y - 6a_z d_z - 6b_z d_z + 24d^2) \\
B &= \frac{1}{280l} (b^2 - a^2 + 2a_x b_x + 2a_y b_y + 2a_z b_z - 14l^2 - 24a_x d_x - 24a_y d_y - 24a_z d_z + 36d^2) \\
C &= \frac{1}{280l} (a^2 - b^2 + 2a_x b_x + 2a_y b_y + 2a_z b_z - 14l^2 - 24b_x d_x - 24b_y d_y - 24b_z d_z + 36d^2) \\
D &= \frac{1}{420} (12a^2 + b^2 - 3a_x b_x - 3a_y b_y - 3a_z b_z - 28l^2 + 3a_x d_x + 3a_y d_y + 3a_z d_z - 3b_x d_x - 3b_y d_y - 3b_z d_z + 18d^2) \\
E &= \frac{-1}{840} (3a^2 + 3b^2 - 4a_x b_x - 4a_y b_y - 4a_z b_z - 14l^2 + 6a_x d_x + 6a_y d_y + 6a_z d_z + 6b_x d_x + 6b_y d_y + 6b_z d_z) \\
F &= \frac{1}{420} (a^2 + 12b^2 - 3a_x b_x - 3a_y b_y - 3a_z b_z - 28l^2 - 3a_x d_x - 3a_y d_y - 3a_z d_z + 3b_x d_x + 3b_y d_y + 3b_z d_z + 18d^2) \\
&\left(\begin{array}{l} d_x = e_7 - e_1, \quad a_x = le_4, \quad a_y = le_5, \quad a_z = le_6, \quad a = \sqrt{a_x^2 + a_y^2 + a_z^2} \\ d_y = e_8 - e_2, \quad b_x = le_{10}, \quad b_y = le_{11}, \quad b_z = le_{12}, \quad b = \sqrt{b_x^2 + b_y^2 + b_z^2} \\ d_z = e_9 - e_3, \quad d = \sqrt{d_x^2 + d_y^2 + d_z^2} \end{array} \right)
\end{aligned}$$

$$\mathbf{K}_b = \frac{EI}{l^3} \begin{bmatrix} 12\mathbf{I} & 6\mathbf{I} & -12\mathbf{I} & 6\mathbf{I} \\ & 4l^2\mathbf{I} & -6\mathbf{I} & 2l^2\mathbf{I} \\ & & 12\mathbf{I} & -6\mathbf{I} \\ sym. & & & 4l^2\mathbf{I} \end{bmatrix} \quad (32)$$

$$\begin{aligned}
\varepsilon_a &= \frac{1}{2} \left(\left(\frac{d\mathbf{u}}{dx} \right)^T \left(\frac{d\mathbf{u}}{dx} \right) - 1 \right) \\
&= \frac{1}{2} \left(\left(\frac{d\mathbf{r}}{dx} \right)^T \left(\frac{d\mathbf{r}}{dx} \right) - 1 \right) \\
&= \frac{1}{2} \left(\left(\frac{d\mathbf{S}}{dx} \mathbf{q} \right)^T \left(\frac{d\mathbf{S}}{dx} \mathbf{q} \right) - 1 \right) \\
&= \frac{1}{2} \left(\left(\frac{d\mathbf{S}}{d\xi} \mathbf{q} \right)^T \left(\frac{d\mathbf{S}}{d\xi} \mathbf{q} \right) - 1 \right) \\
&= \frac{1}{2} \left(\frac{\mathbf{q}^T \mathbf{S}_\xi^T \mathbf{S}_\xi \mathbf{q}}{l^2} - 1 \right)
\end{aligned} \quad (33)$$

Finally, the equations of motion of the flexible beam element with external force yield the following equation.

$$\begin{aligned} \mathbf{M}\ddot{\mathbf{q}} + (\mathbf{K}_a + \mathbf{K}_b)\mathbf{q} \\ = \mathbf{S}^T \mathbf{F}^e + A\bar{\mathbf{S}}^T \mathbf{w} - C_d \bar{\mathbf{I}} \bar{\mathbf{S}} \dot{\mathbf{q}}(t) \end{aligned} \quad (34)$$

2.1.3. Kinematic constraints

In this study, a joint is defined as a kinematic constraint between two bodies [31]. Therefore, the joints that connect two bodies impose restrictions on the relative motion of each of the bodies by constraint forces.

(1) Kinematic constraints between rigid bodies

The joint can be categorized according to the motion that is allowed by the joint. In three-dimensional (3D) space, an unconstrained rigid body has six degrees of freedom (DOFs), as follows: translational and rotational motions that are about the three independent axes, x , y , and z . Several common types of joints are shown in Table 1. A detailed explanation and the mathematical description of each joint are presented in Ham et al. [35].

Table 2-1. Joint types and the allowable relative motion.

Joint type	Allowable relative motion on the degrees of freedom (DOFs)					
	x-trans	y-trans	z-trans	x-rot	y-rot	z-rot
Free motion	O	O	O	O	O	O
Spherical (ball)	X	X	X	O	O	O
Universal	X	X	X	O	O	X
Revolute (hinge)	X	X	X	X	X	O

Cylindrical	X	X	O	X	X	O
Prismatic (sliding)	X	X	O	X	X	X
Fixed	X	X	X	X	X	X

(2) Kinematic constraints between rigid and 1D flexible bodies

The constraint equations between an ANCF beam and a rigid body are presented by Ham et al. [44]. To formulate the kinematic constraints between a beam and a rigid body, we define the generalized coordinate of a beam and a rigid body as

$$\mathbf{q} = \left[\mathbf{r}_0^i \quad \mathbf{r}_0^{ii} \quad \mathbf{r}_l^i \quad \mathbf{r}_l^{ii} \quad \mathbf{r}_G \quad \boldsymbol{\theta}_G \right]^T. \quad (35)$$

As mentioned before, the mooring lines are modeled to be connected to the floating barge and the seabed with ball joints. To make a ball joint, the end node position of the i th beam should coincide with the designated point on the rigid body, as shown in Figure 2-6.

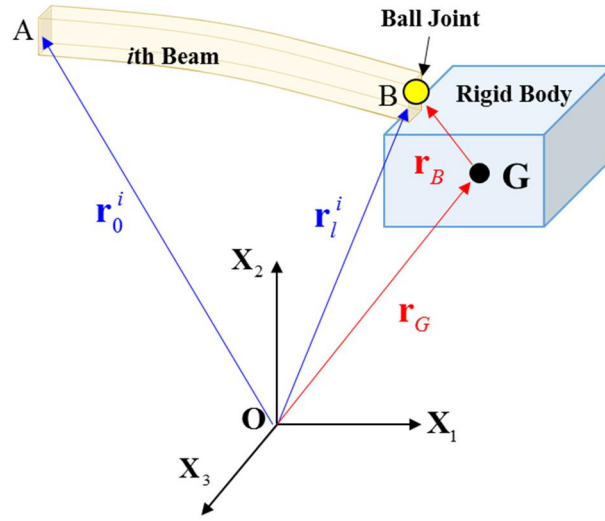


Figure 2-6. Ball joint between the beam and rigid body.

This relation can be expressed by

$$\begin{aligned}
 \mathbf{g}^{(ball,3)} &= {}^E \mathbf{r}_{B,flexible} - {}^E \mathbf{r}_{B,rigid} \\
 &= {}^E \mathbf{r}_l^i - ({}^E \mathbf{r}_G + {}^E \mathbf{R}_G {}^G \mathbf{r}_B) = \mathbf{S}(\xi) \mathbf{q} - ({}^E \mathbf{r}_G + {}^E \mathbf{R}_G {}^G \mathbf{r}_B) = 0
 \end{aligned} \quad (36)$$

where $\mathbf{R}(\theta_G)$ is the rotation matrix that transforms the local vector into the global vector. ξ is equal to l if the ball joint is located at the end node position of the beam. The constraint Jacobian matrix is obtained as

$$\mathbf{G}^{(ball)} = \frac{\partial \mathbf{g}^{(ball,3)}}{\partial \mathbf{q}} = \begin{bmatrix} \mathbf{S}(\xi) & -\mathbf{I}_{3 \times 3} & [{}^E \mathbf{R}_G \mathbf{r}_B] \end{bmatrix}. \quad (37)$$

Based on the kinematic description of the beam element and the constraint Jacobian

matrix, the kinetic and strain energy can be derived. Finally, the equations of motion of the flexible multibody system can be obtained from the Euler-Lagrange equation. The equations of motion for the multibody system, including rigid and flexible bodies, are as follows.

$$\begin{bmatrix}
 \mathbf{M}_{rigid} & \mathbf{0} & -\mathbf{G}_{k,(rigid-rigid)}^T & -\mathbf{G}_{k,(flex-rigid)}^T \\
 \mathbf{0} & \mathbf{M}_{flex} & -\mathbf{G}_{k,(rigid-flex)}^T & -\mathbf{G}_{k,(flex-flex)}^T \\
 \mathbf{G}_{k,(rigid-rigid)} & \mathbf{G}_{k,(rigid-flex)} & \Gamma_1 \frac{4\boldsymbol{\varepsilon}_1}{h^2} & \mathbf{0} \\
 \mathbf{G}_{k,(flex-rigid)} & \mathbf{G}_{k,(flex-flex)} & \mathbf{0} & \Gamma_2 \frac{4\boldsymbol{\varepsilon}_2}{h^2}
 \end{bmatrix}
 \begin{bmatrix}
 \mathbf{v}_{k+1}^{(rigid)} \\
 \mathbf{v}_{k+1}^{(flex)} \\
 \boldsymbol{\lambda}_{k+1}^1 \\
 \boldsymbol{\lambda}_{k+1}^2
 \end{bmatrix}
 =
 \begin{bmatrix}
 \mathbf{M}_{rigid} \mathbf{v}_k^{(rigid)} - h \frac{\partial V}{\partial \mathbf{q}_k} + h \mathbf{f}(\mathbf{q}_k, \mathbf{v}_k) \\
 \mathbf{M}_{flex} \mathbf{v}_k^{(flex)} - h(\mathbf{K}_t + \mathbf{K}_l) \mathbf{q}_k + h \mathbf{f}(\mathbf{q}_k, \mathbf{v}_k) \\
 -\frac{4\Gamma_1}{h} \mathbf{g}_k + \Gamma_1 \mathbf{G}_k \mathbf{v}_k \\
 -\frac{4\Gamma_2}{h} \mathbf{g}_k + \Gamma_2 \mathbf{G}_k \mathbf{v}_k
 \end{bmatrix}. \quad (38)$$

2.2. Modeling of the wire rope

2.2.1. Constraint-based wire rope model

In this study, the wire rope is modeled as a constraint to consider the interferences with the body effectively. Then, the constraint and constraint Jacobian is calculated to formulate DELE.

(1) Stretching constraint

Shown in Figure 2-7, Body A and Body B are connected with a wire rope with an initial length $l_{initial}$, and the length of the wire rope is l . Then, the constraint of the wire rope is

$$g(\mathbf{q}) = l - l_{initial} = |\mathbf{r}_A - \mathbf{r}_B| - l_{initial} = 0, \quad (39)$$

where \mathbf{r}_A and \mathbf{r}_B are position vectors from the origin O to point A and B , respectively. The constraint equation becomes zero when the length of the wire rope is equal to the initial length. If the wire rope is stretched, which means the constraint is violated, the constraint force is exerted on the wire rope to satisfy the constraints. The constraint force is then given by

$$F = \lambda \cdot g(\mathbf{q}). \quad (40)$$

The constraint force is proportional to $g(\mathbf{q})$, which is the change in the length of the

wire rope and is exerted by each end of the wire rope. Therefore, the constraint force works as a tension of the wire rope. This model works the same as the massless spring model by calculating the spring force as a constraint force. In the DELE (11), the term ε is inversely proportional to the spring coefficient. Therefore, the error of the constraint equation for the wire rope can increase when the spring coefficient of the wire rope is small. In other words, the wire rope can relate stretch to stiffness. As the wire rope is modeled as a straight line, the looseness of the wire rope was not considered in this study.

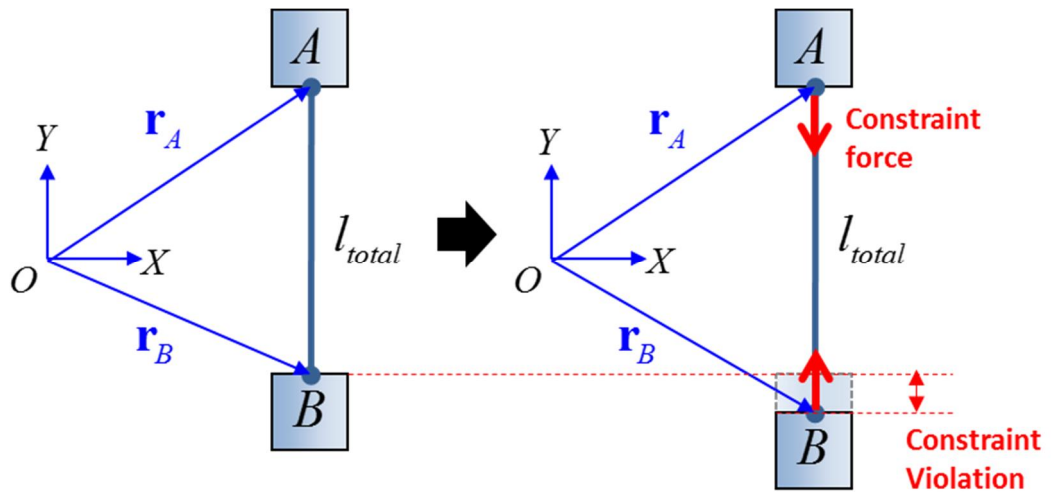


Figure 2-7. Constraint-based wire rope with stretching.

(2) Bending constraint

The bending of the wire rope can be also modeled with additional constraints. To simulate bending, the wire rope should be divided into several elements. Then, the direction of each vector of the segment should remain the same to simulate bending stiffness. Figure 2-8 shows the vector \mathbf{d}_i of each wire rope segment.

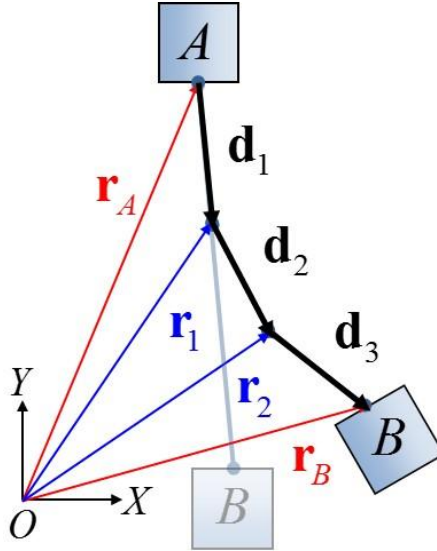


Figure 2-8. Constraint-based wire rope with bending.

The bending constraint of the wire rope is then obtained as the following equations.

$$g_1(\mathbf{q}) = \frac{\mathbf{r}_1 - \mathbf{r}_A}{|\mathbf{r}_1 - \mathbf{r}_A|} - \frac{\mathbf{r}_2 - \mathbf{r}_1}{|\mathbf{r}_2 - \mathbf{r}_1|} = 0, \quad g_2(\mathbf{q}) = \frac{\mathbf{r}_2 - \mathbf{r}_1}{|\mathbf{r}_2 - \mathbf{r}_1|} - \frac{\mathbf{r}_B - \mathbf{r}_2}{|\mathbf{r}_B - \mathbf{r}_2|} = 0 \quad (41)$$

(3) Torsion constraint

The torsion is the twisting deformation of the wire rope. In the same way, with the other constraints, the torsion constraint can be modeled by the relative angle between two bodies connected with wire rope. Figure 2-9 shows the torsion of the wire rope connecting two bodies.

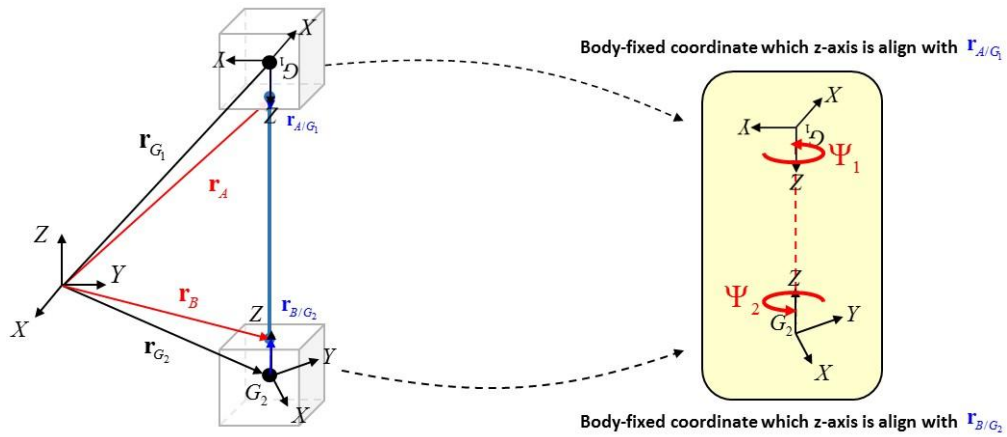


Figure 2-9. Constraint-based wire rope with torsion.

For each body, the body-fixed coordinate in which the z-axis is aligned with the wire rope can be selected. Then, the twist angle Ψ is the rotational angle of the body with the z-axis. The constraint equation is then can be obtained as follows, which implies that the twist angle of two bodies should be the same.

$$g(\mathbf{q}) = \Psi_1 + \Psi_2 = 0 \quad (42)$$

(4) Wire rope with multiple segments

With the stretching constraint described previously, the constraint works in the same way with the incompressible spring model. However, the constraint model can be applied to more complicated cases that the spring model cannot reflect. As shown in Figure 2-10, even when the wire rope is split into several segments, the wire rope can be expressed as one simple constraint as follows. Bending and torsion stiffness are neglected in this study.

$$\begin{aligned}
g(\mathbf{q}) &= l_a + l_b + l_c - l_{initial} \\
&= |\mathbf{r}_1 - \mathbf{r}_A| + |\mathbf{r}_2 - \mathbf{r}_1| + |\mathbf{r}_B - \mathbf{r}_2| - l_{initial} = 0
\end{aligned} \tag{43}$$

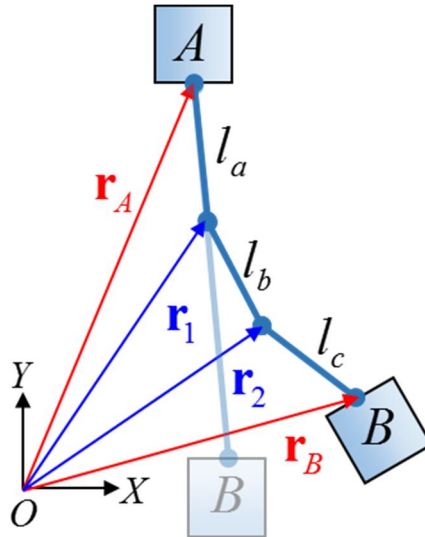


Figure 2-10. The wire rope split into several segments.

In this way, the split of the wire rope due to the contact with bodies (Figure 2-11), or the winding around the body such as pulleys (Figure 2-12) can be simulated by using constraint-based wire rope. The advantage of this model is that the number of the constraint does not increase as the number of the segment consisting of one wire rope increases. The number of the wire rope constraint remains one with another form that describes the summation of the length of each segment is same as the initial length. It can simulate the various situation in the block erection operation easily without the increases in the simulation cost.

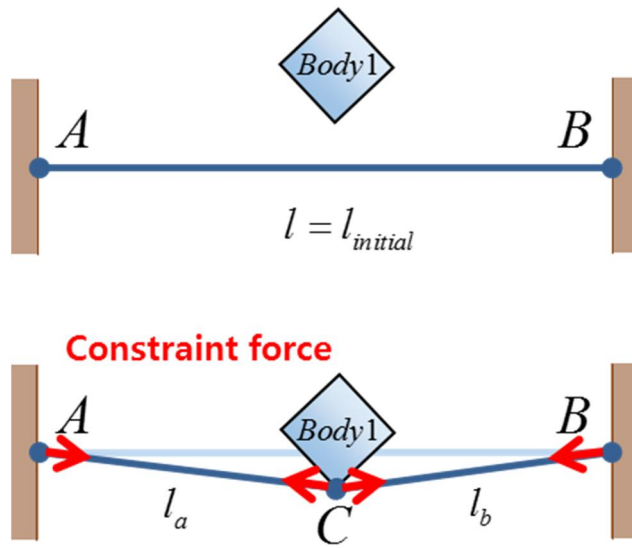


Figure 2-11. The wire rope split due to the contact with the body.

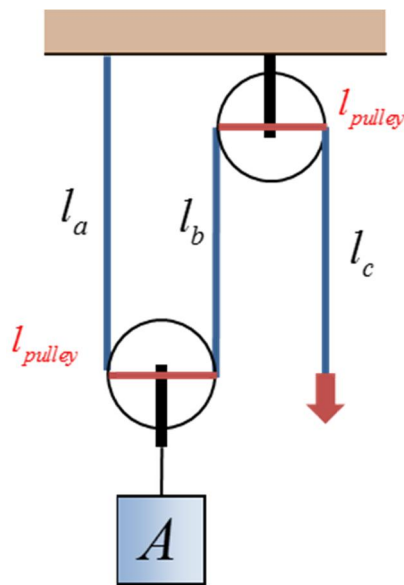


Figure 2-12. The wire rope winding pulleys.

2.2.2. Mooring line model

(1) Catenary mooring line

Traditionally, the dynamic motion of the floating crane has been analyzed based on the multibody dynamics. For this purpose, simulation tools are developed for dynamic analysis of the shipbuilding and offshore operation processes [43], [45]. In these programs, modeling of the mooring line is simply suggested, using the massless spring or analytical catenary model, which is not appropriate for dynamic analysis.

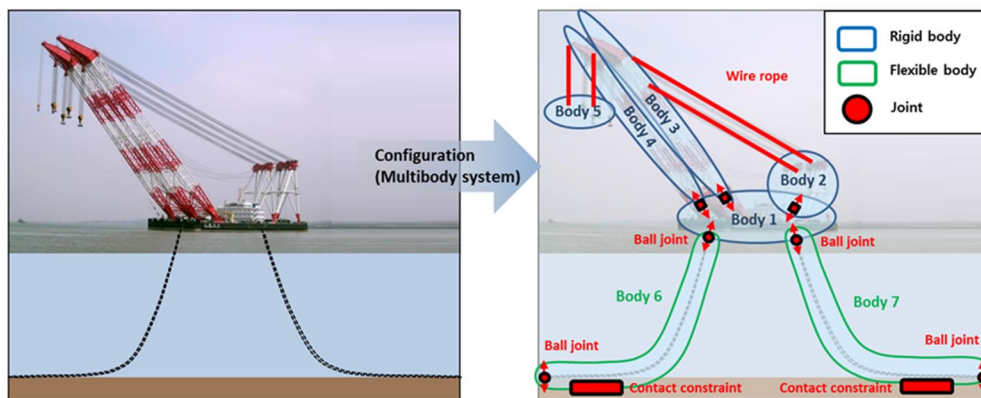


Figure 2-13. The configuration of a floating crane and the mooring system.

In this study, we suggested the FEM-based mooring line model applicable to the multibody system using the flexible multibody dynamics. As shown in Figure 2-13, the mooring line can be modeled as a flexible body, which connects the floating barge and the seabed. The mooring line was modeled with a group of flexible beam elements, and connected to a floating body and the seabed with ball joints. Then, contact with the seabed is modeled as a number of constraints. The theoretical backgrounds of the flexible multibody dynamics including beam elements and the joints with the rigid body are

illustrated in section 2.1.2, and also well explained in Ham [43].

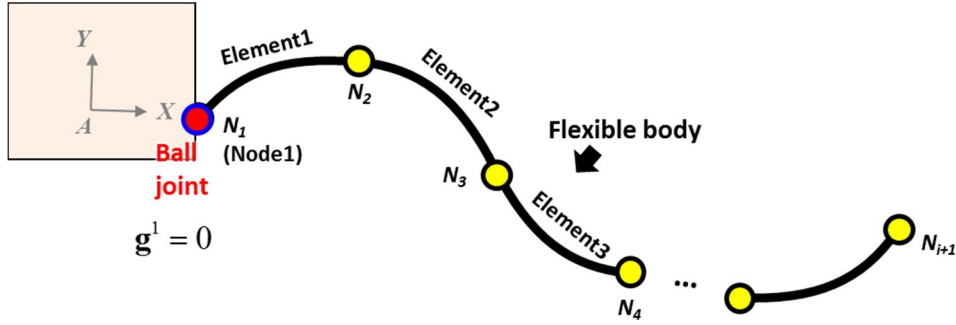


Figure 2-14. The configuration of a multibody system with multiple beam elements.

Figure 2-14 shows a multibody system consists of a rigid body and multiple beam elements denoted by A and f connected with a ball joint. Then, the multibody formulation, DELE, is expressed as shown in Eq. (44).

$$\begin{bmatrix} \mathbf{M}^A & \mathbf{0} & -(\mathbf{G}_A)_k^T \\ \mathbf{0} & \mathbf{M}^f & -(\mathbf{G}_f)_k^T \\ (\mathbf{G}_A)_k & (\mathbf{G}_f)_k & \Gamma \frac{4\epsilon}{h^2} \end{bmatrix} \begin{bmatrix} \mathbf{v}_{k+1}^A \\ \mathbf{v}_{k+1}^f \\ \boldsymbol{\lambda}_{k+1} \end{bmatrix} = \begin{bmatrix} \mathbf{M}^A \mathbf{v}_k^A + h\mathbf{f}^A \\ \mathbf{M}^f \mathbf{v}_k^f + h\mathbf{f}^f \\ \frac{4\Gamma}{h^2} \mathbf{g}_k + \Gamma \mathbf{G}_k \mathbf{v}_k \end{bmatrix} \quad (44)$$

The multiple beam elements are composed of i flexible 1D-beam elements. Each flexible element shares the end node with the neighboring element to have the same position and slope. Therefore, the coordinate \mathbf{v}^f and the mass matrix \mathbf{M}^f of the multiple beam elements are defined as follows.

$${}^E \mathbf{v}_{flexible} = \frac{d\mathbf{S}}{d\xi} \mathbf{q} = \mathbf{S}_\xi \begin{bmatrix} {}^E \mathbf{r}_{N_1} \\ {}^E \dot{\mathbf{r}}_{N_1} \\ \vdots \\ {}^E \mathbf{r}_{N_{i+1}} \\ {}^E \dot{\mathbf{r}}_{N_{i+1}} \end{bmatrix} \quad (45)$$

$$\mathbf{M}^f = \begin{pmatrix} \mathbf{M}_{element1}^f & & & \mathbf{0} \\ (12 \times 12) & & & \\ & \mathbf{M}_{element2}^f & & \\ & (12 \times 12) & & \\ & & \mathbf{M}_{element3}^f & \\ & & (12 \times 12) & \\ \mathbf{0} & & & \ddots \end{pmatrix}$$

The mass matrices of the elements are overlapped as they share end nodes. Each mass matrix is obtained from the beam shape function in Eq. (27). Similarly, the force \mathbf{f}^f is composed of the sum of the internal and external forces as follows.

$$\mathbf{f}^f = \begin{pmatrix} \mathbf{K}_{element1} & & & \mathbf{0} \\ (12 \times 12) & & & \\ & \mathbf{K}_{element2} & & \\ & (12 \times 12) & & \\ & & \mathbf{K}_{element3} & \\ & & (12 \times 12) & \\ \mathbf{0} & & & \ddots \end{pmatrix} \mathbf{q}^f \quad (46)$$

$$+ \begin{pmatrix} \mathbf{S}^T(\xi_1) & \mathbf{0} & \mathbf{0} \\ (12 \times 3) & & \\ \mathbf{0} & \mathbf{S}^T(\xi_2) & \mathbf{0} \\ & (12 \times 3) & \\ \mathbf{0} & \mathbf{0} & \mathbf{S}^T(\xi_3) \\ & & (12 \times 3) \\ \mathbf{0} & \mathbf{0} & \ddots \end{pmatrix} \begin{bmatrix} \mathbf{F}_{element1}^e \\ \mathbf{F}_{element2}^e \\ \mathbf{F}_{element3}^e \\ \vdots \end{bmatrix} + \begin{pmatrix} A_1 l_1 \bar{\mathbf{S}}^T & \mathbf{0} & \mathbf{0} \\ (12 \times 3) & & \\ \mathbf{0} & A_2 l_2 \bar{\mathbf{S}}^T & \mathbf{0} \\ & (12 \times 3) & \\ \mathbf{0} & \mathbf{0} & A_3 l_3 \bar{\mathbf{S}}^T \\ & & (12 \times 3) \\ \mathbf{0} & \mathbf{0} & \ddots \end{pmatrix} \begin{bmatrix} \mathbf{w}_{element1} \\ \mathbf{w}_{element2} \\ \mathbf{w}_{element3} \\ \vdots \end{bmatrix}$$

The constraint equation \mathbf{g} and its Jacobian \mathbf{G}_A , \mathbf{G}_f of the ball joint between a rigid body and flexible element are obtained in Eq. (36) and Eq. (37).

(2) Initial position calculation

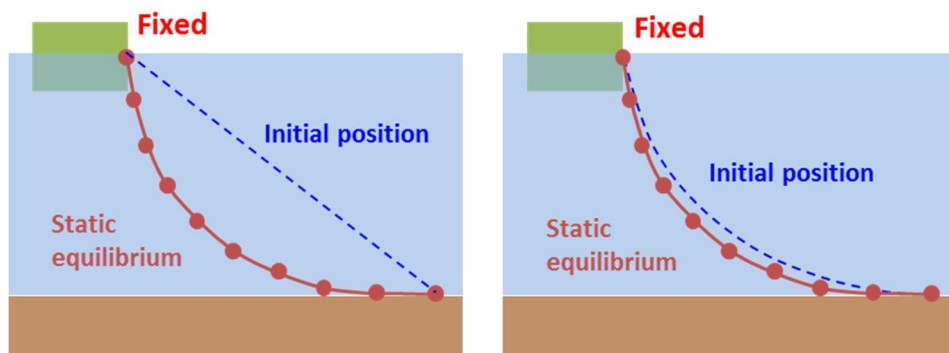


Figure 2-15. The necessity of the calculation of the initial position.

Unlike other systems with flexible bodies that the deformation occurs during the simulation, the mooring line is highly deformed at the beginning due to its weight. Moreover, the strain can become large in the case of the mooring line. Therefore, the initial position and the orientation of each node of the mooring line should be defined before the simulation (Figure 2-15). Simply put, the mooring line can be modeled as a straight line connecting two points with no initial deflection. However, if the mooring line is modeled as a straight line, buckling may occur instantaneously at the initial stage (Figure 2-16). It is because of the large compressive stress at the beginning, as the unstretched length of the mooring line is much longer than the length of the straight line. Furthermore, it takes a long time to find the equilibrium state. Therefore, to find the static equilibrium shape of the mooring line, we applied the analytical catenary model.

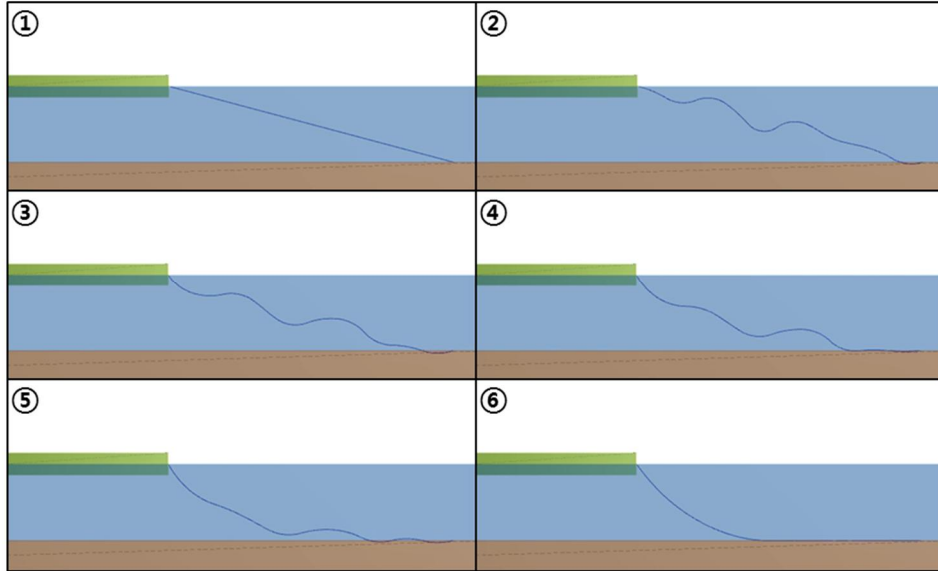


Figure 2-16. Buckling of the mooring line at the initial stage.

The analytical catenary model calculates the profile and the tension of the catenary mooring line with two given endpoints, total unstretched length, and the weight per unit length. The elastic stiffness is neglected. Based on the force equilibrium equations and shape information, the following equation is obtained [46], [47].

$$\frac{bq/2T_H}{\sinh(bq/2T_H)} - \frac{b}{\sqrt{S^2 - h^2}} = 0, \quad \begin{cases} b = x_2 - x_1 \\ h = y_2 - y_1 \end{cases} \quad (47)$$

where b , h is the horizontal and vertical length, respectively, S is the total unstretched length, q is the weight per unit length, and T_H is the horizontal tension. The coordinates of two ends are (x_1, y_1) and (x_2, y_2) , respectively. The horizontal tension can be obtained by

solving Eq. (47). Then, the catenary profile of the mooring line can be obtained. Meanwhile, in the real world, part of the mooring line is laid on the seabed, as in Figure 2-17. Therefore, considering the mooring length on the seabed, we can get the final equation, Eq. (48).

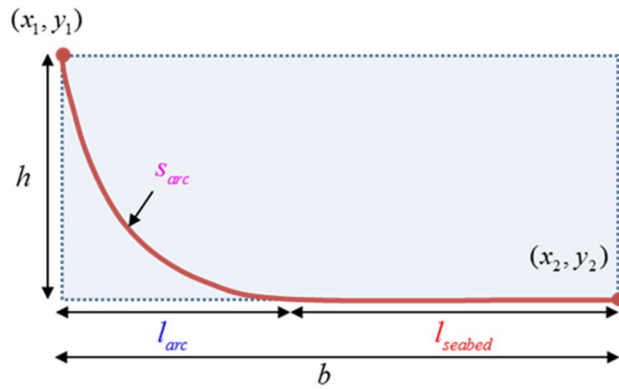


Figure 2-17. The mooring line considering the length on the seabed.

$$\begin{aligned}
 l_{arc} &= \frac{T_H}{q} \cosh^{-1} \left(\frac{q}{T_H} h + 1 \right) \\
 s_{arc} &= \frac{T_H}{q} \sinh \left(\frac{q l_{arc}}{T_H} \right) \\
 l_{seabed} &= b - l_{arc}
 \end{aligned} \tag{48}$$

Each beam element of the mooring line is located following the analytic catenary equation. The beam element can be described by the position and slope vectors of each end. Therefore, the position and slope vectors for the nodes divided by the number of the element should be calculated. We assume that the length of the elements is the same at

the initial. Then, the relationship between the length and position of the element in the two-dimensional mooring plane can be described as Eq. (49).

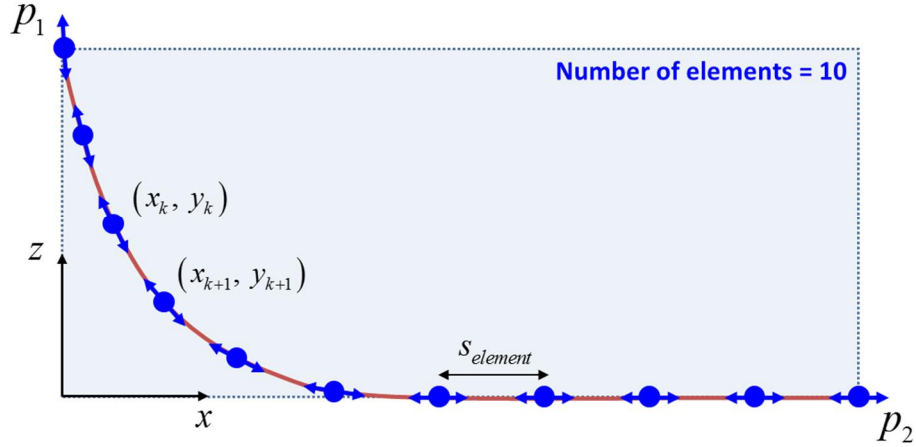


Figure 2-18. The initial position of each beam element.

$$\begin{aligned}
 s_{element} &= S / N_{element} \\
 s_{element} &= \frac{T_H}{q} \sinh\left(\frac{q}{T_H} x_k\right) - \frac{T_H}{q} \sinh\left(\frac{q}{T_H} x_{k+1}\right) \\
 y_k &= \frac{T_H}{q} \left(\cosh\left(\frac{q}{T_H} x_k\right) - 1 \right) \\
 y'_k &= \sinh\left(\frac{q}{T_H} x_k\right)
 \end{aligned} \tag{49}$$

x_k and y_k , and x_{k+1} and y_{k+1} is the position of two endpoints of k_{th} element on the plane (Figure 2-18). Finally, by the three-dimensional global transformation, the position and

slope vector of the elements can be obtained.

(3) External forces

The current force is one of the main external loads exerted on the mooring line in the water. To calculate the current force on the mooring line with dynamic motion, the Morison equation (Morison et al., 1950) is adopted. The following equation is the basic form of the Morison equation.

$$F = \rho V \dot{u} + \rho C_a V (\dot{u} - \dot{v}) + \frac{1}{2} \rho C_d A (u - v) |u - v| \quad (50)$$

Here, C_a and C_d are the added mass and drag coefficient, V is the volume, and A is the cross-sectional area of the body. u and v are the speed of the current and the body, respectively. The speed of the current u is the function of the water depth. According to IEC 61400-3 (2009), if the current speed at the surface is given, the profile of the velocity can be expressed as

$$u(z) = u(0) \cdot \left(\frac{z + d}{d} \right)^{1/7}, \quad (51)$$

where d is the total depth of the water, which is positive, and z is the height, which is negative in a downward direction. The current speed on the seabed becomes zero.

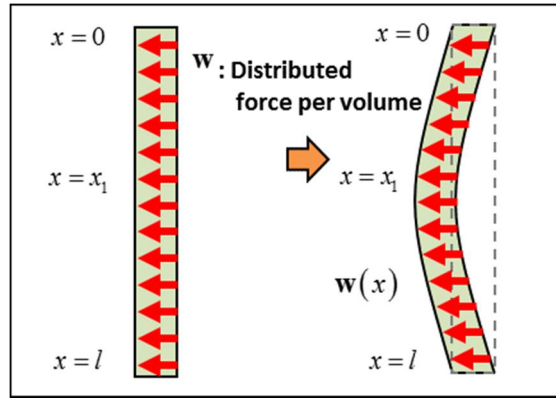


Figure 2-19. The distributed force exerted on a flexible beam element.

To calculate the total current force exerted on a flexible beam element, the distributed force is integrated along with the element. The distributed current force per unit length is as follows: d is the diameter of the beam element.

$$w = -\rho C_a \frac{1}{4} \pi d^2 \dot{v} + \frac{1}{2} \rho C_d d (u - v) |u - v| \quad (52)$$

The first term of Eq. (52) is the added mass force, and the second term is damping force. To calculate the total current force exerted on the flexible beam element, the distributed force should be integrated along with the element. The acceleration and the velocity of the beam element are the same as the second derivative and derivative of the position vector.

$$\begin{aligned} \mathbf{v}(x, t) &= \dot{\mathbf{r}}(x, t) = \mathbf{S}(\xi) \dot{\mathbf{q}}(t) \\ \dot{\mathbf{v}}(x, t) &= \ddot{\mathbf{r}}(x, t) = \mathbf{S}(\xi) \ddot{\mathbf{q}}(t) \end{aligned} \quad (53)$$

Then, the added mass force acting on the beam element can be calculated.

$$\begin{aligned}
d\mathbf{F}_{added} &= -\rho C_a \frac{1}{4} \pi d^2 \cdot \dot{\mathbf{v}} dx \\
&= -\rho C_a \frac{1}{4} \pi d^2 \cdot \{\mathbf{S}(\xi) dx\} \ddot{\mathbf{q}}(t) \\
&= -\rho C_a \frac{1}{4} \pi d^2 l \cdot \{\mathbf{S}(\xi) d\xi\} \ddot{\mathbf{q}}(t)
\end{aligned} \tag{54}$$

The Jacobian is multiplied to Eq. (54) for the coordinate transformation.

$$\begin{aligned}
d\mathbf{Q}_{added} &= \left(\frac{\partial \mathbf{r}}{\partial \mathbf{q}} \right)^T d\mathbf{F}_{added} \\
&= \mathbf{S}^T d\mathbf{F}_{added} \\
&= \mathbf{S}^T \cdot \left[-\rho C_a \frac{1}{4} \pi d^2 l \cdot \{\mathbf{S}(\xi) d\xi\} \ddot{\mathbf{q}}(t) \right] \\
&= -\rho C_a \frac{1}{4} \pi d^2 l \cdot \{\mathbf{S}^T \mathbf{S} d\xi\} \ddot{\mathbf{q}}(t)
\end{aligned} \tag{55}$$

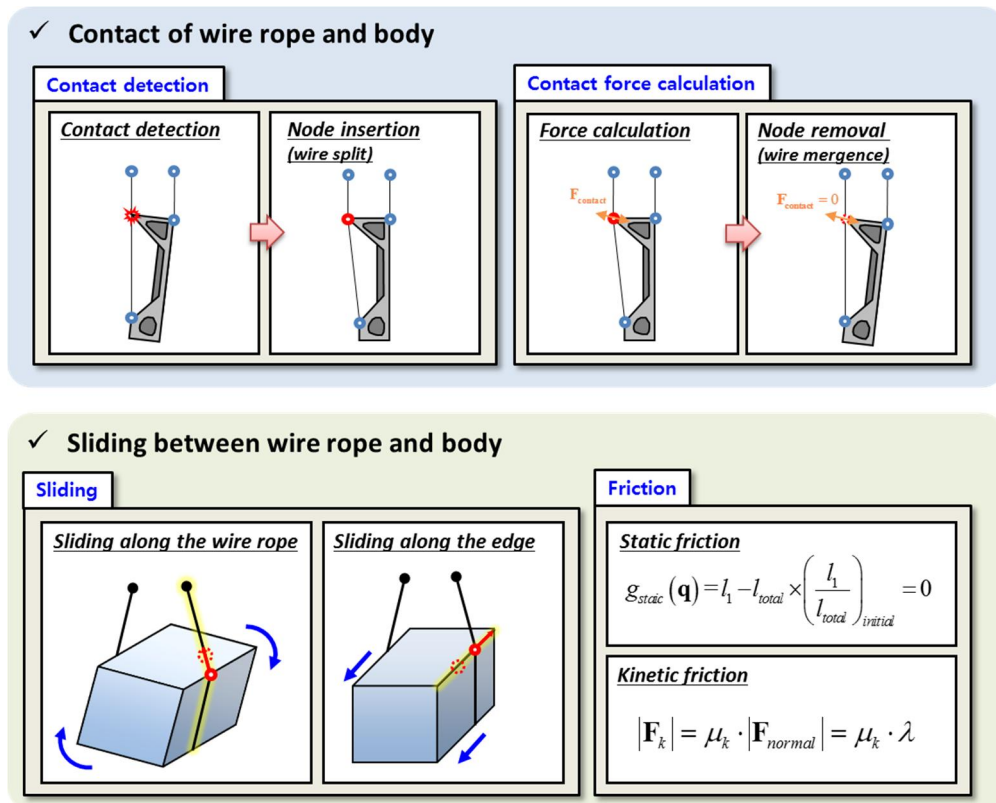
Finally, the generalized added mass force over the beam is obtained as follows.

$$\begin{aligned}
& \mathbf{Q}_{added} \\
&= \int_0^1 d\mathbf{Q}_{added} \\
&= -\rho C_a \frac{1}{4} \pi d^2 l \left(\int_0^1 \mathbf{S}^T \mathbf{S} d\xi \right) \ddot{\mathbf{q}}(t) \\
&= -\rho C_a \frac{1}{4} \pi d^2 l \bar{\mathbf{S}} \ddot{\mathbf{q}}(t)
\end{aligned} \tag{56}$$

The damping force can be calculated in the same way. The velocity of the element is assumed to be constant. Then, the generalized damping force yields the following equation.

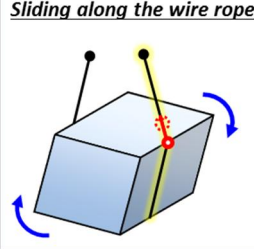
$$\begin{aligned}
& \mathbf{Q}_{damping} \\
&= \iiint_V \mathbf{S}^T \mathbf{w}^e dV \\
&= \int_0^l \mathbf{S}^T \frac{1}{2} \rho C_d d \cdot (\mathbf{u} - \mathbf{v})^2 dx \\
&= \int_0^1 \mathbf{S}^T \frac{1}{2} \rho C_d d \cdot (\mathbf{u} - \mathbf{v})^2 l d\xi \\
&= \left(\int_0^1 \mathbf{S}^T d\xi \right) \frac{1}{2} \rho C_d d \cdot (\mathbf{u} - \mathbf{v})^2 l \\
&= \bar{\mathbf{S}}^T \frac{1}{2} \rho C_d d \cdot (\mathbf{u} - \mathbf{v})^2 l
\end{aligned} \tag{57}$$

2.3. Interaction between wire rope and body

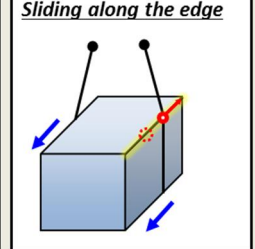


Sliding

Sliding along the wire rope



Sliding along the edge



Friction

Static friction

$$g_{static}(\mathbf{q}) = l_1 - l_{total} \times \left(\frac{l_1}{l_{total}} \right)_{initial} = 0$$

Kinetic friction

$$|\mathbf{F}_k| = \mu_k \cdot |\mathbf{F}_{normal}| = \mu_k \cdot \lambda$$

Figure 2-20. The interaction between the wire rope and the body.

The interaction between the wire rope and the body can be divided into two processes; contact and sliding (Figure 2-20). The contact process performs node insertion and removal, and the sliding process updates the position of the node and calculates the frictional force.

2.3.1. Contact model

The contact model consists of a contact detection procedure and a contact force

calculation procedure. The overall procedure is illustrated in Figure 2-21. This process is performed at every interval of time during the numerical calculation of the equations of motion.

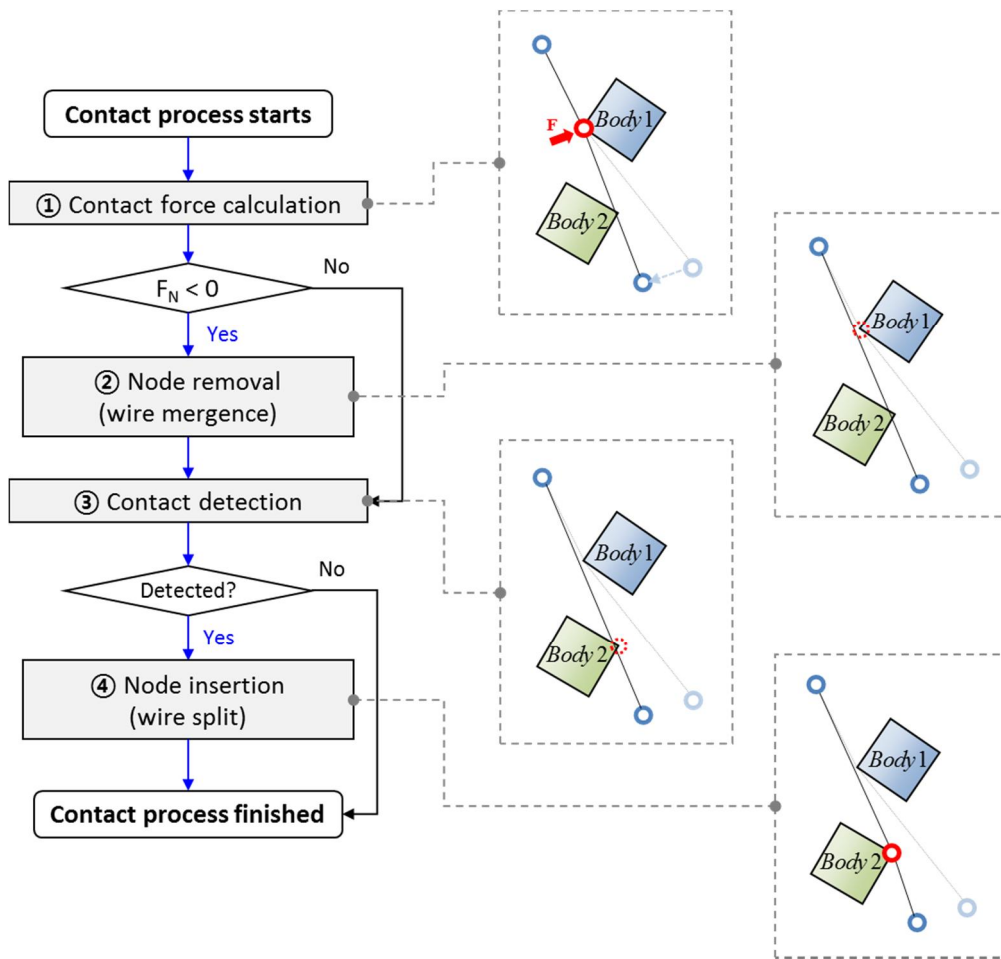


Figure 2-21. The contact process between the body and the wire rope.

(1) Contact detection and node insertion

① Contact detection

As the contact between the wire rope and the body is detected, the contact nodes are inserted, which split the wire rope. The contact detection is composed of a broad phase and a narrow phase (Figure 2-22), to reduce the detection time.

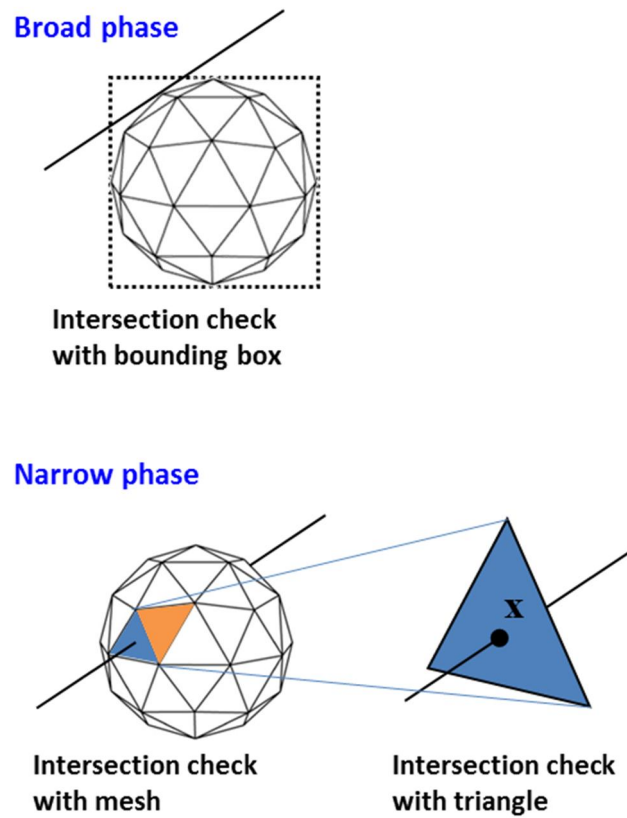


Figure 2-22. Broad phase and narrow phase for contact detection.

In the broad phase, the intersection between the wire rope and the bounding box of the body is checked. Then, if the intersection is detected in the broad phase, the narrow phase is activated. Generally, the block model used in the shipbuilding and offshore industries consists of triangular meshes. The narrow phase checks the intersection between the wire

rope and each triangle mesh of the block. To find the intersection points, general intersection algorithms between a triangle and a straight line can be used. For this, Möller's algorithm [48], which is generally known as the fastest algorithm, was used in this study.

With the given start point and the direction of a straight line (line), as well as three vertices of a triangular mesh (triangle), Möller's algorithm calculates the intersection point by using barycentric coordinates of the triangle. The line $R(t)$ with the origin O and the direction D can be defined as

$$R(t) = O + tD. \quad (58)$$

It is assumed that the triangle has three vertices V_0 , V_1 , and V_2 . Then, a random point T on the triangle using barycentric coordinates is given by:

$$T(u, v) = V_0 + u \cdot (V_1 - V_0) + v \cdot (V_2 - V_0), \quad (u + v \leq 1, \quad u, v \geq 0) \quad (59)$$

The point must satisfy this condition to be located in the triangle. As shown in Figure 2-23, the intersection point \mathbf{x} between the line and the triangle should satisfy the following.

$$\begin{aligned} O + tD &= V_0 + u \cdot (V_1 - V_0) + v \cdot (V_2 - V_0) \\ &= (1 - u - v)V_0 + uV_1 + vV_2 \end{aligned} \quad (60)$$

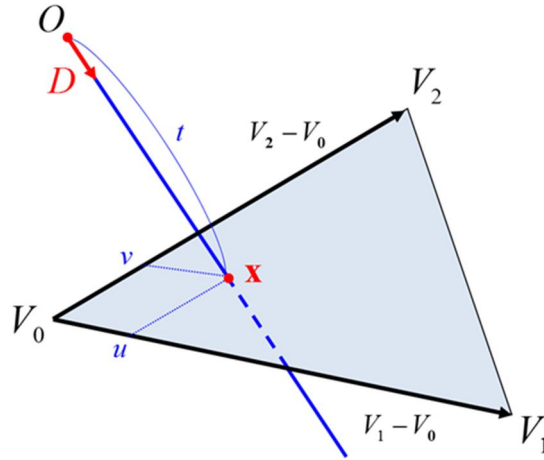


Figure 2-23. The intersection point of the triangle and the straight line.

Equation (60) can be rearranged as

$$\begin{bmatrix} -D & V_1 - V_0 & V_2 - V_0 \end{bmatrix} \begin{bmatrix} t \\ u \\ v \end{bmatrix} = O - V_0. \quad (61)$$

Solving the linear equation above, the distance t of the intersection point from the origin, and the barycentric coordinates u and v can be found. The solution for equation (61) can then be obtained using Cramer's rule.

$$\begin{bmatrix} t \\ u \\ v \end{bmatrix} = \frac{1}{(D \times (V_2 - V_0)) \cdot (V_1 - V_0)} \begin{bmatrix} (T \times (V_1 - V_0)) \cdot (V_2 - V_0) \\ (D \times (V_2 - V_0)) \cdot T \\ (T \times (V_1 - V_0)) \cdot D \end{bmatrix}. \quad (62)$$

The Möller's algorithm finds the intersection between the triangle and the line regarding that the line as a ray, which is an infinite half-straight line with origin. As the wire rope is a finite line in the simulation, the intersection is not calculated if the distance t is larger than the length of the wire rope. As the block can be represented as a group of triangular meshes, all triangles in the mesh group should be checked to determine if they intersect with the wire rope. If the intersection points are found, the node insertion process is performed.

② Node insertion (wire split)

The intersection point of the wire rope and the block is calculated in the contact detection procedure. The previous research by Lee et al. [5] split the wire rope with the intersection points from Möller's algorithm. However, that does not reflect the actual situation exactly, as the wire rope penetrates the body. In the numerical simulation, time passes by a certain time step. Thus, the wire rope could penetrate the body as the time increases discretely. To solve this problem, we calculated the contact point on the edge of the body as presented in Figure 2-24.

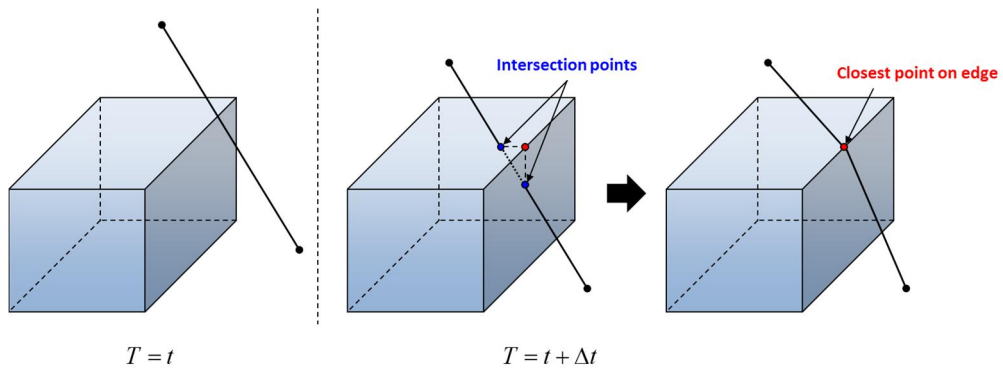


Figure 2-24. Contact node insertion.

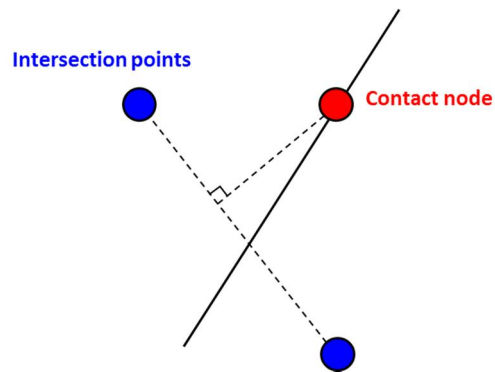


Figure 2-25. The contact node calculation with the intersection points.

As depicted in Figure 2-25, the contact node is found as the closest point on the edge and the intersection points. If the contact node is inserted in the wire rope, the constraint equation that represents the wire rope is changed as the following equation.

$$g(\mathbf{q}) = |\mathbf{r}_A - \mathbf{r}_C| + |\mathbf{r}_C - \mathbf{r}_B| - l_{total} = 0, \quad (63)$$

where r_A and r_B are the start and end position vector of the wire rope, and r_C is the position vector of the contact node.

(2) Contact force calculation and node removal

① Contact force calculation

In the wire split procedure above, the existing wire ropes are split into several segments. Then, the contact force on each contact point is calculated, and the wire rope segments are merged if the body is detached from the wire rope. To make a decision to merge the wire rope or not, the normal of the constraint force respect to the body should be calculated. As stated in the previous section, the contact node always exists on the edge of the body. For the calculation of the normal of the constraint force, the normal of the edge should be obtained first. The edge of the block is a segment created by the intersection of two planes. That indicates that we could find two neighboring planes that include the given edge.

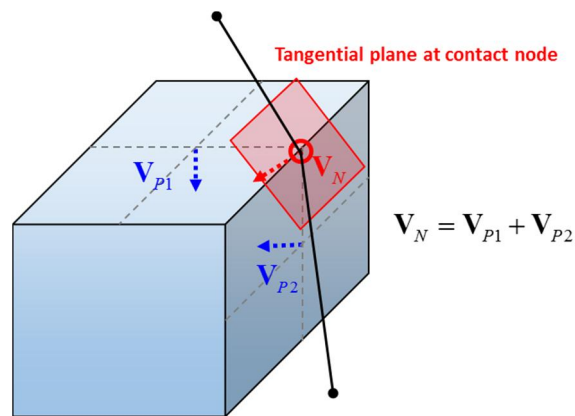


Figure 2-26. Tangential plane and normal vector at the edge.

In this study, the tangential plane and the normal vector at the edge is obtained by the sum of the normal vector of neighboring planes. The normal vector of the plane is assumed to face inside at all times. As presented in Figure 2-26, the normal vector at the edge of the contact node, \mathbf{V}_N can be expressed as the sum of \mathbf{V}_{P1} and \mathbf{V}_{P2} . The tangential plane at the contact node is a plane that includes the contact node, with the normal vector \mathbf{V}_N .

Meanwhile, the contact force at the node is the result of the tension of the wire rope segments split by the node. The contact force is given by the vector sum of tensions of the wire rope with the longitudinal direction.

$$\mathbf{F}^c = \mathbf{T}_1 + \mathbf{T}_2, \quad |\mathbf{T}_1| = |\mathbf{T}_2|. \quad (64)$$

The tensions on the wire rope are constant throughout the rope in case there is no friction. The normal of the contact force at the edge is then calculated as the inner product of the normal vector at the edge and the contact force.

$$F_N = \mathbf{V}_N \cdot \mathbf{F}^c. \quad (65)$$

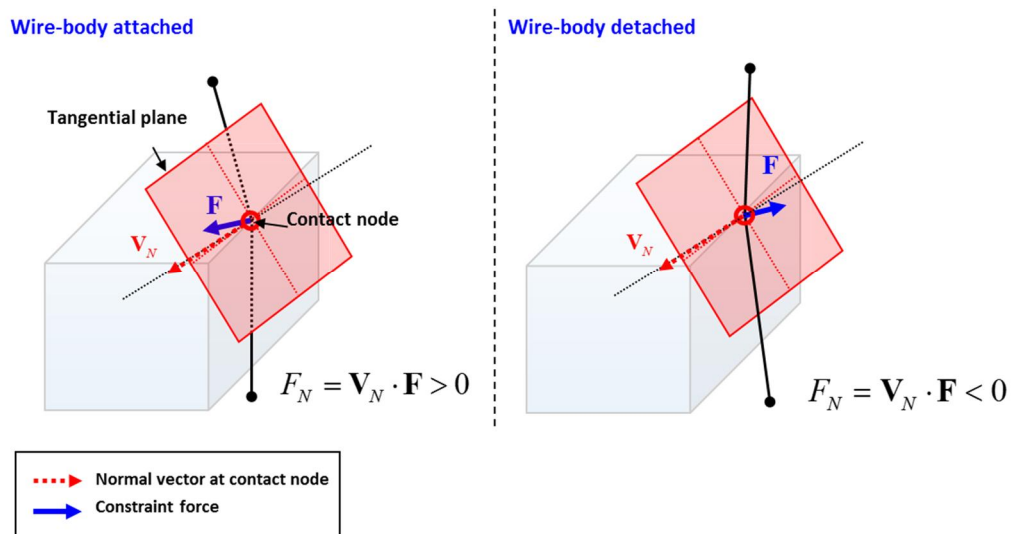


Figure 2-27. Attachment and detachment of the body and the wire rope.

Figure 2-27 shows the attachment and detachment of the body and the wire rope. If the normal of the contact force is positive, it means that the wire rope is exerting force to the body, and the wire rope remains attached. In case that the normal of the contact force becomes negative, we conclude the wire rope is no longer exerting force on the body and activates the wire merge procedure.

② Node removal (wire merge)

If the normal of the contact force becomes negative, the node is removed, and the wire rope, including the contact node, is merged. It is exactly the opposite procedure of the node insertion and wire split process. As the contact node is removed, the neighboring nodes of the wire rope are connected as illustrated in Figure 2-28.

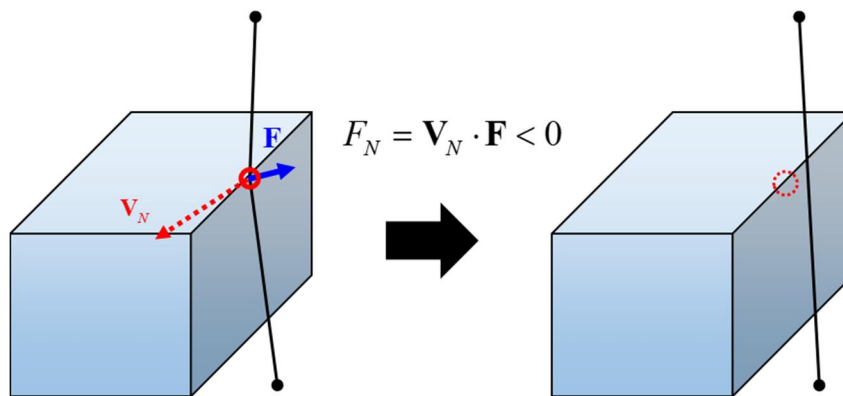


Figure 2-28. Node removal of the wire rope.

2.3.2. Sliding model

If the contact between the wire rope and the body occurs, the relative motion between them exists. The relative motion can be divided into two, sliding along the edge and sliding along the wire rope (Figure 2-29).

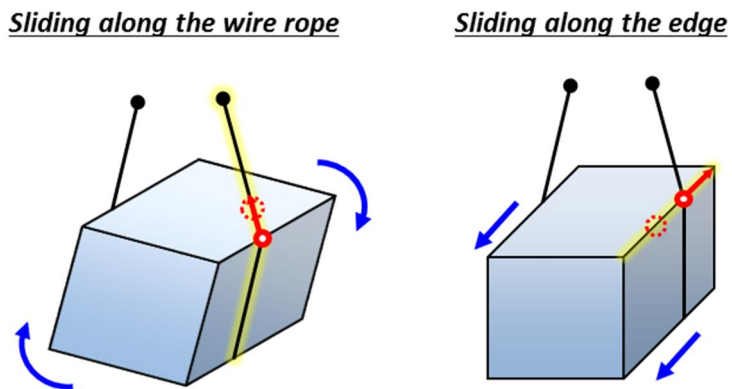


Figure 2-29. Relative motion between the wire rope and the body.

The sliding along the wire rope is the relative motion that the body moves along the

direction of the wire rope. If the block slides down along the wire rope, as presented in Figure 2-30, the position of the contact node, which is attached to the body, is changed. Then, the constraint equation of the wire rope is changed, including the node. The position of the node is automatically updated at each time interval, as the position of the body is changed.

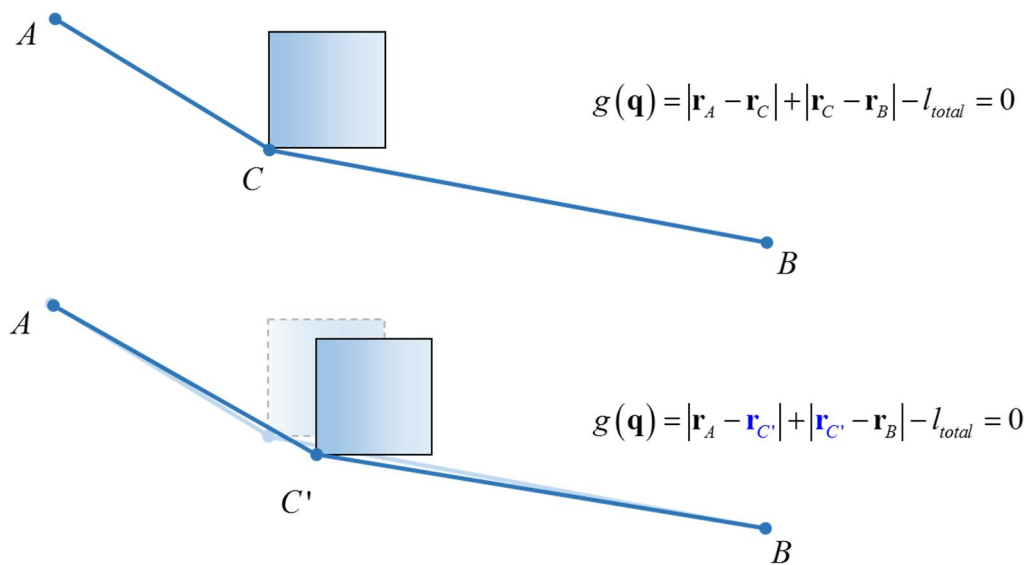


Figure 2-30. A body sliding along the wire rope.

On the other hand, if the wire rope slides along the edge of the body, the position of the contact node relative to the body is changed. The wire rope is not modeled as an object with mass and inertia, but the constraint. Therefore, different from the sliding along the wire rope, the position of the contact node along the edge should be explicitly calculated as the motion of the wire rope is not updated dynamically. In the case of the wire rope is stretched, the contact node slides along the edge of the body to make the length of the wire rope to a minimum. Therefore, the position of the contact node P is

updated to the final point P' , which is the closest point on the edge from the line connecting neighboring nodes (Figure 2-31).

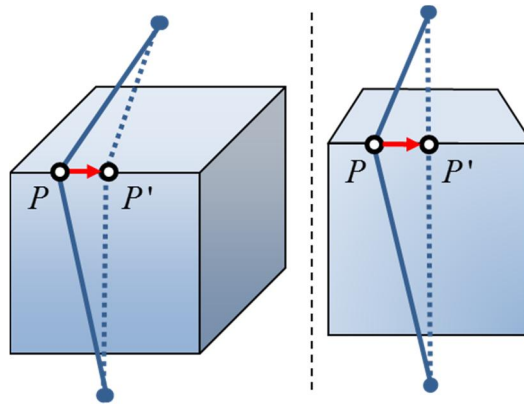


Figure 2-31. A wire rope sliding along the edge of the body.

Figure 2-31 shows the sliding of the wire rope along the edge that the contact node already exists. However, in case of the final point of the contact node does not exist on the edge, the contact node needs to move to the other edge to minimize the length. To solve this problem, we suggested the update procedure to allow the contact node to slide to the other edges.

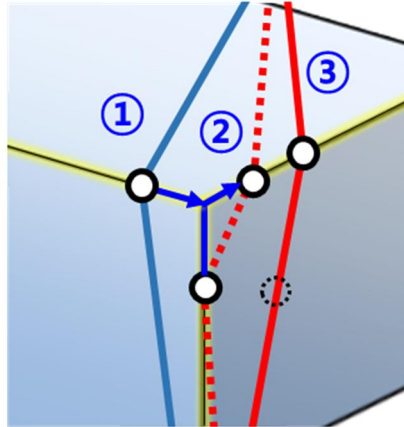


Figure 2-32. A wire rope sliding to the other edges.

Figure 2-32 presents the procedure to update the position of the contact node to slide to the other edges. Firstly, the final point P' that the contact node moves to is calculated. If the final point does not exist on the edge and located on the extension of the edge, the contact node moves to the end of the edge. Then, the contact node is split into several nodes located at the other edges that share the same vertex (② in Figure 2-32). This is the intermediate state of the contact nodes. Next, the contact force calculation and node removal procedure are performed for the contact nodes at the intermediate state. Finally, the intermediate nodes that the normal of the contact force is negative are removed. The final contact node and the wire rope is as shown in ③ in Figure 2-32.

2.3.3. Friction model

When the body and the wire rope have relative motion stated above, the frictional forces are exerted between them. For this, the static and kinematic frictional force should be calculated.

(1) Friction along the wire rope

If a body slides along the wire rope, the frictional force is exerted to the body to restrain the motion. In the Coulomb friction model, the frictional force is divided into two, static and kinematic friction. To simulate static friction when sliding along the wire rope (Figure 2-33), an additional constraint is applied as follows.

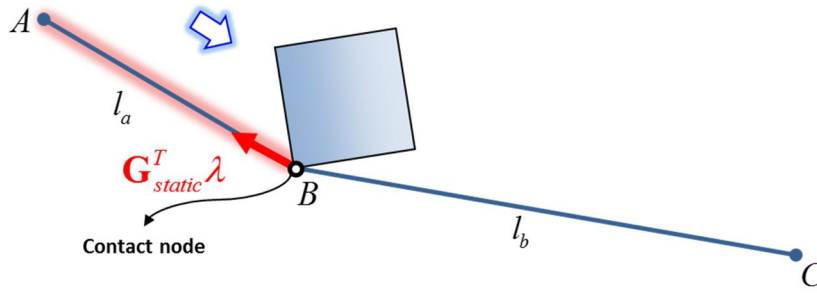


Figure 2-33. Static frictional force exerted on the body sliding along the wire rope.

$$\mathbf{g}_{static}(\mathbf{q}) = l_a - (l_a + l_b) \times \left(\frac{l_{a,initial}}{l_{initial}} \right) = 0. \quad (66)$$

Eq. (66) is the static friction constraint, which calculates the sliding velocity of the contact node B , considering the stretching of the whole wire rope. It implies that the contact node does not slide along the wire rope. If the contact node is firstly detected, the static constraint is created immediately. With this constraint, the contact node does not slide along the wire rope, and the block is stuck. The constraint force (Eq. (67)) then becomes the static frictional force exerted on the contact node and the body.

$$\mathbf{F}_{static} = \mathbf{G}_{static}^T \boldsymbol{\lambda}. \quad (67)$$

As shown in Figure 2-33, the constraint force is exerted with the direction to stop sliding of the contact node. If the constraint force exceeds the maximum static friction force, which is obtained from the static frictional coefficient μ_s (Eq. (68)), the static friction constraint is removed, and the kinetic frictional force is exerted.

$$|\mathbf{F}_{static}| \geq \mu_s |\mathbf{F}_{normal}|. \quad (68)$$

The kinetic frictional force is calculated by multiplying the kinetic frictional coefficient μ_k and the normal force.

$$\mathbf{F}_{kinetic} = \mu_k \cdot |\mathbf{F}_{normal}| \cdot {}^E \mathbf{t} = \mu_k \cdot F_N \cdot {}^E \mathbf{t}. \quad (69)$$

The normal force F_N is the constraint force exerted in the normal direction of the body edge, which is calculated in Eq. (65). Vector ${}^E \mathbf{t}$ is a unit vector that is the direction of the kinetic frictional force. The unit vector has the opposite direction of the projection of the relative velocity of the body at the tangential plane (Figure 2-34).

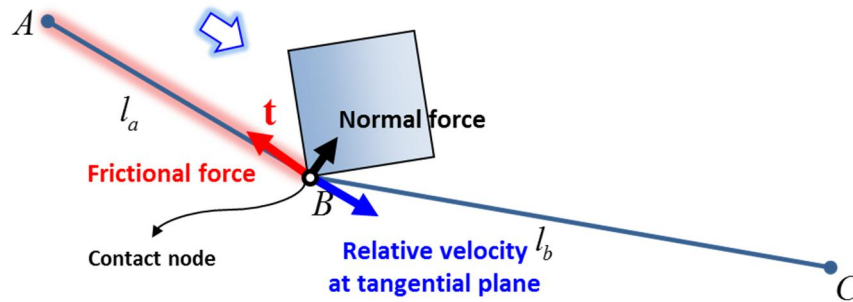


Figure 2-34. Kinetic frictional force exerted on the body sliding along the wire rope.

(2) Friction along the edge

When the wire rope is sliding along the edge of the body, the frictional force is exerted on the contact node. If the static friction force is exerted, the contact node of the wire rope is calculated as a fixed point on the body. The location of the contact node is expressed as a local vector of the body and fixed on the edge. Then, the static frictional force exerted on the contact node is calculated as the projection of the constraint force on the edge direction.

If the static frictional force exceeds the maximum value as in Eq. (68), the contact node starts to slide along the edge. As the wire rope is modeled with constraint in this study, not a massive body, the motion of the contact node with frictional force is approximated. As presented in Figure 2-35, the contact node moves to the final point obtained in Figure 2-31 by a specific ratio [1].

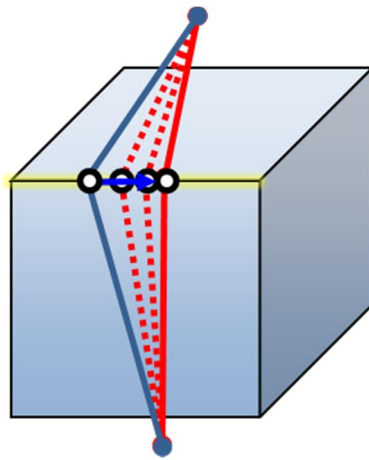


Figure 2-35. Contact node sliding along the edge with frictional force.

The position of the contact node is then calculated as follows.

$$P_{next} = P + \alpha(\mu_k)(P' - P). \quad (70)$$

P' is the final location that minimizes the length of the wire rope, and P and P_{next} is the present and next location of the contact node. α is the ratio of moving, which is the function of the kinematic friction coefficient. The ratio is linearly decreased from 1 to 0 as the kinematic friction coefficient increases from 0 to 1.

2.3.4. Case studies

To test the contact, sliding, and friction model, some test cases are performed.

(1) Tilted box dropping

Three cases are performed to test the static friction model. In case 1-1 and case 1-2, the motion of a tilted box dropped on the wire rope with and without static friction are

compared. The motion of the box is depicted in Figure 2-36. In case 1-1, the box spins on the same place infinitely, as there is no friction between the box and the wire rope. If there is static friction between them, in case 1-2, the torque induced by the static friction force is exerted to the box. Then, the box rotates with the contact node as the center and stops at the end. Figure 2-36 shows that the position of the box is unchanged in case 1-1, and moves in the right direction in case 2-2.

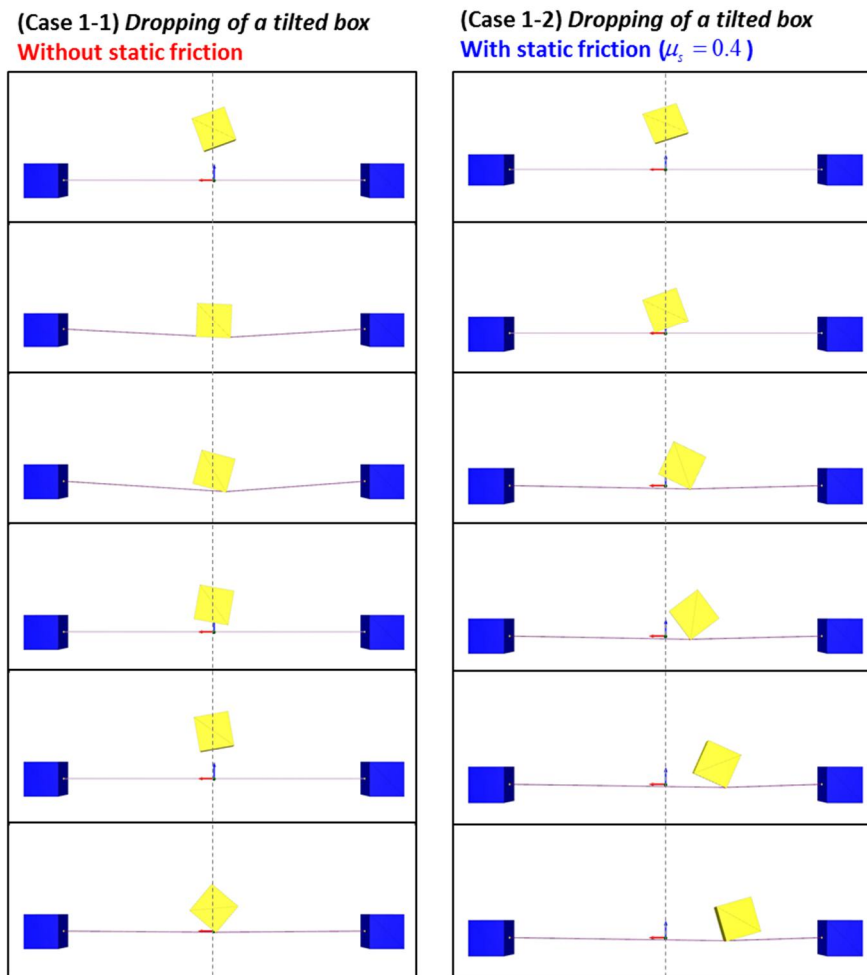


Figure 2-36. Motion of a tilted box dropped on the wire rope.

The same case is performed with a bunny model, which is composed of complex meshes with a convex and concave shape. The static friction is included in this case.

(Case 1-3) Dropping of a tilted bunny
With static friction ($\mu_s = 0.4$)

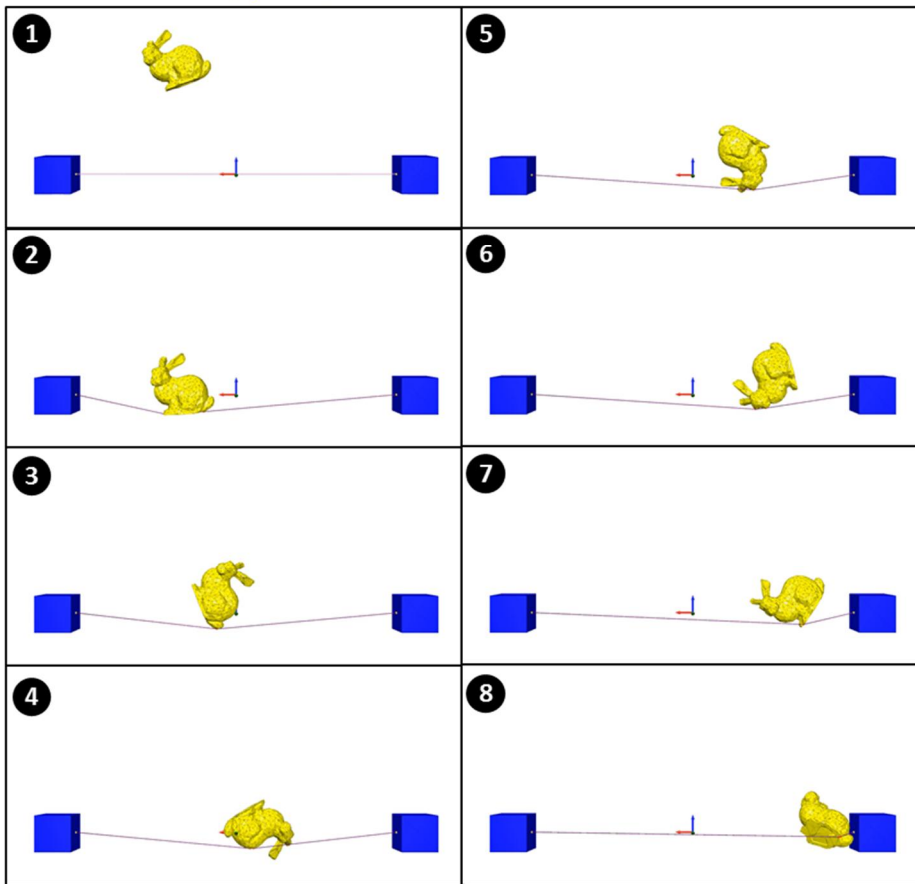


Figure 2-37. Motion of a bunny dropped on the wire rope.

As in case 1-2, the bunny rotates with a contact node as a center and moves to the end of the wire rope. The contact nodes are properly detected along the curved surface of the bunny model.

(2) Body sliding along the wire rope

To test the kinetic friction model, the motion of the body sliding along the tilted wire rope is compared in two cases (Figure 2-38). Without kinetic friction, the box slides along the wire rope until the end. If there is a kinetic frictional force exerted on the box, the sliding speed is reduced as time goes by and stops in the middle.

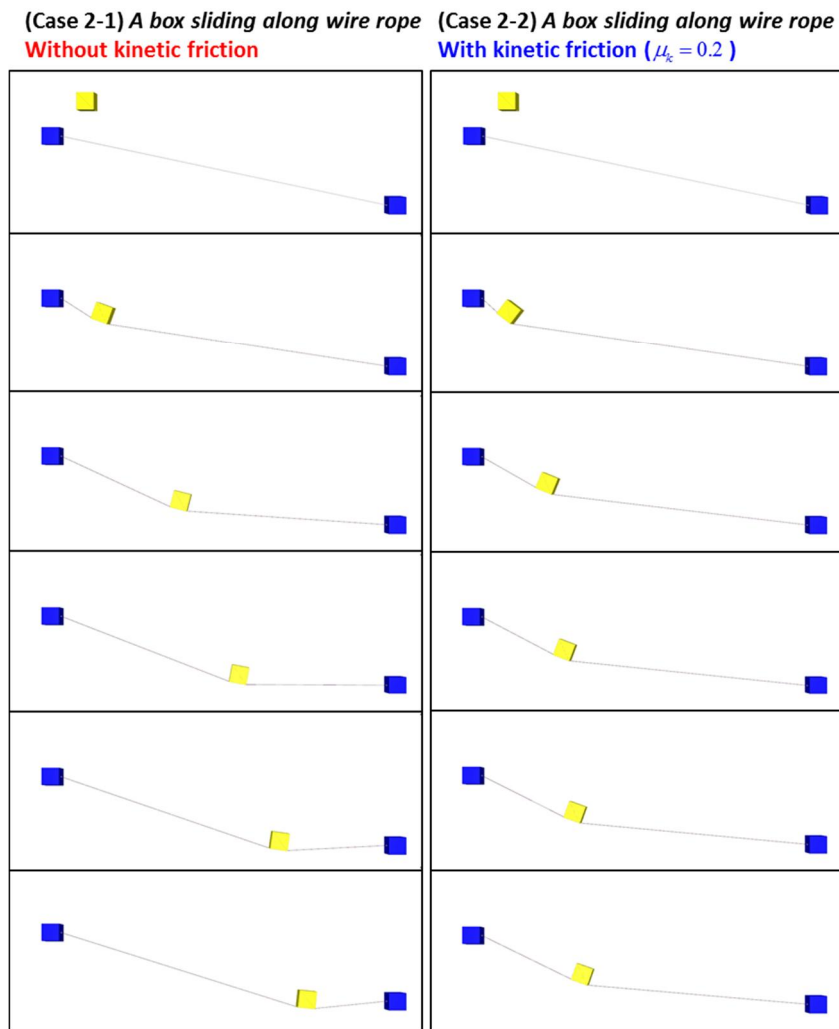


Figure 2-38. Motion of a box sliding along the wire rope.

(3) Dropping of a body between wire ropes

In the sliding model, the contact node is split into several nodes as the wire rope slides to the other edges on the body. To test the sliding model, two cases are simulated to see the motion of the contact node and the body. The test cases are applied to a body with complex meshes such as a sphere and a bunny model. The body is dropped through two wire ropes, and the wire rope slides by the curve of the bodies. Figure 2-39 presents the result of a test case 3-1 with a sphere model.

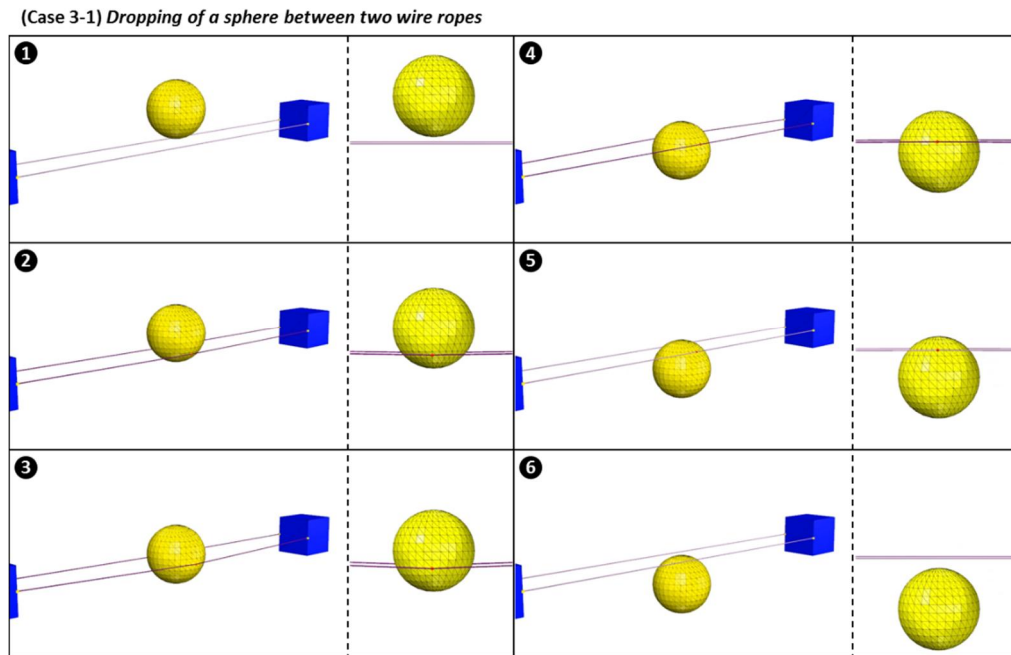


Figure 2-39. Motion of a sphere dropped between two wire ropes.

As presented, the contact nodes are created on the sphere as the wire rope touches the body. Then, the sphere passes through the wire rope, and the contact node slides along several edges. The case 3-2 with a bunny model is as shown in Figure 2-40.

(Case 3-2) Dropping of a bunny between two wire ropes

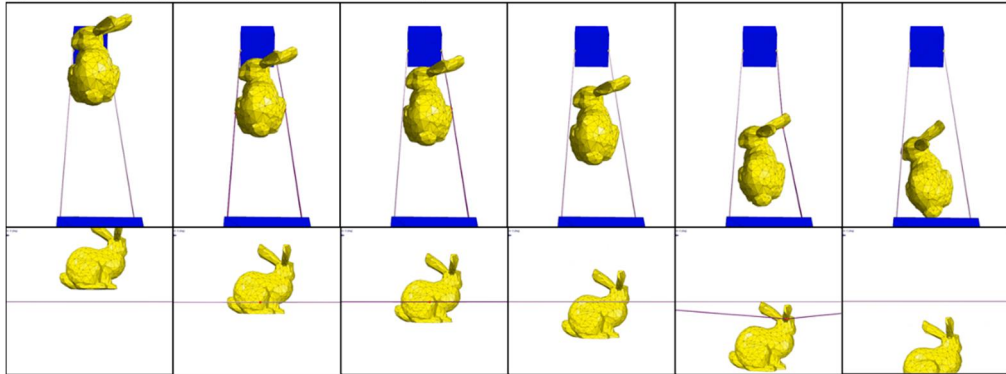


Figure 2-40. Motion of a bunny dropped between two wire ropes.

In this case, the contact node moves along the edges with different directions of the bunny model. In the end, the ear of the bunny is caught in a wire rope and then slides down.

2.4. Contact between mooring line and the seabed

During the simulation, the interaction between the mooring line and the seabed should be considered, as the end of the mooring line is laid on the seabed. Moreover, the friction between them plays an important role in keeping the position of the floating body under the current. In this part, the contact constraints of the mooring line and the seabed are formulated, and the friction between them is introduced in a model.

2.4.1. Collision

Existing studies [49], [15], [16], [17] modeled the contact between the mooring line and the seabed by using the linear springs connecting each node and the seabed. However, this method is not appropriate for the elements using a 3rd order shape function. The mooring line and the seabed are modeled as a flexible body and a rigid body, respectively. The contact between them can be detected, and simulated by using the contact algorithm between rigid and flexible body. However, in the specific case of the mooring line and the seabed, the contact can be modeled as constraints, which can reduce the simulation time much more. In this study, we suggested two constraints to model the contact: the non-interpenetration constraint and the slope constraint.

(1) Non-interpenetration constraint

The non-interpenetration constraint restrains the vertical position of each node, as the linear springs in the existing method. Figure 2-41 shows the application of the non-interpenetration constraint.

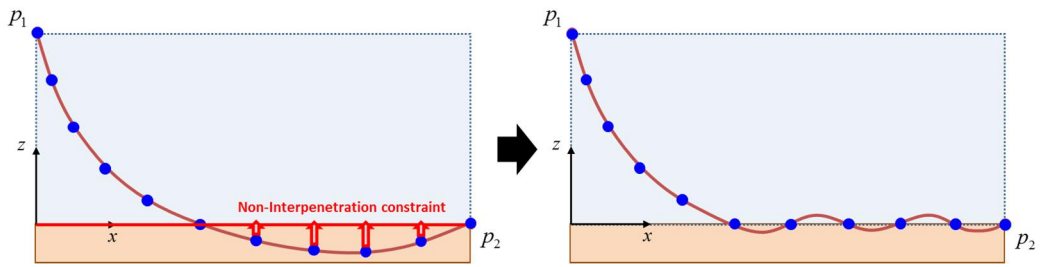
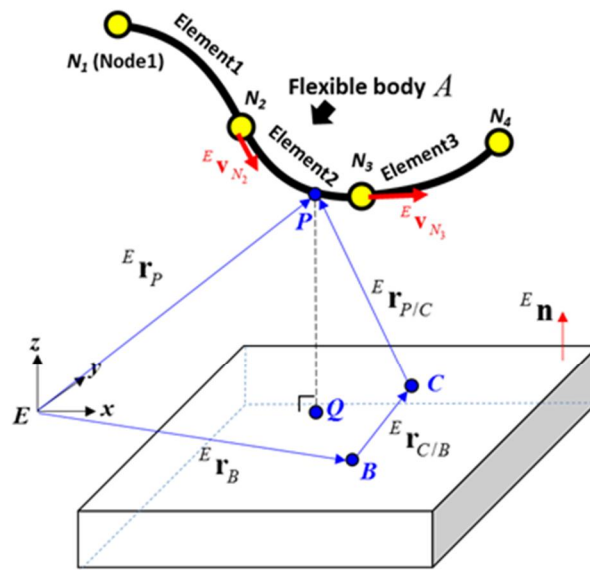


Figure 2-41. Non-interpenetration constraint.

As the beam elements composing the mooring line are modeled using a 3rd order shape function, the buckling of the mooring line can occur. To solve this problem, additional constraint to restrain the slope is required.



- B** : Body center point
- C** : Body fixed point on the plane
- $E \mathbf{n}$: Normal vector of the plane

Figure 2-42. The configuration of the non-interpenetration constraint.

The constraint equations can be derived as follows. Figure 2-42 shows the flexible body A , which is the mooring line, and the seabed B . The normal vector of the seabed plane is given as \mathbf{n} . For the non-interpenetration condition, the distance of the perpendicular line between the two bodies, PQ , should be positive. The non-interpenetration constraint g^1 on each node is derived as an inequation as follows.

$$\begin{aligned}
g^1 &= {}^E \mathbf{n} \cdot {}^E \mathbf{r}_{P/C} \\
&= {}^E \mathbf{n} \cdot ({}^E \mathbf{r}_{P,flexible} - {}^E \mathbf{r}_C) \\
&= {}^E \mathbf{n} \cdot \left\{ \mathbf{S}(\xi) \mathbf{q}_A - ({}^E \mathbf{r}_B + {}^E \mathbf{r}_{C/B}) \right\} \\
&= {}^E \mathbf{R}_B {}^B \mathbf{n} \cdot \left\{ \mathbf{S}(\xi) \mathbf{q}_A - ({}^E \mathbf{r}_B + {}^E \mathbf{R}_B {}^B \mathbf{r}_C) \right\} > 0
\end{aligned} \tag{71}$$

In the existing contact model, the contacts between the mooring line and the seabed are regarded as the external forces exerted by the springs. However, to include the constraint equations to the Discrete Euler-Lagrange equation, the Jacobian matrix of the constraints needs to be calculated. The Jacobian matrix of the non-interpenetration constraint can be derived as follows.

$$\begin{aligned}
\frac{\partial g^1}{\partial \mathbf{q}} &= \begin{bmatrix} \frac{\partial g^1}{\partial ({}^E \mathbf{q}_A)} \\ \frac{\partial g^1}{\partial ({}^E \mathbf{r}_B)} \\ \frac{\partial g^1}{\partial ({}^E \boldsymbol{\omega}_B)} \end{bmatrix}^T = \begin{bmatrix} \mathbf{S}(\xi)^T {}^E \mathbf{n} \\ -{}^E \mathbf{n} \\ -(\mathbf{S}(\xi)\mathbf{q} - {}^E \mathbf{r}_B) \times {}^E \mathbf{n} \end{bmatrix}^T \\
&= \begin{bmatrix} {}^E \mathbf{n}^T \mathbf{S}(\xi) & (-{}^E \mathbf{n})^T & -(\mathbf{S}(\xi)\mathbf{q} - {}^E \mathbf{r}_B)^T {}^E \tilde{\mathbf{n}} \end{bmatrix} \\
&= [\mathbf{G}_{A,N_2N_3}^1 \quad \mathbf{G}_B^1]
\end{aligned} \tag{72}$$

(2) Slope constraint

The slope constraint restrains the slope of each element in the z-direction from making the mooring line lay down to the seabed. Figure 2-43 presents the application of the non-penetration constraint and slope constraint to model the contact with the seabed.

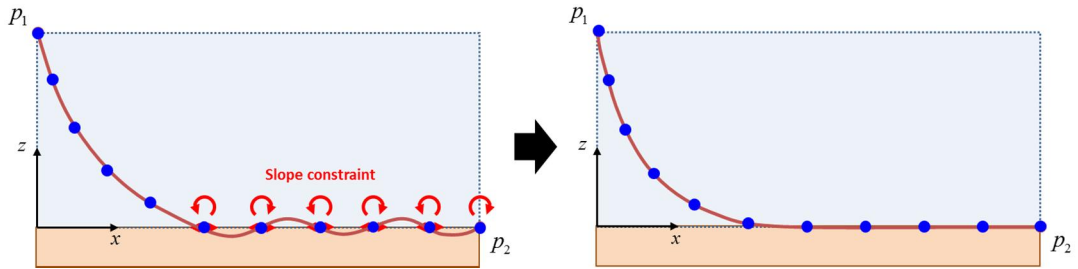
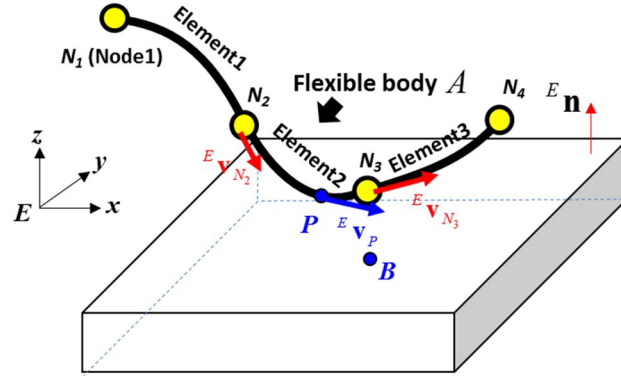


Figure 2-43. Slope constraint.

If the contact between the flexible body and the seabed at point P (Figure 2-44), the slope vector at the contact point should be parallel to the seabed. It means that the slope vector of point P should be perpendicular to the normal vector of the seabed \mathbf{n} .



B : Body center point
 $E \mathbf{n}$: Normal vector of the plane

Figure 2-44. The configuration of the slope constraint.

Therefore, the slope constraint g^2 yields the following equation.

$$\begin{aligned}
 g^2 &= {}^E \mathbf{v}_P \cdot {}^E \mathbf{n} \\
 &= \mathbf{S}_\xi \mathbf{q} \cdot {}^E \mathbf{n} = 0
 \end{aligned}
 \quad .$$

$$\left(\begin{array}{c}
 {}^E \mathbf{v}_P = \frac{d\mathbf{S}}{d\xi} \mathbf{q} = \mathbf{S}_\xi \\
 \left[\begin{array}{c}
 {}^E \mathbf{r}_{N_3} \\
 {}^E \mathbf{v}_{N_3} \\
 {}^E \mathbf{r}_{N_4} \\
 {}^E \mathbf{v}_{N_4}
 \end{array} \right]
 \end{array} \right) \quad (73)$$

The slope vector at point P can be obtained using a derivation of the shape function and the nodal coordinates. The Jacobian function of the slope constraint is calculated as the following equation.

$$\begin{aligned}
\frac{\partial \mathbf{g}^2}{\partial \mathbf{q}} &= \begin{bmatrix} \frac{\partial \mathbf{g}^2}{\partial ({}^E \mathbf{q}_A)} \\ \frac{\partial \mathbf{g}^2}{\partial ({}^E \mathbf{r}_B)} \\ \frac{\partial \mathbf{g}^2}{\partial ({}^E \boldsymbol{\omega}_B)} \end{bmatrix}^T = \begin{bmatrix} \mathbf{S}_\xi^T {}^E \mathbf{n} \\ \mathbf{0} \\ -\mathbf{S}_\xi \mathbf{q} \times {}^E \mathbf{n} \end{bmatrix}^T \\
&= \begin{bmatrix} {}^E \mathbf{n}^T \mathbf{S}_\xi & \mathbf{0} & -(\mathbf{S}_\xi \mathbf{q})^T {}^E \tilde{\mathbf{n}} \end{bmatrix} . \\
&= [\mathbf{G}_{A,N_2,N_3}^2 \quad \mathbf{G}_B^2]
\end{aligned} \tag{74}$$

Two constraints are suggested in this study, which is appropriate for the flexible body using a 3rd order shape function. Figure 2-45 compares the profile of the mooring line by adopting the existing and the suggested contact model with the seabed. The existing model shows the buckling, especially at the end of the part of the mooring line on the seabed. Due to the slope constraint, the mooring line on the seabed is stretched in the suggested model. Here, the connected floating body is assumed to be fixed.

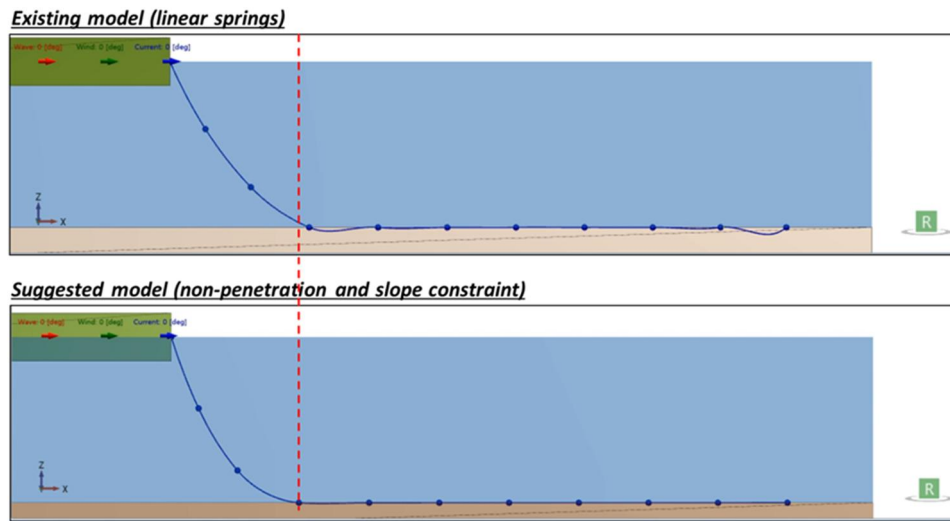


Figure 2-45. Comparison between the existing and suggested contact model.

(3) Penetration depth

With the constraints suggested above, the mooring line does not penetrate the seabed and remain stretched. However, as the seabed is not a rigid body in the real world, the mooring line can penetrate inside the seabed due to its own weight. The penetration depth varies according to the property of the material and the composition of the seabed. In the existing simulations, the stiffness of the seabed is generally given as an input to consider the material property of the seabed. Likewise, although the contact between the mooring line and the seabed is expressed as constraint equations, they can be violated according to the property of the seabed. In the final form of the Discrete Euler-Lagrange equation with constraints (Eq. (11)), the regularization term ε determines how strongly the constraints should be satisfied. ε has the same value with the inverse number of the spring stiffness in the existing model. Therefore, the stiffness of the seabed can be considered as the input data in the suggested model.

2.4.2. Friction

The frictional force between the mooring line and the seabed has a great influence on the behavior of the mooring line. The frictional force on the seabed has been studied for a long time by many researchers. The Coulomb friction model, using the static and the dynamic friction coefficient, has been widely adopted. However, as the friction coefficient has been proven to be the function of the relative velocity between two bodies by Bowden and Tabor [50], the modified Coulomb friction model was introduced. The modified Coulomb friction model approximates the Coulomb friction model to a continuous function (Figure 2-46). The modified Coulomb friction model has been used in various types of commercial software, with the advantages of numerical stability and efficiency. Nevertheless, the model has a problem in that it cannot realize sticking, and slow slippage always occurs between bodies with constant velocities [51].

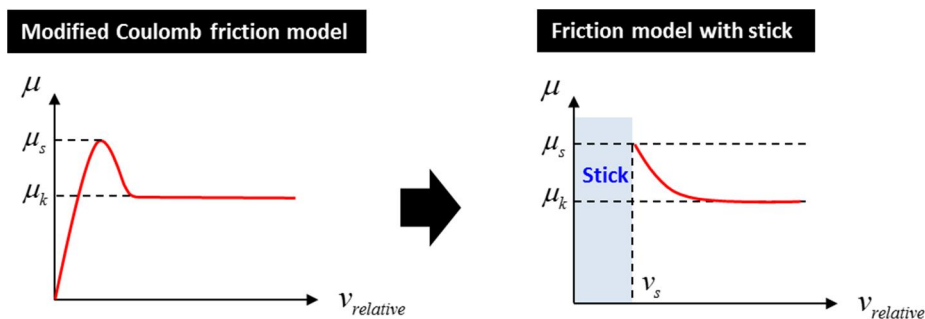


Figure 2-46. Modified Coulomb friction model and the friction model with stick.

To solve this problem, Choi and Yoo [52] suggested a friction model that realizes stick using the concept of elastic deformation of the body, as presented in Figure 2-47. In this model, the sticking is modeled using the spring-damper system. The stick stiffness can be obtained using the elastic deformation limit of the object. As the relative

displacement between two bodies exceeds the elastic deformation limit, the object starts to slide.

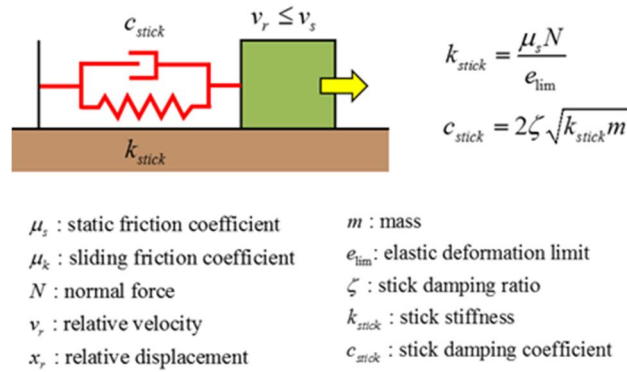


Figure 2-47. Friction model for sticking.

2.4.3. Case studies

(1) Mooring line under the current

With the calculated current force and contact model, the motion of the mooring line is obtained under the current with or without the frictional force at the seabed. The current speed is 2.0 m/s at the surface, and the barge is assumed to be fixed to space. The static and sliding friction coefficients are 0.98 and 0.74, which are the recommended friction coefficient between chain and sand by Taylor and Valent [53]. The results are shown in Figure 2-48 and Figure 2-49.

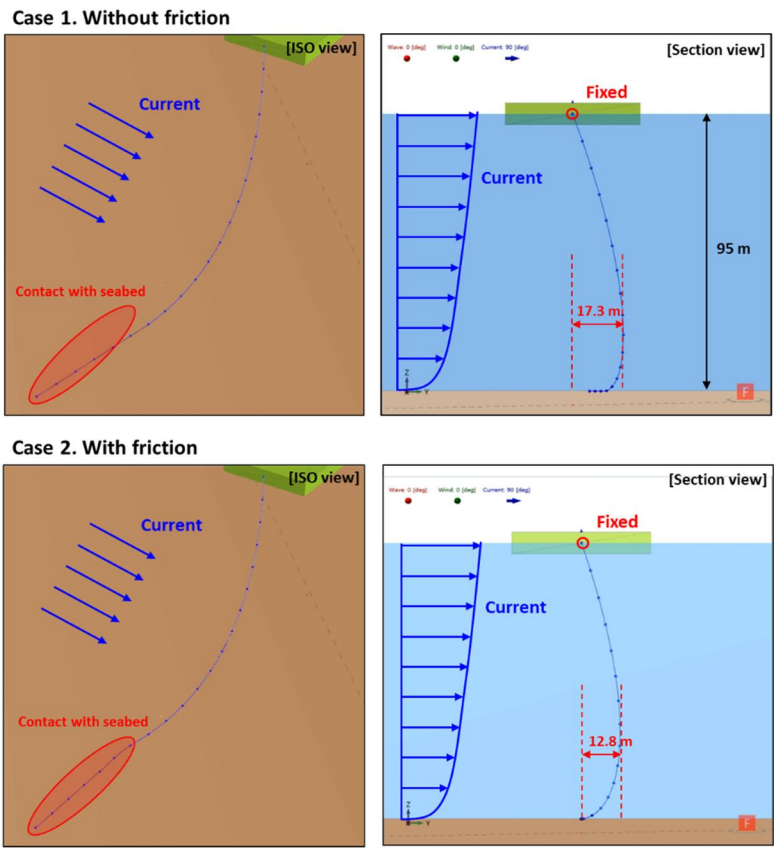


Figure 2-48. The motion of the mooring line under the current.

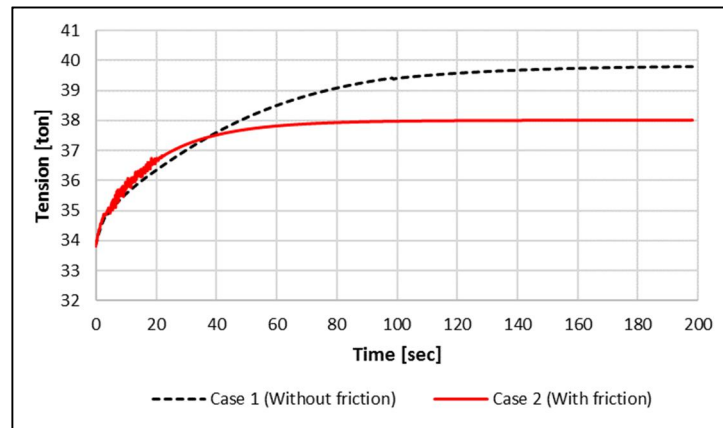


Figure 2-49. The tension of the mooring line under the current.

As shown, the frictional force between the seabed and the mooring line plays an important role in the case of an existing current. The deflection of the mooring line to the current direction is 17.3 m, and 12.8 m, respectively, for each case. In case 2, the mooring line on the seabed does not move due to the friction. The tension of the mooring line increases with the application of the current in both cases. The maximum value is 40 tons and 38 tons for each case, respectively.

(2) Mooring line with periodic motion

To check the dynamic effect of the suggested mooring line, the periodic motion is given to the floating barge connected to the mooring line. The motion of the mooring line and the tension are compared with that of the analytic solution, which cannot consider the dynamic effect. The amplitude and the period of the motion of the barge are set to be 3 m and 4 seconds, respectively. Fig. 22 shows the motion of the mooring line. Two cases are simulated based on the mooring line model. The weight per length of the mooring line is 203.9 kg/m, and the axial stiffness is 205,200 kN.

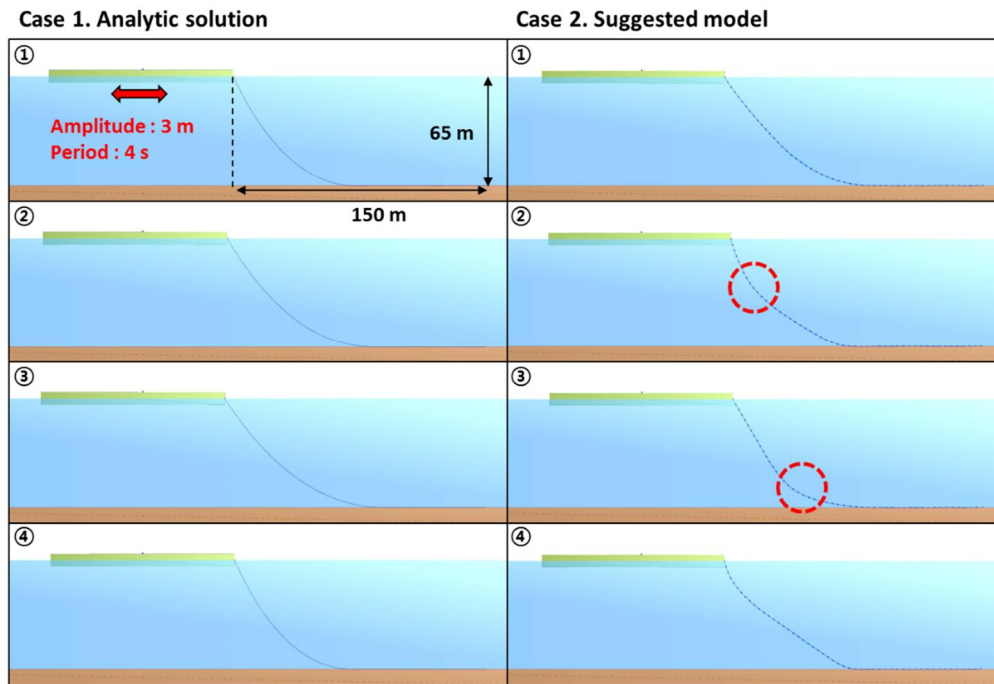


Figure 2-50. The motion of the mooring line connected to the floating barge with periodic motion.

The first case shows the result of a quasi-static analysis using an analytic solution, which neglects the effect of inertial and damping forces. The velocity of the mooring line is assumed infinitesimally small at each time step, and only the position of the mooring line is updated. On the other hand, the dynamic effects are considered in case 2. As indicated by red circles in Figure 2-50, the snapping effect can be investigated due to the inertial force of the mooring line. Then, the tension at the fairlead of each case is obtained, as shown in Figure 2-51.

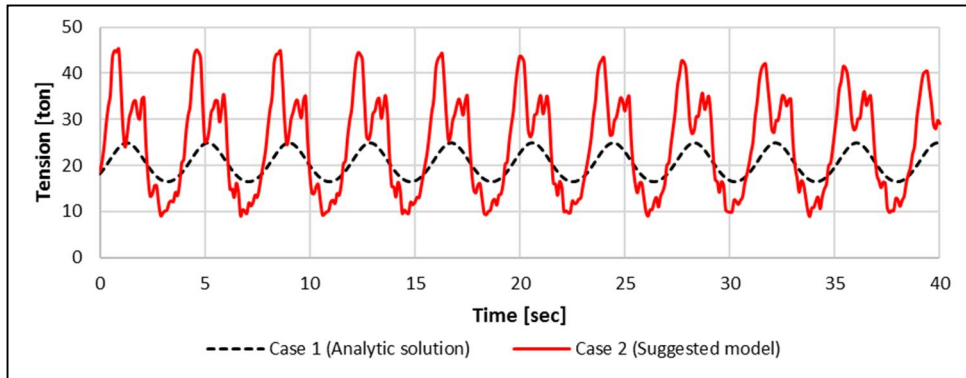


Figure 2-51. Tension at the fairlead of the floating barge with periodic motion.

Due to the snapping effect, the tension of the suggested mooring line model is irregular, and the amplitude of the oscillation is much higher than that of the analytic solution. Therefore, for the accurate prediction of the motion of the mooring line and the floating body, the dynamic effect should be considered.

2.5. Control of the underactuated system

2.5.1. Underactuated mechanical system

A mechanical system can be classified into three; overactuated, fully actuated, and underactuated mechanical system, according to the relationship between the number of the independent control inputs and the degrees of freedom [54]. If the number of control inputs is more than the degrees of freedom, it is an overactuated system, and a fully actuated system if it is the same. If the number of control inputs is more than the degrees of freedom, the system is underactuated.

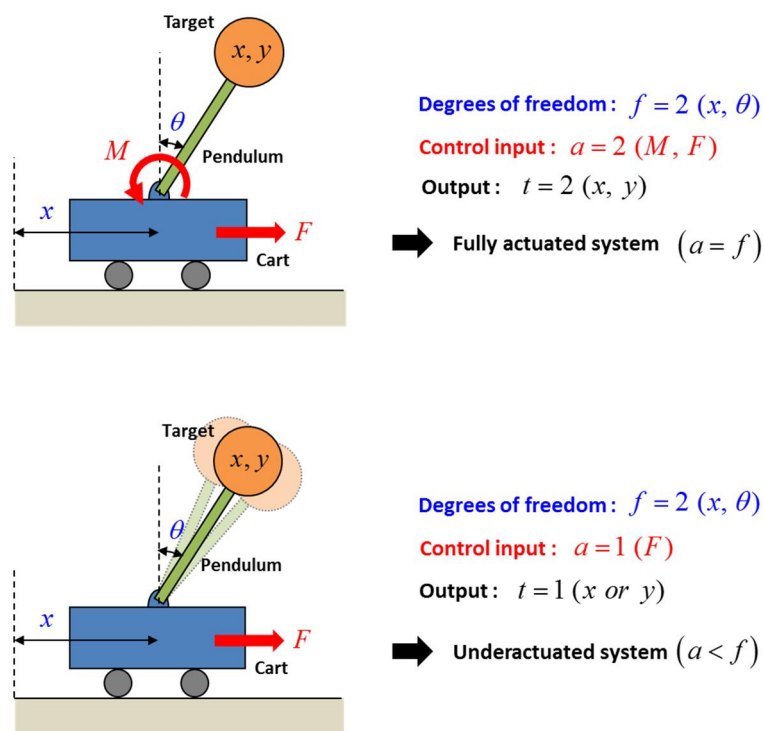


Figure 2-52. Two-dimensional inverted pendulum with different control inputs.

Figure 2-52 shows an example of a two-dimensional inverted pendulum with a different number of control inputs. The target output is the location of the orange object, x and y . The inverted pendulum has two degrees of freedom, which is the motion of the cart in the x -direction and the angle of the pendulum. If there are two control inputs to control both, the system can control the exact location of the target, and the system is fully actuated. On the other hand, if there is only one control input that controls the motion of the cart, the system is an underactuated system. The system can only control x or y position of the target output. In this system, the target can rotate with one degree of freedom.

In a fully actuated and an overactuated system, all degrees of freedom can explicitly be regulated by available controls. However, in the underactuated system, the target output is not determined by the control input. The underactuation makes the inverse dynamics control problem more challenging, as the control inputs cannot be solved from the dynamic equations by model inversion due to the invertible matrix [55]. Therefore, many traditional non-linear control methods are not directly applicable to this system.

The examples of the underactuated system include mobile robot, spacecraft, underwater vehicle, surface vessel, helicopter, space robot, and underactuated manipulator [56]. Typically, cranes are the underactuated system, as there is no direct influence of the actuators on the swinging payload [57]. Though the motion of the top mounting point of the wire rope can be controlled directly, the motion of the payload is not determined with the control inputs, but it is defined by the dynamics of the system. As presented in Figure 2-53, the block connected to the wire ropes of cranes can have swinging motion due to the dynamics of the system, even when the control inputs of the cranes are given.

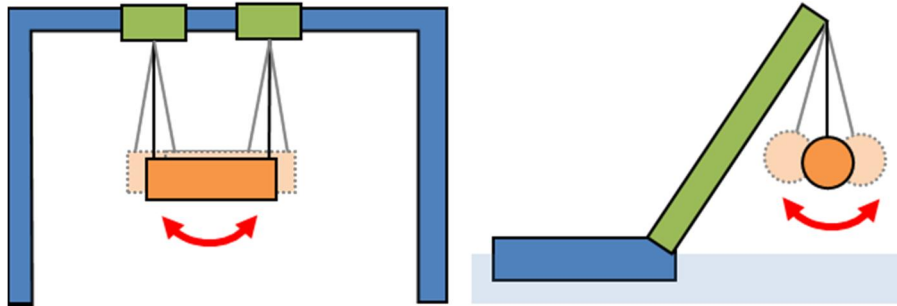


Figure 2-53. Examples of the underactuated crane system in shipyards.

2.5.2. Trajectory tracking control

The control of the underactuated mechanical system (UMS) aims to find a control law that controls the target output in the presence of modeling uncertainties and external disturbances. The purpose of the UMS control can be divided into two main categories: set-point regulation and trajectory tracking [56]. A set-point regulation is to control the output to maintain a certain position or orientation by stabilizing the equilibrium state. It is a well-defined control issue, and the control methods such as PBC (Passivity Based Control) can be adopted. However, the trajectory tracking, which is to control the target output to track the desired trajectory, is still a challenging topic. For the block erection operation, which is the target application in this study, the trajectory tracking control of the block is required.

(1) Servo constraint

For the trajectory tracking control, the application of so-called servo constraints is a very appealing and efficient approach [58], [59]. The desired system outputs can be described in terms of the system states and modeled as servo constraints, which can be

imposed onto the controlled system as additional constraint functions (Figure 2-54).

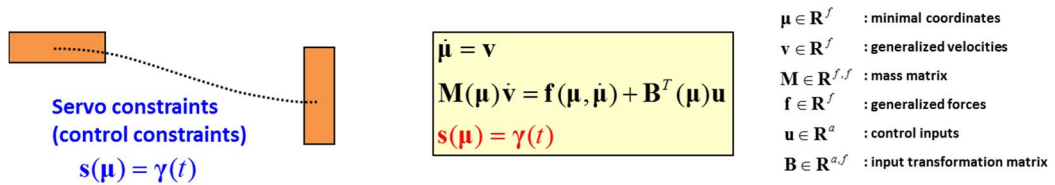


Figure 2-54. Application of the servo constraint.

The servo constraint, also called control constraint, then force the exact reproduction of the desired trajectory.

(2) Motion planning

The servo constraint is formulated by the desired trajectory that connects the initial and final orientation. In block erection operation, the desired position and orientation of the block are given at first, and the trajectory of the block is created by a smooth path to the final state. The translational motion of the block $\boldsymbol{\gamma}_r$ can be modeled as a straight line from initial to the final position as follows,

$$\boldsymbol{\gamma}_r(t) = \boldsymbol{\gamma}_{r0} + (\boldsymbol{\gamma}_{rf} - \boldsymbol{\gamma}_{r0})c(t), \quad (75)$$

where $\boldsymbol{\gamma}_{r0}$ and $\boldsymbol{\gamma}_{rf}$ is the initial and final position. For the smooth motion of the block, the interpolation function $c(t)$ is used. It is composed of three phases including acceleration and deceleration time, and the velocity is constant between them (Figure 2-55).

$$c(t) = \begin{cases} c_I(t) & \text{for } t_0 \leq t < \tau_0 \\ c_{II}(t) & \text{for } \tau_0 \leq t < t_f - \tau_0 \\ c_{III}(t) & \text{for } t_f - \tau_0 \leq t < t_f \end{cases} \quad (76)$$

$$\left(\begin{array}{l} \tau = t_f - t_0 \\ \tau_0 : \text{acceleration/deceleration time} \end{array} \right)$$

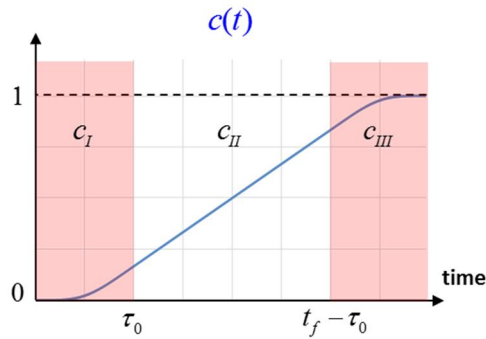


Figure 2-55. Interpolation function for motion planning.

The rotational motion of the block can be described in the same way by its initial and final orientation, ${}^O\mathbf{R}_a$ and ${}^O\mathbf{R}_e$. The rotational transformation matrix ${}^a\mathbf{R}_e$ can be calculated by the given value,

$${}^a\mathbf{R}_e(\varphi_a, \varphi_e) = {}^O\mathbf{R}_a^T(\varphi_a) {}^O\mathbf{R}_e(\varphi_e) \quad (77)$$

For rotational motion planning, we assume the block rotates from initial to final orientation with a certain axis of rotation \mathbf{e}_{re} and angle s_{re} as illustrated in Figure 2-56.

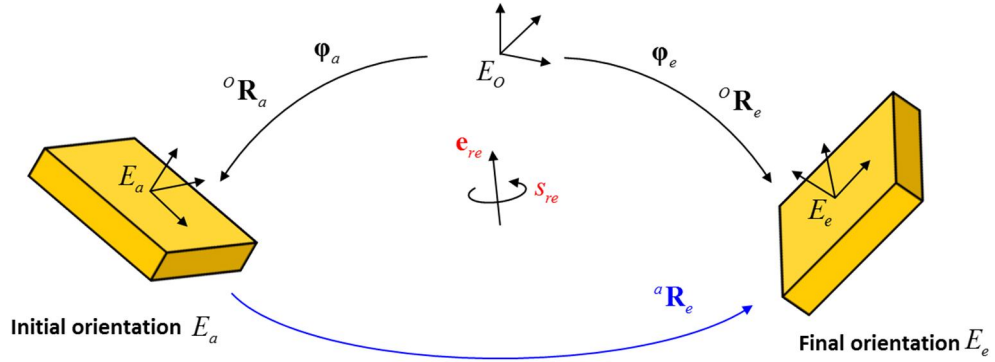


Figure 2-56. Rotational motion of the block from initial to final orientation.

By using the Rodrigues' rotation formula, the rotational transformation matrix is also described by the axis of rotation and angle.

$${}^a\mathbf{R}_e(\mathbf{e}_r, s_{re}) = \cos(s_{re})\mathbf{I}_3 + \sin(s_{re})\tilde{\mathbf{e}}_r + (1 - \cos(s_{re}))\mathbf{e}_r\mathbf{e}_r^T \quad (78)$$

Then, with Eq. (77) and Eq. (78), the rotational axis and angle to obtain the final orientation can be calculated as

$$s_{re} = \arccos\left(\frac{1}{2}\left({}^a\mathbf{R}_e(1,1) + {}^a\mathbf{R}_e(2,2) + {}^a\mathbf{R}_e(3,3) - 1\right)\right)$$

$$\mathbf{e}_r = \frac{1}{\sin(s_{re})} \begin{bmatrix} {}^a\mathbf{R}_e(3,2) - {}^a\mathbf{R}_e(2,3) \\ {}^a\mathbf{R}_e(1,3) - {}^a\mathbf{R}_e(3,1) \\ {}^a\mathbf{R}_e(2,1) - {}^a\mathbf{R}_e(1,2) \end{bmatrix}, \quad (79)$$

where ${}^a\mathbf{R}_e(i, j)$ is i^{th} row and j^{th} column of ${}^a\mathbf{R}_e(\boldsymbol{\varphi}_a, \boldsymbol{\varphi}_e)$. Finally, the rotation trajectory

of the block is formulated as before in Eq. (75), by using the interpolation function.

$$\begin{aligned} \gamma_{\varphi}(t) &= \gamma_{\varphi 0} + (\gamma_{\varphi f} - \gamma_{\varphi 0}) c(t) \\ \left(\begin{array}{l} \gamma_{\varphi}(t_0) = \gamma_{\varphi 0} = 0 \\ \gamma_{\varphi}(t_f) = \gamma_{\varphi f} = s_{re} \end{array} \right) \end{aligned} \quad (80)$$

In summary, the prescribed trajectory that block has to follow is specified by the following equation.

$$\mathbf{x} = \begin{bmatrix} \mathbf{r}(t) \\ \boldsymbol{\varphi}(t) \end{bmatrix} = \begin{bmatrix} \boldsymbol{\gamma}_r(t) \\ \boldsymbol{\varphi}(\gamma_{\varphi}(t)) \end{bmatrix} \quad (81)$$

\mathbf{x} is the target output, and the right side of the equation is the desired trajectory from motion planning.

2.5.3. Dynamic equations

The dynamic equations of the crane system are formulated in this section to find the control input and to predict the actual motion of the system. The target crane system of this study is the gantry crane and the floating crane.

(1) Gantry crane

The gantry crane consists of the crane girder with two legs, the upper and lower trolley, the hooks and equalizers, and the wire ropes. As shown in Figure 2-57, the crane girder moves along the rail on the ground with the direction of the y-axis. Two trolleys are also

connected to the crane girder with slider joints, having the x-axis as the moving axis. The gantry crane system controls the motion of the block through the translational motion of two trolleys and crane girder, and the hoisting of the wire ropes connected to the hook (Figure 2-57).

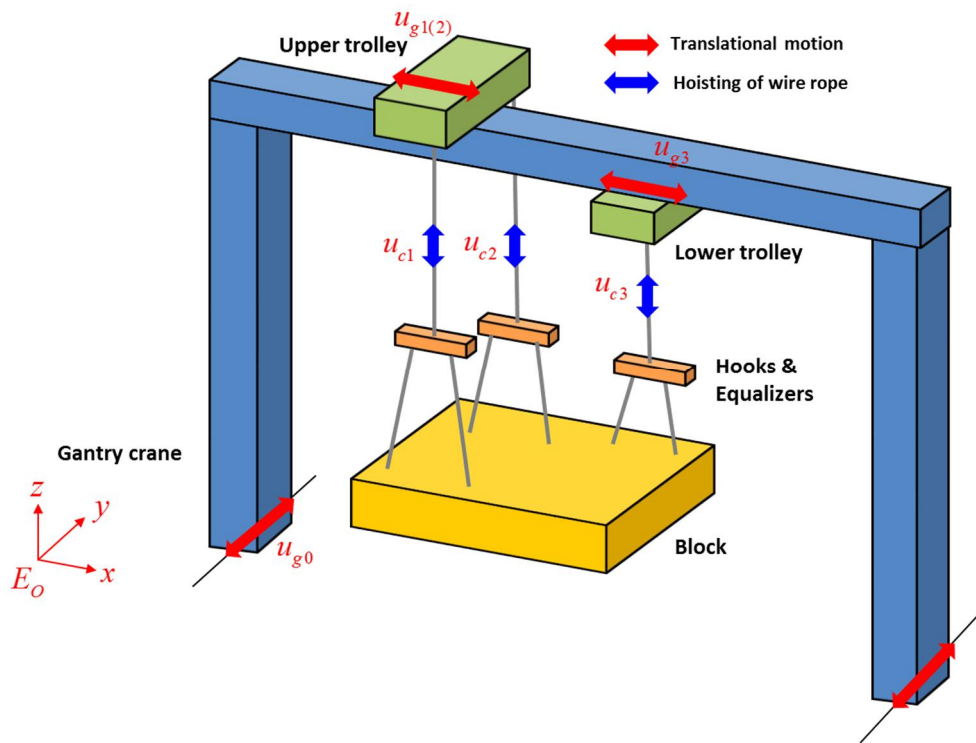


Figure 2-57. Configuration of the gantry crane system.

Meanwhile, in the gantry system, the wire rope is not directly attached to the block, but the equipment called hooks are connected. Three wire ropes connect the trolleys and the hooks that are holding an equipment called an equalizer. Then, several wire ropes from equalizers, also called slings, are connected to the lug of the block.

① Redundant coordinates

The control inputs (\mathbf{u}) of the crane system are expressed as the control force \mathbf{u}_g exerted on the crane girder and trolleys, and the torque \mathbf{u}_c exerted on the winch that each wire rope is connected.

$$\begin{aligned}\mathbf{u} &= \begin{bmatrix} \mathbf{u}_g \\ \mathbf{u}_c \end{bmatrix} \\ \mathbf{u}_g &= [u_{g0} \quad u_{g1(2)} \quad u_{g3}]^T \\ \mathbf{u}_c &= [u_{c1} \quad u_{c2} \quad u_{c3}]^T\end{aligned}\tag{82}$$

With the control inputs, the coordinate \mathbf{p} of the gantry crane then has six variables as shown in Figure 2-58 and Eq. (83).

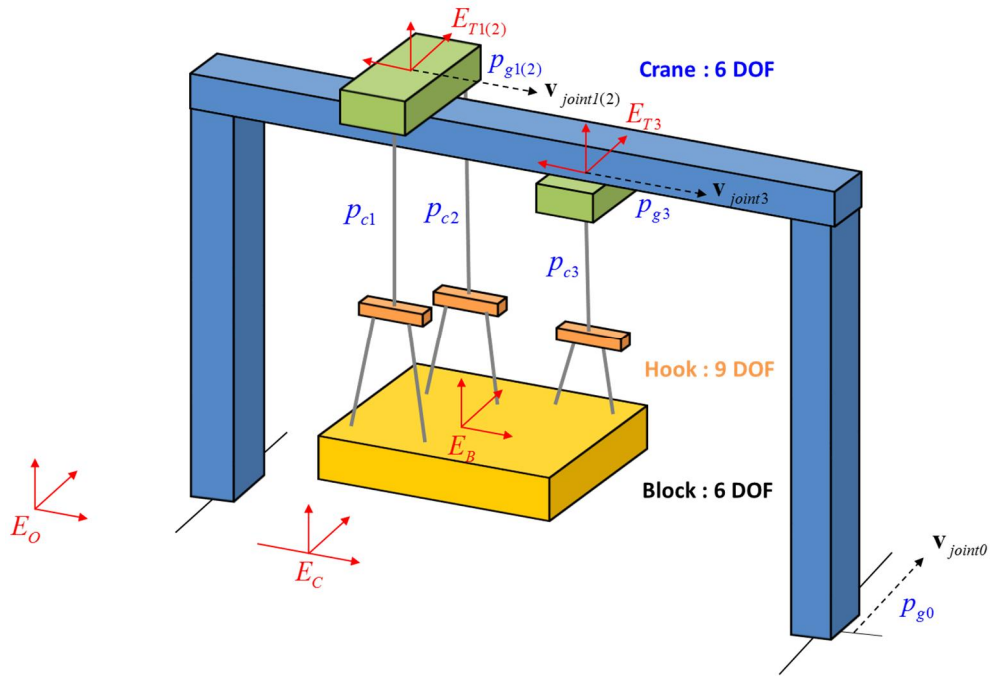


Figure 2-58. Redundant coordinates of the crane system.

$$\begin{aligned}
 \mathbf{p} &= \begin{bmatrix} \mathbf{p}_g \\ \mathbf{p}_c \end{bmatrix} \\
 \mathbf{p}_g &= [p_{g0} \quad p_{g1(2)} \quad p_{g3}]^T \\
 \mathbf{p}_c &= [p_{c1} \quad p_{c2} \quad p_{c3}]^T
 \end{aligned} \tag{83}$$

The crane, trolleys, and block have their local frames, which are represented as E_C , E_{T_i} , and E_B , respectively. The space-fixed frame is expressed as E_O . \mathbf{p}_g is the displacement of the crane girder and trolleys from the initial position with each moving axis. The moving direction, which is the axis of each slider joint, is presented in Figure 2-58 as \mathbf{v}_{joint} . \mathbf{p}_c represents the length of the wire ropes hoisted by the control torque on the winch. Then,

the mass matrix \mathbf{M} and \mathbf{B} for control inputs \mathbf{u} , which generates actuating force $\mathbf{f}_i = -\mathbf{B}^T \mathbf{u}$ is as follows.

$$\mathbf{M}_p = \begin{bmatrix} m_0 & 0 & 0 & 0 & 0 & 0 \\ 0 & m_{1(2)} & 0 & 0 & 0 & 0 \\ 0 & 0 & m_3 & 0 & 0 & 0 \\ 0 & 0 & 0 & \frac{J_1}{r_1^2} & 0 & 0 \\ 0 & 0 & 0 & 0 & \frac{J_2}{r_2^2} & 0 \\ 0 & 0 & 0 & 0 & 0 & \frac{J_3}{r_3^2} \end{bmatrix}, \mathbf{B} = \begin{bmatrix} 1 & & & & & \\ & 1 & & & & \\ & & 1 & & & \\ & & & 1/r_1 & & \\ & & & & 1/r_2 & \\ & & & & & 1/r_3 \end{bmatrix} \quad (84)$$

where m_0 is the mass of the crane girder with two legs, $m_{1(2)}$ and m_3 is the mass of the upper and lower trolley, and J_i and r_i is the moment of inertia and radius of winches.

The hook is modeled as point mass that only described as position. Each hook then has three degrees of freedom and a total of nine degrees of freedom. The hook and equalizer coordinates \mathbf{q} are expressed as follows, where \mathbf{q}_i is the position of each hook. The mass matrix of hook \mathbf{M}_q is expressed as $\mathbf{M}_q = m_q \mathbf{I}_{9 \times 9}$, where m_q is the mass of the hook.

$$\mathbf{q} = \begin{bmatrix} \mathbf{q}_1 \\ \mathbf{q}_2 \\ \mathbf{q}_3 \end{bmatrix} \quad (85)$$

$$\mathbf{q}_i = [q_{xi} \quad q_{yi} \quad q_{zi}]^T$$

As the block has six degrees of freedom, which is the position and orientation with x, y, and z-axis, the crane with six coordinates can control the motion of the block

completely. The block coordinates \mathbf{x} with position \mathbf{r} , and orientation $\boldsymbol{\varphi}$ are:

$$\begin{aligned}\mathbf{x} &= \begin{bmatrix} \mathbf{r} \\ \boldsymbol{\varphi} \end{bmatrix} \\ \mathbf{r} &= [r_x \quad r_y \quad r_z]^T \\ \boldsymbol{\varphi} &= [\varphi_1 \quad \varphi_2 \quad \varphi_3]^T\end{aligned}\tag{86}$$

The mass matrix of the block is then

$$\begin{aligned}\mathbf{M}_b &= \begin{bmatrix} m\mathbf{I}_3 & \mathbf{0} \\ \mathbf{0} & \mathbf{J} \end{bmatrix} \\ \mathbf{J} &= \begin{bmatrix} J_x & 0 & 0 \\ 0 & J_y & 0 \\ 0 & 0 & J_z \end{bmatrix}.\end{aligned}\tag{87}$$

② Constraints

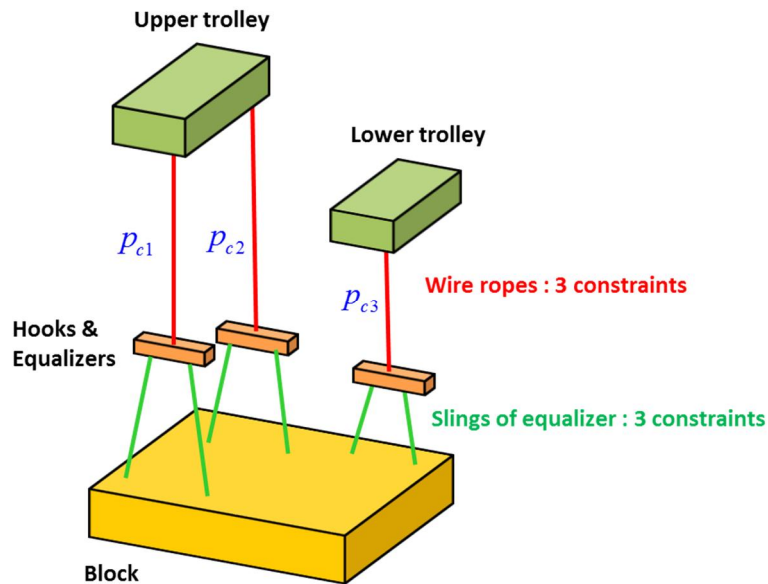


Figure 2-59. Constraints of the crane system.

The motion of the crane system, hooks and equalizers, and the block are restrained with the wire ropes (Figure 2-59). Strictly, the wire rope is not a constraint, which lowers the degrees of freedom of the connected object. The stretching of the wire rope connecting the trolley and the hook can still occur. However, to formulate the dynamic equations for the inverse dynamics solver that calculates the control input, we assume that the wire rope is a constraint such as a rigid beam without stretching. The stretching of the wire rope is considered at the simulation of the actual plant.

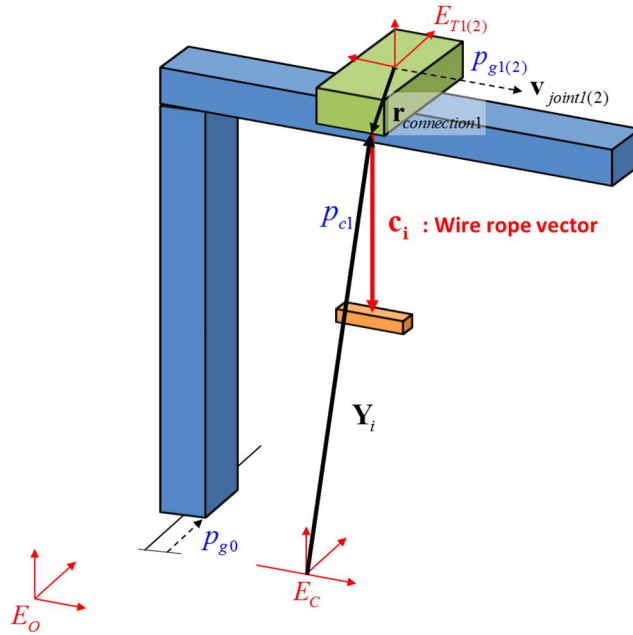


Figure 2-60. Wire rope vector between trolley and hook.

As presented in Figure 2-60, the trolley and hook are connected by a wire rope, which is expressed as a holonomic constraint. With the constraint that the length of the wire rope vector \mathbf{c}_i is the same as the control input p_{ci} , the constraint equation yields the following.

$$\Phi_{1,i}(\mathbf{p}, \mathbf{q}) = \frac{1}{2} (\mathbf{c}_i^T(\mathbf{p}, \mathbf{q}) \mathbf{c}_i(\mathbf{p}, \mathbf{q}) - p_{ci}^2) \quad (88)$$

The wire rope vector is expressed as follows, connecting the hook and the connection point of the trolley.

$$\mathbf{c}_i = \mathbf{r}_{hook} - \mathbf{r}_{trolley} = (\mathbf{q}) - (\mathbf{r}_C + \mathbf{p}_i) = (\mathbf{q}) - (\mathbf{r}_C + {}^O\mathbf{R}_C \mathbf{Y}_i)$$

$$\left(\begin{array}{l} \mathbf{Y}_1 = {}^C\mathbf{r}_{T1} + {}^C\mathbf{R}_{T1} {}^{T1}\mathbf{r}_{connection1} = {}^C\mathbf{r}_{T1,init} + p_{g0} {}^C\mathbf{v}_{joint0} + p_{g1} {}^C\mathbf{v}_{joint1} + {}^C\mathbf{R}_{T1} {}^{T1}\mathbf{r}_{connection1} \\ \mathbf{Y}_2 = {}^C\mathbf{r}_{T2} + {}^C\mathbf{R}_{T2} {}^{T2}\mathbf{r}_{connection2} = {}^C\mathbf{r}_{T2,init} + p_{g0} {}^C\mathbf{v}_{joint0} + p_{g2} {}^C\mathbf{v}_{joint2} + {}^C\mathbf{R}_{T2} {}^{T2}\mathbf{r}_{connection2} \\ \mathbf{Y}_3 = {}^C\mathbf{r}_{T3} + {}^C\mathbf{R}_{T3} {}^{T3}\mathbf{r}_{connection3} = {}^C\mathbf{r}_{T3,init} + p_{g0} {}^C\mathbf{v}_{joint0} + p_{g3} {}^C\mathbf{v}_{joint3} + {}^C\mathbf{R}_{T3} {}^{T3}\mathbf{r}_{connection3} \end{array} \right) \quad (89)$$

${}^O\mathbf{R}_C$ and ${}^C\mathbf{R}_{Ti}$ are the rotation transformation matrix from frame E_O to frame E_C , and frame E_C to frame E_{Ti} . The left upper case of each vector indicates the frame that the vector is defined. The vectors without the left upper case are defined in the space-fixed frame E_O . ${}^C\mathbf{r}_{Ti,init}$ represents the initial vector of the trolley, which is constant. \mathbf{Y}_i is the local vector of the connection point on the trolley from the crane frame E_C . To calculate the direction of the constraint force, the Jacobian of the constraint equation is obtained.

$$\dot{\mathbf{c}}_i = \dot{\mathbf{r}}_{hook} - \dot{\mathbf{r}}_{trolley} = (\dot{\mathbf{q}}) - (\dot{\mathbf{r}}_C + \dot{\mathbf{p}}_i) = (\dot{\mathbf{q}}) - (\dot{\mathbf{r}}_C + \boldsymbol{\omega}_C \times \mathbf{p}_i + {}^O\mathbf{R}_C \dot{\mathbf{Y}}_i)$$

$$= (\dot{\mathbf{q}}) - {}^O\mathbf{R}_C \dot{\mathbf{Y}}_i \quad (90)$$

$$\left(\begin{array}{l} \dot{\mathbf{Y}}_i = \dot{p}_{g0} {}^C\mathbf{v}_{joint0} + \dot{p}_{gi} {}^C\mathbf{v}_{jointi} + \cancel{\boldsymbol{\omega}_{Ti}} \times {}^C\mathbf{R}_{Ti} {}^{Ti}\mathbf{r}_{connectioni} \\ = \dot{p}_{g0} {}^C\mathbf{v}_{joint0} + \dot{p}_{gi} {}^C\mathbf{v}_{jointi} \end{array} \right)$$

We assumed that the crane frame does not move or rotate during the simulation. The crane girder can still move on the crane frame. The rotation of the trolley with respect to the crane is also neglected, as the trolleys are connected to crane by slider joints.

The derivatives of the constraint equations are then calculated as follows.

$$\begin{aligned}
\dot{\Phi}_{1,i} &= \mathbf{c}_i^T \dot{\mathbf{c}}_i - p_{ci} \dot{p}_{ci} = 0 \\
&= \mathbf{c}_i^T \{(\dot{\mathbf{q}}) - {}^O \mathbf{R}_C \dot{\mathbf{Y}}_i\} - p_{ci} \dot{p}_{ci} \\
&= \mathbf{c}_i^T (\dot{\mathbf{q}}) - \mathbf{c}_i^T {}^O \mathbf{R}_C (\dot{p}_{g0} {}^C \mathbf{v}_{joint0} + \dot{p}_{gi} {}^C \mathbf{v}_{jointi}) - p_{ci} \dot{p}_{ci} \\
&= \begin{bmatrix} \mathbf{c}_1^T & & \\ & \mathbf{c}_2^T & \\ & & \mathbf{c}_3^T \end{bmatrix} \begin{bmatrix} \dot{\mathbf{q}}_1 \\ \dot{\mathbf{q}}_2 \\ \dot{\mathbf{q}}_3 \end{bmatrix} \\
&\quad - \begin{bmatrix} \mathbf{c}_1^T {}^O \mathbf{R}_C {}^C \mathbf{v}_{joint0} & \mathbf{c}_1^T {}^O \mathbf{R}_C {}^C \mathbf{v}_{joint1} & 0 & p_{c1} & 0 & 0 \\ \mathbf{c}_2^T {}^O \mathbf{R}_C {}^C \mathbf{v}_{joint0} & \mathbf{c}_2^T {}^O \mathbf{R}_C {}^C \mathbf{v}_{joint2} & 0 & 0 & p_{c2} & 0 \\ \mathbf{c}_3^T {}^O \mathbf{R}_C {}^C \mathbf{v}_{joint0} & 0 & \mathbf{c}_3^T {}^O \mathbf{R}_C {}^C \mathbf{v}_{joint3} & 0 & 0 & p_{c3} \end{bmatrix} \begin{bmatrix} \dot{\mathbf{p}}_g \\ \dot{\mathbf{p}}_c \end{bmatrix} \\
&= \mathbf{G}_{1q}(\mathbf{p}, \mathbf{q}) \dot{\mathbf{q}} + \mathbf{G}_{1p}(\mathbf{p}, \mathbf{q}) \dot{\mathbf{p}}
\end{aligned} \tag{91}$$

The Jacobian of the constraint, $\mathbf{G}_{1q}(\mathbf{p}, \mathbf{q})$ and $\mathbf{G}_{1p}(\mathbf{p}, \mathbf{q})$ are then obtained, which are the direction of the constraint forces exerted on the hook and crane.

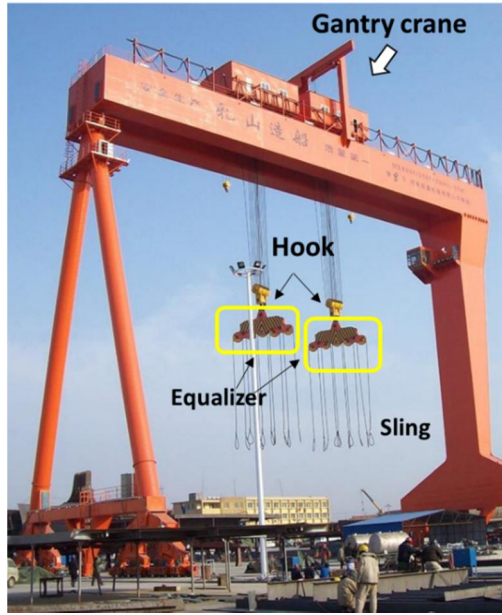


Figure 2-61. The equalizers and slings of the gantry crane.

Meanwhile, the equalizer is equipment that connected to the hook, which consists of equalizing wire rope, fixed and moving pulleys, and slings as shown in Figure 2-61. The equalizer connects the lifting points on the target block with the crane by the wire ropes called slings. The main role of the equalizer is to distribute the tensions to all slings equally. The moving pulleys move up and down to adjust the tension of each sling automatically. The actual mechanism of the equalizer has been modeled using constraint-based wire rope from Ham et al. [60]. We created a constraint equation for the slings of the equalizer as follows, which restrains the sum of the length of the slings equally.

$$g(\mathbf{q}) = \sum_{k=1}^n l_k - l_{total} = 0 \quad (92)$$

Then, the constraint equation of the slings of each equalizer can be formulated as the following equation.

$$\Phi_{2,i}(\mathbf{q}, \mathbf{x}) = \sum_j |\mathbf{c}_{ij}(\mathbf{q}, \mathbf{x})| - l_i \quad (93)$$

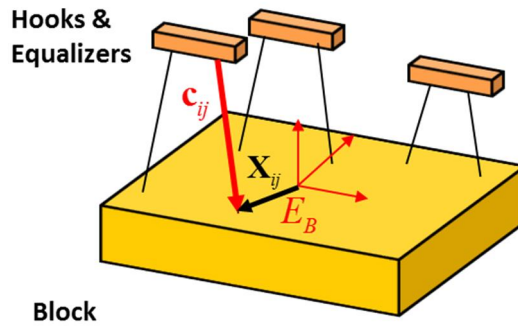


Figure 2-62. Sling vector between hook and block.

i is the index of the hook from 1 to 3, and j is the index of the slings of each equalizer. The wire rope vector and its derivative are obtained in Eq. (94). \mathbf{d}_{ij} is the vector of the lug points of the block from the space-fixed frame, while \mathbf{X}_{ij} is the vector from the local frame of the block.

$$\begin{aligned} \mathbf{c}_{ij} &= \mathbf{r}_{lug} - \mathbf{r}_{hook} = (\mathbf{r}_B + \mathbf{d}_{ij}) - (\mathbf{q}) = (\mathbf{r}_B + {}^o\mathbf{R}_B \mathbf{X}_{ij}) - (\mathbf{q}) \\ \dot{\mathbf{c}}_{ij} &= \dot{\mathbf{r}}_{lug} - \dot{\mathbf{r}}_{hook} = (\dot{\mathbf{r}}_B + \dot{\mathbf{d}}_{ij}) - (\dot{\mathbf{q}}) = (\dot{\mathbf{r}}_B + \boldsymbol{\omega}_B \times \mathbf{d}_{ij}) - (\dot{\mathbf{q}}) \end{aligned} \quad (94)$$

Finally, the Jacobian of the equalizer constraints is calculated.

$$\begin{aligned}
\dot{\Phi}_{2,i} &= \sum_j |\mathbf{c}_{ij}|' = \sum_j \frac{\mathbf{c}_{ij} \cdot \dot{\mathbf{c}}_{ij}}{|\mathbf{c}_{ij}|} \\
&= \sum_j \left(\frac{\mathbf{c}_{ij}}{|\mathbf{c}_{ij}|} \left[((\dot{\mathbf{r}}_B + \boldsymbol{\omega}_B \times \mathbf{d}_{ij}) - (\dot{\mathbf{q}}_{eqi})) \right] \right) \\
&= \sum_j \left(\frac{\mathbf{c}_{ij}}{|\mathbf{c}_{ij}|} \left[((\dot{\mathbf{r}}_B - \mathbf{d}_{ij} \times \boldsymbol{\omega}_B) - (\dot{\mathbf{q}}_{eqi})) \right] \right) \\
&= \sum_j \left(\frac{\mathbf{c}_{ij}}{|\mathbf{c}_{ij}|} \left[((\dot{\mathbf{r}}_B - \tilde{\mathbf{d}}_{ij} \boldsymbol{\omega}_B) - (\dot{\mathbf{q}}_{eqi})) \right] \right) = \sum (\mathbf{k}_{ij}^T \mathbf{v}_B - \mathbf{k}_{ij}^T \tilde{\mathbf{d}}_{ij} \boldsymbol{\omega}_B - \mathbf{k}_{ij}^T \dot{\mathbf{q}}_{eqi}) \quad (95) \\
&= \begin{bmatrix} \sum_j \mathbf{k}_{1j}^T & -\sum_j \mathbf{k}_{1j}^T \tilde{\mathbf{d}}_{1j} \\ \sum_j \mathbf{k}_{2j}^T & -\sum_j \mathbf{k}_{2j}^T \tilde{\mathbf{d}}_{2j} \\ \sum_j \mathbf{k}_{3j}^T & -\sum_j \mathbf{k}_{3j}^T \tilde{\mathbf{d}}_{3j} \end{bmatrix} \begin{bmatrix} \mathbf{v}_B \\ \boldsymbol{\omega}_B \end{bmatrix} - \begin{bmatrix} \sum_j \mathbf{k}_{1j}^T \\ \sum_j \mathbf{k}_{2j}^T \\ \sum_j \mathbf{k}_{3j}^T \end{bmatrix} \begin{bmatrix} \dot{\mathbf{q}}_1 \\ \dot{\mathbf{q}}_2 \\ \dot{\mathbf{q}}_3 \end{bmatrix} \\
&= \mathbf{G}_{2s}(\mathbf{q}, \mathbf{x}) \dot{\mathbf{x}} + \mathbf{G}_{2q}(\mathbf{q}, \mathbf{x}) \dot{\mathbf{q}}
\end{aligned}$$

where,

$$\mathbf{k}_{ij} = \frac{\mathbf{c}_{ij}}{|\mathbf{c}_{ij}|} \quad (96)$$

③ Equations of motion

Finally, the equations of motion of the crane system, hook, and the block is obtained as

$$\begin{aligned}
 \mathbf{M}_p \ddot{\mathbf{p}} &= \mathbf{f}_p(\mathbf{p}, \dot{\mathbf{p}}) + \mathbf{B}^T \mathbf{u} - \mathbf{G}_{1p}^T(\mathbf{p}, \mathbf{q}) \lambda_1 \\
 \mathbf{M}_q \ddot{\mathbf{q}} &= \mathbf{f}_q(\mathbf{q}, \dot{\mathbf{q}}) - \mathbf{G}_{1q}^T(\mathbf{p}, \mathbf{q}) \lambda_1 - \mathbf{G}_{2q}^T(\mathbf{q}, \mathbf{x}) \lambda_2 \\
 \mathbf{M}_b \dot{\mathbf{t}} &= \mathbf{f}_b(\mathbf{x}, \dot{\mathbf{x}}) - \mathbf{G}_{2s}^T(\mathbf{q}, \mathbf{x}) \lambda_2
 \end{aligned} \tag{97}$$

$$\left(\mathbf{t} = \begin{bmatrix} \mathbf{v} \\ \boldsymbol{\omega} \end{bmatrix}, \mathbf{v} = [\dot{r}_x \quad \dot{r}_y \quad \dot{r}_z], \boldsymbol{\omega} = [\omega_x \quad \omega_y \quad \omega_z] \right),$$

where \mathbf{f} is the external force exerted on each body, and λ_i is the magnitude of the constraint force of Φ_i .

(2) Floating crane

The floating crane is composed of a crane barge and two booms, and the block is connected to the booms with four wire ropes. The crane controls the motion of the block through the angle of two booms and the hosting of four wire ropes connected to the boom (Figure 2-63). The booms are connected to the crane barge by hinge joints with the y-axis as the rotation axis.

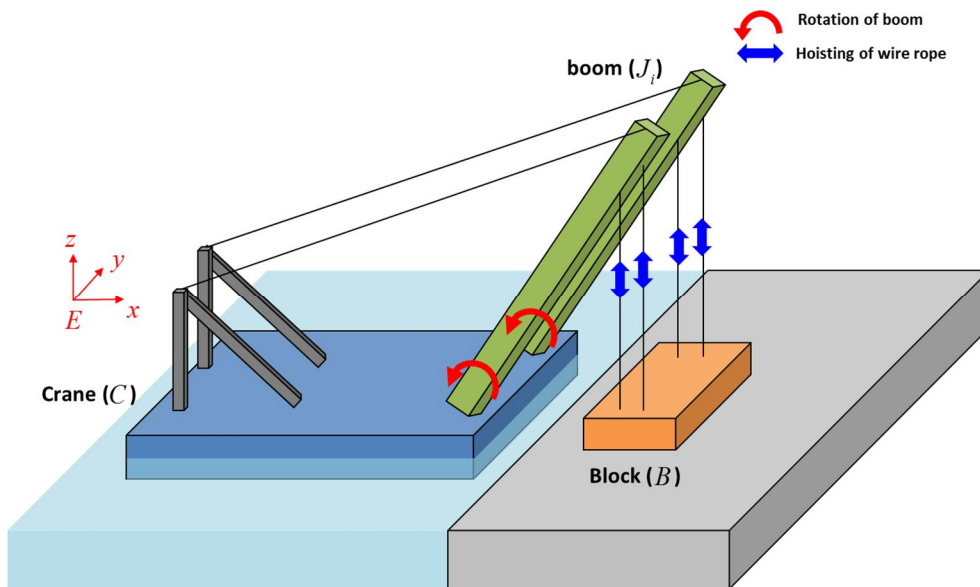


Figure 2-63. Configuration of the floating crane system.

The crane barge is fixed to the quay and the seabed by mooring lines. However, it still has a dynamic motion induced by the wave forces. In this application, we assumed that the floating barge only has heave and pitch motion during the operation, which can then be compensated with the motion of the booms and the wire ropes.

① Redundant coordinates

The floating crane has six control inputs, which are the moment exerted on the hinge joint between the boom and the barge, and the moment exerted on the winch of the wire ropes.

$$\begin{aligned}
\mathbf{u} &= \begin{bmatrix} \mathbf{u}_b \\ \mathbf{u}_c \end{bmatrix} \\
\mathbf{u}_b &= [u_{b1} \quad u_{b2}]^T \\
\mathbf{u}_c &= [u_{c1} \quad u_{c2} \quad u_{c3} \quad u_{c4}]^T
\end{aligned} \tag{98}$$

In the same way as the gantry crane, the crane barge, booms and the block has local frames as shown in Figure 2-64.

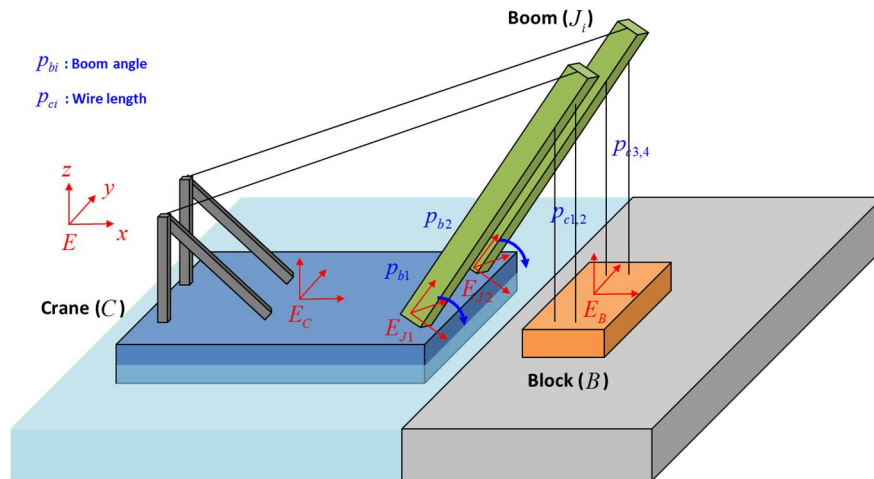


Figure 2-64. Coordinates of the floating crane.

Though the crane system has six control inputs, the number of the coordinates of the floating crane is eight, including the heave and pitch motion of the crane barge. The motion of the crane barge is not directly controllable, and it is a typical underactuated system. The coordinates of the floating crane and the drive system and the mass matrix are defined as follows.

$$\begin{aligned}
\mathbf{p}_{crane} &= [z_{crane} \quad \theta_{crane}]^T, \quad \mathbf{p} = \begin{bmatrix} \mathbf{p}_b \\ \mathbf{p}_c \end{bmatrix} \\
\mathbf{p}_b &= [p_{b1} \quad p_{b2}]^T \\
\mathbf{p}_c &= [p_{c1} \quad p_{c2} \quad p_{c3} \quad p_{c4}]^T
\end{aligned} \tag{99}$$

$$\mathbf{M}_p = \begin{bmatrix} I_{boom1} + (l/2)^2 m_{boom1} & & & & & \\ & I_{boom2} + (l/2)^2 m_{boom2} & & & & \\ & & J_1 / r_1 & & & \\ & & & J_2 / r_2 & & \\ & & & & J_3 / r_3 & \\ & & & & & J_4 / r_4 \end{bmatrix} \tag{100}$$

As the floating crane has six control inputs, the motion of the block with six degrees of freedom is controllable. The block coordinates are defined the same as that of the gantry crane. In this system, we ignored the motion of the hooks and assumed the block is connected to the boom directly with wire ropes.

② Constraints

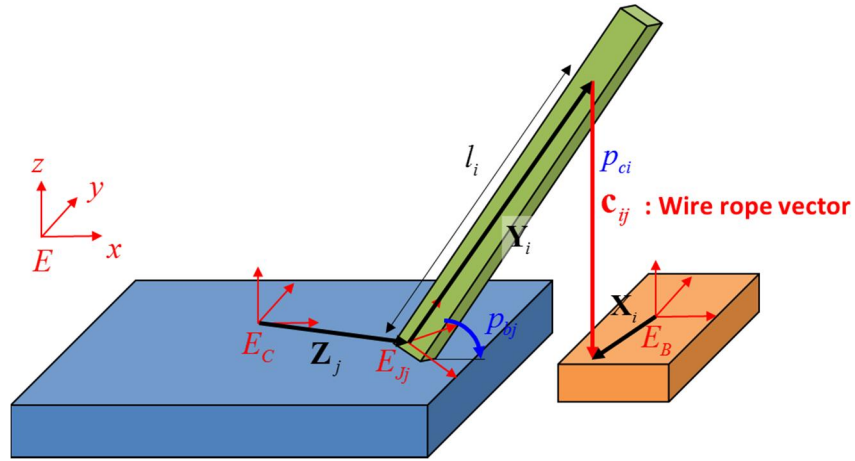


Figure 2-65. Wire rope vector between boom and block.

The wire rope constraint between boom and block is modeled as a constraint to restrain the length of the wire rope same as the distance between the connection point of the boom and the lug of the block. The constraint equation is defined as

$$\Phi_{ij}(\mathbf{p}, \mathbf{x}) = \frac{1}{2} (\mathbf{c}_{ij}^T(\mathbf{p}, \mathbf{x}) \mathbf{c}_{ij}(\mathbf{p}, \mathbf{x}) - p_{ci}^2) \quad (101)$$

where \mathbf{c}_{ij} is the wire rope vector, and i is the index of the wire rope from 1 to 4, and j is the index of the boom, which is 1 or 2. The wire rope vector and its derivatives can be written as follows.

$$\begin{aligned}
\mathbf{c}_{ij} &= \mathbf{r}_{lug} - \mathbf{r}_{boom} \\
&= \left(\mathbf{r}_B + {}^C \mathbf{R}_B \mathbf{X}_i \right) - \left(\mathbf{r}_{boomj} + {}^E \mathbf{R}_{Jj} \mathbf{Y}_i \right) \\
&= \left(\mathbf{r}_B + \mathbf{d}_i \right) - \left(\mathbf{r}_{crane} + {}^E \mathbf{R}_{crane} \mathbf{Z}_j + {}^E \mathbf{R}_{Jj} \mathbf{Y}_i \right) \\
&\quad \left(\mathbf{Y}_{boom_i} = [0, 0, l_i]^T \right)
\end{aligned} \tag{102}$$

$$\begin{aligned}
\dot{\mathbf{c}}_{ij} &= \left(\dot{\mathbf{r}}_B + \boldsymbol{\omega}_B \times \mathbf{d}_i \right) - \left(\dot{\mathbf{r}}_{crane} - \overline{{}^E \mathbf{R}}_{crane} \mathbf{Z}_j \begin{bmatrix} 0 \\ \dot{\theta}_{crane} \\ 0 \end{bmatrix} - \overline{{}^E \mathbf{R}}_{Jj} \mathbf{Y}_i \begin{bmatrix} 0 \\ \dot{p}_{bj} + \dot{\theta}_{crane} \\ 0 \end{bmatrix} \right) \\
&= \left(\dot{\mathbf{r}}_B + \boldsymbol{\omega}_B \times \mathbf{d}_i \right) - \left(\dot{\mathbf{r}}_{crane} - \overline{{}^E \mathbf{R}}_{crane} \mathbf{Z}_j \mathbf{e}_y \dot{\theta}_{crane} - \overline{{}^E \mathbf{R}}_{Jj} \mathbf{Y}_i \mathbf{e}_y \left(\dot{p}_{bj} + \dot{\theta}_{crane} \right) \right)
\end{aligned} \tag{103}$$

\mathbf{Z}_j , \mathbf{Y}_i , and \mathbf{X}_i are the local position vector of the joint of the boom j from the crane, connection point i of the boom, and the lug point i of the block. Finally, the derivative of the constraint is calculated from the equations above.

$$\begin{aligned}
\dot{\Phi}_{ij} &= \mathbf{c}_{ij}^T \dot{\mathbf{c}}_{ij} - p_{ci} \dot{p}_{ci} = 0 \\
&= \mathbf{c}_{ij}^T \left\{ \left(\dot{\mathbf{r}}_B + \boldsymbol{\omega}_B \times \mathbf{d}_i \right) + \left(-\dot{\mathbf{r}}_{crane} + \overline{{}^E \mathbf{R}}_{crane} \mathbf{Z}_j \mathbf{e}_y \dot{\theta}_{crane} + \overline{{}^E \mathbf{R}}_{Jj} \mathbf{Y}_i \mathbf{e}_y \left(\dot{p}_{bj} + \dot{\theta}_{crane} \right) \right) \right\} - p_{ci} \dot{p}_{ci} \\
&= \mathbf{c}_{ij}^T \left(\dot{\mathbf{r}}_B - \tilde{\mathbf{d}}_i \boldsymbol{\omega}_B \right) - \mathbf{c}_{ij}^T \dot{\mathbf{r}}_{crane} + \mathbf{c}_{ij}^T \overline{{}^E \mathbf{R}}_{crane} \mathbf{Z}_j \mathbf{e}_y \dot{\theta}_{crane} + \mathbf{c}_{ij}^T \overline{{}^E \mathbf{R}}_{Jj} \mathbf{Y}_i \mathbf{e}_y \left(\dot{p}_{bj} + \dot{\theta}_{crane} \right) - p_{ci} \dot{p}_{ci} \\
&= \begin{bmatrix} \mathbf{c}_{ij}^T & -\mathbf{c}_{ij}^T \tilde{\mathbf{d}}_i \end{bmatrix} \begin{bmatrix} \dot{\mathbf{r}}_B \\ \boldsymbol{\omega}_B \end{bmatrix} + \begin{bmatrix} -\mathbf{c}_{ij}^T & \mathbf{c}_{ij}^T \overline{{}^E \mathbf{R}}_{crane} \mathbf{Z}_j \mathbf{e}_y + \mathbf{c}_{ij}^T \overline{{}^E \mathbf{R}}_{Jj} \mathbf{Y}_i \mathbf{e}_y \end{bmatrix} \begin{bmatrix} \dot{\mathbf{r}}_{crane} \\ \dot{\theta}_{crane} \end{bmatrix} + \begin{bmatrix} \mathbf{c}_{ij}^T \overline{{}^E \mathbf{R}}_{Jj} \mathbf{Y}_i \mathbf{e}_y & -p_{ci} \end{bmatrix} \\
&= \mathbf{G}_s(\mathbf{p}, \mathbf{x}) \begin{bmatrix} \dot{\mathbf{r}}_B \\ \boldsymbol{\omega}_B \end{bmatrix} + \mathbf{G}_c(\mathbf{p}_{crane}, \mathbf{p}, \mathbf{x}) \begin{bmatrix} \dot{\mathbf{r}}_{crane} \\ \dot{\theta}_{crane} \end{bmatrix} + \mathbf{G}_p(\mathbf{p}_{crane}, \mathbf{p}, \mathbf{x}) \begin{bmatrix} \dot{p}_b \\ \dot{p}_c \end{bmatrix}
\end{aligned} \tag{104}$$

From this equation, the Jacobian of the constraint is obtained for the block, crane barge, and the drive system.

③ Equations of motion

Lastly, the equations of motion of the crane barge, drive system, and the block are obtained as follows.

$$\begin{aligned}
 \tilde{\mathbf{M}}\ddot{\mathbf{p}}_{crane} &= \tilde{\mathbf{f}}(\mathbf{p}_{crane}, \dot{\mathbf{p}}_{crane}) - \tilde{\mathbf{k}} - \mathbf{G}_c^T(\mathbf{p}_{crane}, \mathbf{p}, \mathbf{q})\boldsymbol{\lambda} \\
 \mathbf{M}_p\ddot{\mathbf{p}} &= \mathbf{f}_p(\mathbf{p}, \dot{\mathbf{p}}) + \mathbf{B}^T\mathbf{u} - \mathbf{G}_p^T(\mathbf{p}_{crane}, \mathbf{p}, \mathbf{x})\boldsymbol{\lambda} \\
 \mathbf{M}_b\dot{\mathbf{t}} &= \mathbf{f}_b(\mathbf{x}, \dot{\mathbf{x}}) - \mathbf{G}_s^T(\mathbf{p}, \mathbf{x})\boldsymbol{\lambda}
 \end{aligned} \tag{105}$$

where \mathbf{f} is the external force exerted on each body, and $\boldsymbol{\lambda}$ is the magnitude of the constraint force of Φ . Matrix $\tilde{\mathbf{M}}_{crane}$, $\tilde{\mathbf{f}}_{crane}$, and $\tilde{\mathbf{k}}$ is expressed as follows, where d_{cog} is the x position of the center of gravity of barge, d_{boom} is the distance of the attached point of the booms in the x-direction, and l is the length of the boom.

constraints.

$$\begin{aligned}
\mathbf{M}_p \ddot{\mathbf{p}} &= \mathbf{f}_p(\mathbf{p}, \dot{\mathbf{p}}) + \mathbf{B}^T \mathbf{u} - \mathbf{G}_p^T(\mathbf{p}, \mathbf{x}) \boldsymbol{\lambda} \\
\mathbf{M}_b \dot{\mathbf{t}} &= \mathbf{f}_b(\mathbf{x}, \dot{\mathbf{x}}) - \mathbf{G}_s^T(\mathbf{p}, \mathbf{x}) \boldsymbol{\lambda} \\
\boldsymbol{\Phi}(\mathbf{p}, \mathbf{x}) &= \mathbf{0} \\
\mathbf{x} &= \boldsymbol{\gamma}(t)
\end{aligned} \tag{107}$$

The mechanical system, or plant, is an actual system that performs the control. The control input calculated from the inverse dynamics solver should be applied to the real hardware for the control. However, in this study, the output of the mechanical system is calculated by using the simulation model of the crane system for verification and application. The calculated control forces are given to the mechanical system (simulation model in this study), and the actual output is obtained. The output of the mechanical system is calculated from DELE in Eq. (11). The dynamic equations of the system can be different from that of the inverse dynamics solver, Eq. (107), as the stretching of the wire rope is included in the plant, and the external forces can be applied as in the actual system.

(2) Index reduction method

The important properties of the inverse dynamics can vary depending on the characteristics of the system. In the overactuated or fully actuated system, the output can explicitly be defined by the control inputs. Therefore, the control force can be obtained simply by a purely algebraic equation reversely. In the underactuated system, on the other hand, the output is not determined by the control inputs, and the target output can have motion dynamically. Therefore, the transformation matrix between the control input and output is invertible. The dynamical effects should be taken into account to find the control

inputs in the underactuated system.

In the underactuated system, the final form of the equations in inverse dynamics solver (Eq. (107)) is a DAE (Differential Algebraic Equation) with a high index. An index is a minimum number of differentiations of the DAE system required in order to obtain an ODE (Ordinary Differential Equation). The index of DAE indicates solvability and difficulty of the system, and high index value causes difficulties in the direct numerical integration of the DAE. The index of DAEs for the inverse dynamics of a fully actuated system is three. However, in the underactuated system, the use of servo constraints leads to a high index of DAEs typically ranging from five or even higher [61]. To solve the DAEs, the index reduction method is required, which reduces the high index value of the DAEs to three or lower.

There are various methods for high index DAE problems, such as flatness-based control [62], projection method [63], and minimal extension method [55]. The flatness implies all system state variables and control inputs can be algebraically expressed in terms of desired output and their time derivatives. The flatness-based control provides an analytic solution to track the reference trajectory exactly as long as there are no disturbances. However, it is not possible to derive the flatness-based analytic solution for the complicated underactuated system. The projection method yields an index reduction from five to three, by splitting the dynamics of the system into constrained and unconstrained parts. Nevertheless, it requires high computational cost to find the projection matrices, which are time-dependent. With these disadvantages, Yang [55] suggested index reduction by the minimal extension method to reduce the index of DAE, which introduces new variables, so-called dummy derivatives. The computation time for constructing the projection matrices is not required.

In index reduction by minimal extension method, two dummy variables, which are the derivative and second derivative of the servo constraint is introduced as shown in Eq. (108).

$$\begin{aligned}
\mathbf{M}_p \ddot{\mathbf{p}} &= \mathbf{f}_p(\mathbf{p}, \dot{\mathbf{p}}) + \mathbf{B}^T \mathbf{u} - \mathbf{G}_p^T(\mathbf{p}, \mathbf{x}) \boldsymbol{\lambda} \\
\mathbf{M}_b \dot{\mathbf{t}} &= \mathbf{f}_b(\mathbf{x}, \dot{\mathbf{x}}) - \mathbf{G}_s^T(\mathbf{p}, \mathbf{x}) \boldsymbol{\lambda} \\
\Phi(\mathbf{p}, \mathbf{x}) &= \mathbf{0} \\
\mathbf{x} &= \boldsymbol{\gamma}, \quad \dot{\mathbf{x}} = \dot{\boldsymbol{\gamma}}, \quad \ddot{\mathbf{x}} = \ddot{\boldsymbol{\gamma}}
\end{aligned} \tag{108}$$

As the holonomic constraints only cause an index of three, only the derivatives of the servo constraints are required to reduce the index. Then, with an assumption that \mathbf{M}_p is positive definite, and \mathbf{G}_s have full rank, the equation above is proven to have an index of three. The DAEs in Eq. (108) are in semi-explicit form, which simple backward Euler discretization generally proven to works well for stable integration [64]. Then, the final equation is obtained as follows.

$$\mathbf{F}(\mathbf{X}) = \begin{bmatrix} \mathbf{f}_1 \\ \mathbf{f}_2 \\ \mathbf{f}_3 \\ \mathbf{f}_4 \end{bmatrix} = \begin{bmatrix} \mathbf{p}_{n+1} - \mathbf{p}_n - \Delta t \mathbf{v}_{n+1} \\ \mathbf{M}_1(\mathbf{v}_{n+1} - \mathbf{v}_n) - \Delta t (\mathbf{B} \mathbf{u}_{n+1} - \mathbf{G}_1(\mathbf{p}_{n+1}, \boldsymbol{\gamma}_{n+1}) \boldsymbol{\lambda}_{n+1}) \\ \mathbf{M}_2 \ddot{\boldsymbol{\gamma}}_{n+1} - \mathbf{f}_2 + \mathbf{G}_2(\mathbf{p}_{n+1}, \boldsymbol{\gamma}_{n+1}) \boldsymbol{\lambda}_{n+1} \\ \Phi(\mathbf{p}_{n+1}, \boldsymbol{\gamma}_{n+1}) \end{bmatrix} = \mathbf{0} \tag{109}$$

$$\left(\mathbf{X} = \begin{bmatrix} \mathbf{p}_{n+1} \\ \mathbf{v}_{n+1} \\ \mathbf{u}_{n+1} \\ \boldsymbol{\lambda}_{n+1} \end{bmatrix} \right)$$

The unknowns of Eq. (109) are \mathbf{p}_{n+1} , \mathbf{v}_{n+1} , \mathbf{u}_{n+1} , and $\boldsymbol{\lambda}_{n+1}$. Finally, the equations are solved using the Gauss-Newton method illustrated below. \mathbf{J} is the Jacobian matrix of the equation \mathbf{F} .

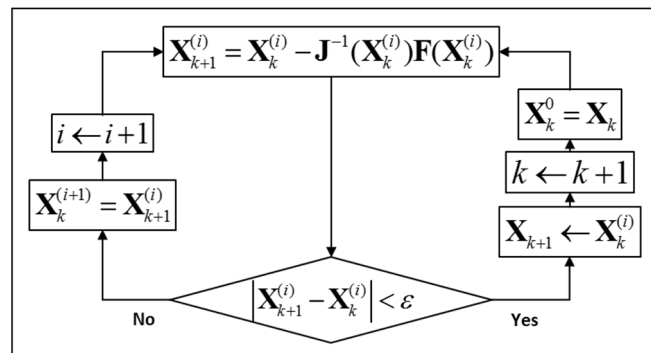


Figure 2-66. Diagram of the Gauss-Newton method.

(3) Feedforward control

In order to obtain a good performance in trajectory tracking, feedforward control is often necessary, which then can be combined with a feedback controller. The feedforward control is to control the output by inverse dynamics solver with the given state value and the predicted external forces. The control forces for the desired output are calculated and applied to the mechanical system.

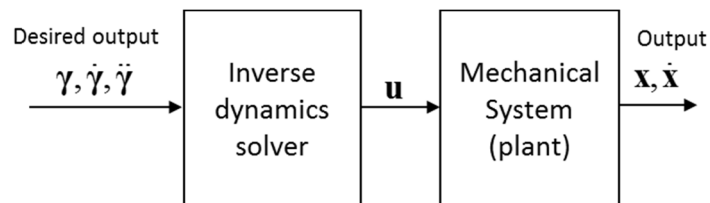


Figure 2-67. Diagram for feedforward control.

Shown in Figure 2-67, the output of the actual system does not affect the inverse dynamics solver in feedforward control. Therefore, the target output tracks the desired trajectory exactly, as long as there are no external disturbances and uncertainties.

(4) Feedback control

The feedforward control method is not appropriate to be applied in the actual system, as there are possible modeling uncertainties and external disturbances. In the applications, the control method should be enhanced by including a feedback control method to provide stable tracking in the actual environment, as shown in Figure 2-68.

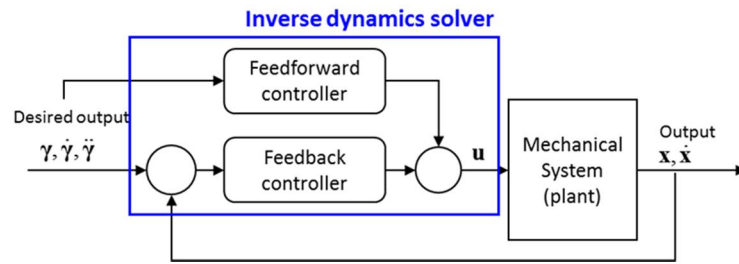


Figure 2-68. Hybrid control merging feedforward and feedback control method.

The servo constraint $\mathbf{s} = \mathbf{x} - \boldsymbol{\gamma} = 0$ represents the error between the desired trajectory and actual output. To consider the output of the mechanical system, the stabilized form of servo constraint [58] is adopted as a PID scheme instead of $\dot{\mathbf{s}} = 0$:

$$\ddot{\mathbf{s}} + \alpha\dot{\mathbf{s}} + \beta\mathbf{s} + \chi \int \mathbf{s} dt = 0 \quad (110)$$

$\alpha, \beta,$ and χ are the PID gain values. Then, the stabilized form of the servo constraint

in the acceleration level is merged to the Eq. (109), and the modified DAEs for inverse dynamics solver combining the feedforward and feedback control law yields the following equation.

$$\mathbf{F}(\mathbf{X}) = \begin{bmatrix} \mathbf{f}_1 \\ \mathbf{f}_2 \\ \mathbf{f}_3 \\ \mathbf{f}_4 \end{bmatrix} = \begin{bmatrix} \mathbf{p}_{n+1} - \mathbf{p}_n - \Delta t \mathbf{v}_{n+1} \\ \mathbf{M}_1 (\mathbf{v}_{n+1} - \mathbf{v}_n) - \Delta t (\mathbf{B} \mathbf{u}_{n+1} - \mathbf{G}_1 (\mathbf{p}_{n+1}, \boldsymbol{\gamma}_{n+1}) \boldsymbol{\lambda}_{n+1}) \\ \mathbf{M}_2 (\ddot{\boldsymbol{\gamma}}_{n+1} - \alpha \dot{\mathbf{s}} - \beta \mathbf{s} - \chi \int \mathbf{s} d) - \mathbf{f}_2 + \mathbf{G}_2 (\mathbf{p}_{n+1}, \boldsymbol{\gamma}_{n+1}) \boldsymbol{\lambda}_{n+1} \\ \boldsymbol{\Phi} (\mathbf{p}_{n+1}, \boldsymbol{\gamma}_{n+1}) \end{bmatrix} = 0 \quad (111)$$

3. Verification

This section provides several verification examples compared with the analytic solutions and commercial software to increase the reliability of the suggested methods.

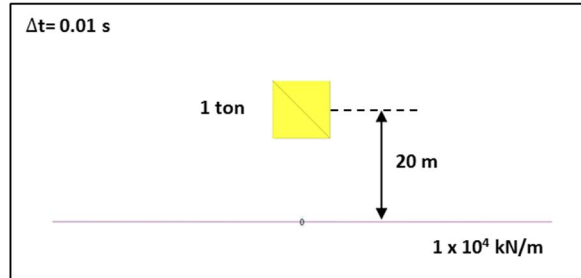
3.1. Verification of the interaction between wire rope and body

To verify the interaction algorithm between the wire rope and the body, we separated the suggested model into contact, friction, and sliding model, and compared with the analytic solutions.

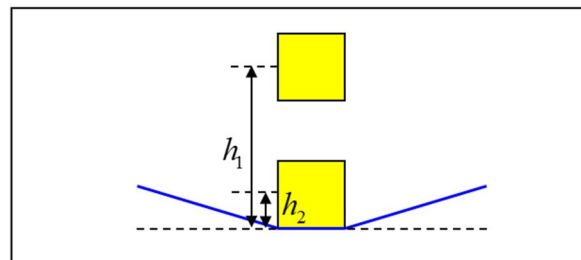
3.1.1. Verification of collision

The collision model includes the collision detection, wire split, force calculation, and wire merge procedure. To verify such procedures, a simple example is presented as illustrated in Figure 3-1. A cube-shaped box with a length of 10 m is dropped from 20 m height from the wire rope. The weight of the box is assumed 1 ton, and the time step is 0.01 s.

Simulation



Analytic solution



$$mgh_1 = mgh_2 + \frac{1}{2}mv_2^2 + \frac{1}{2}kx_2^2$$

Figure 3-1. Simple box-dropping simulation and analytic solution.

For comparison, the analytic solution is calculated from the energy conservation law. The summation of the potential, kinetic, and elastic energy of the block and the wire rope during the simulation should remain the same with the initial potential energy. The damping of the box and the wire rope is neglected. The values of z position and the tension of the wire rope are depicted in Figure 3-2.

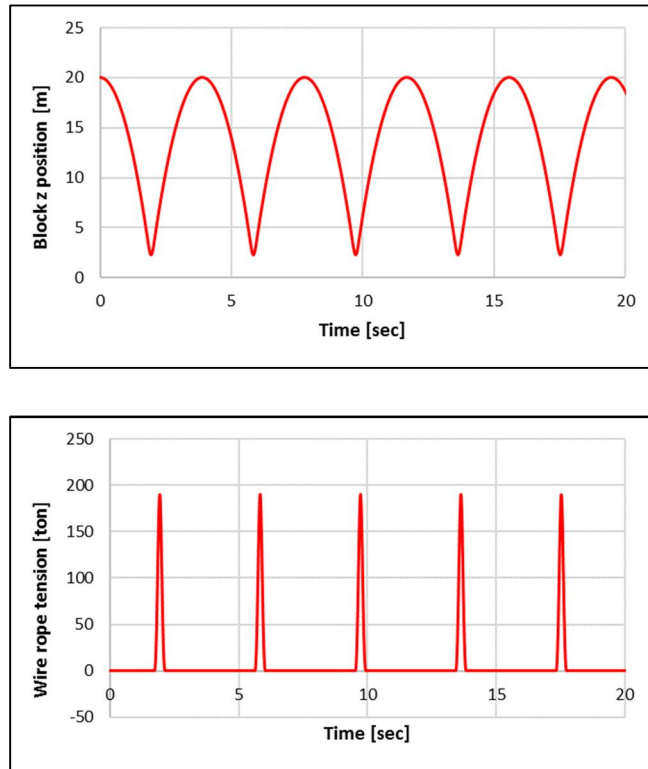


Figure 3-2. Result of the box-dropping simulation.

The box touches the wire rope at 1.75 s, which is the same as the analytic solution. The z-position of the box has regular oscillation and returns to the initial position after the collision as damping is neglected. The tension of the wire rope increases after the collision and reaches a peak at the lowest position of the box. The minimum position of the box and the maximum tension of the wire rope are compared with the analytic solution in Table 3-1.

Table 3-1. Comparison of the box-dropping simulation with the analytic solution.

	Simulation	Analytic solution	Error [%]
Minimum z position of box [m]	2.27	2.28	0.648
Maximum wire rope tension [ton]	189.95	190.11	0.089

The error between the simulation result and the analytic solution is less than 1 % in both values. The error can occur due to the discrete time progression in the simulation with the time step 0.01s.

3.1.2. Verification of sliding

When a wire rope slides on the body, the contact node moves along the edge and split into the other edges. The algorithm to slide to other edges is required only for the numerical simulation as the body is modeled with triangular meshes in the simulation. Therefore, the same model with different mesh compositions should bring the same result. To verify the algorithm that we suggested, we compared a sliding motion of the wire ropes along two identical box models consist of different numbers of mesh (Figure 3-3).

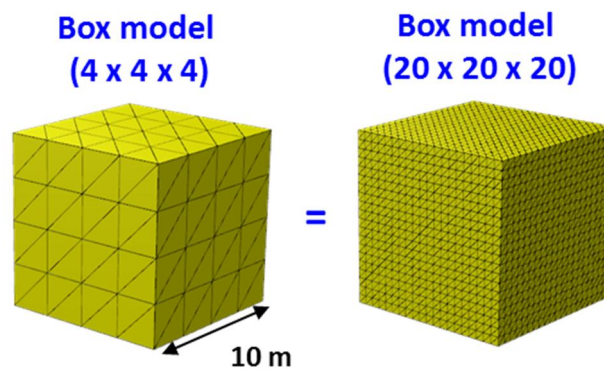


Figure 3-3. The box model with different composition of mesh.

The shape and the weight of the model are exactly the same, and the number of the edges consisting of the box is different. The configuration of the simulation is illustrated in Figure 3-4.

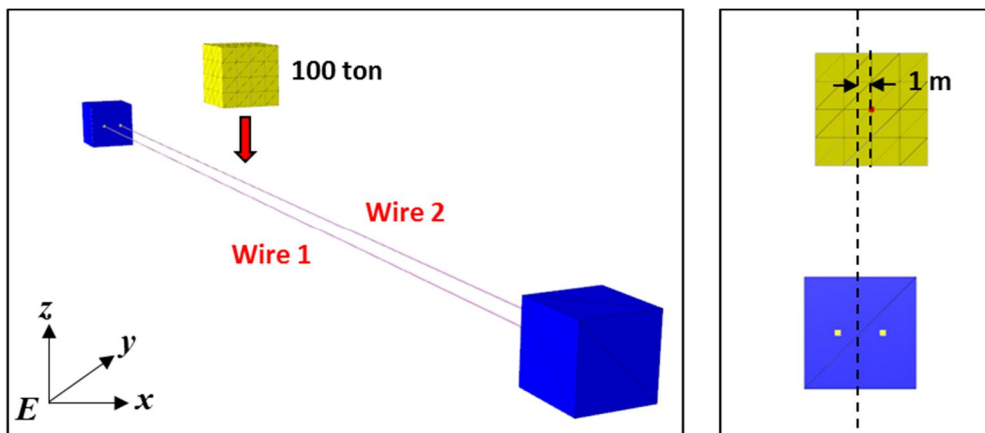


Figure 3-4. Dropping of an unbalanced block on two wire ropes.

The box is located 1 m distant from the centerline on the y-axis. Therefore, as the box dropped on the wire rope, it starts to slide and fall. The sliding of the box and the wire rope is presented in Figure 3-5 and Figure 3-6.

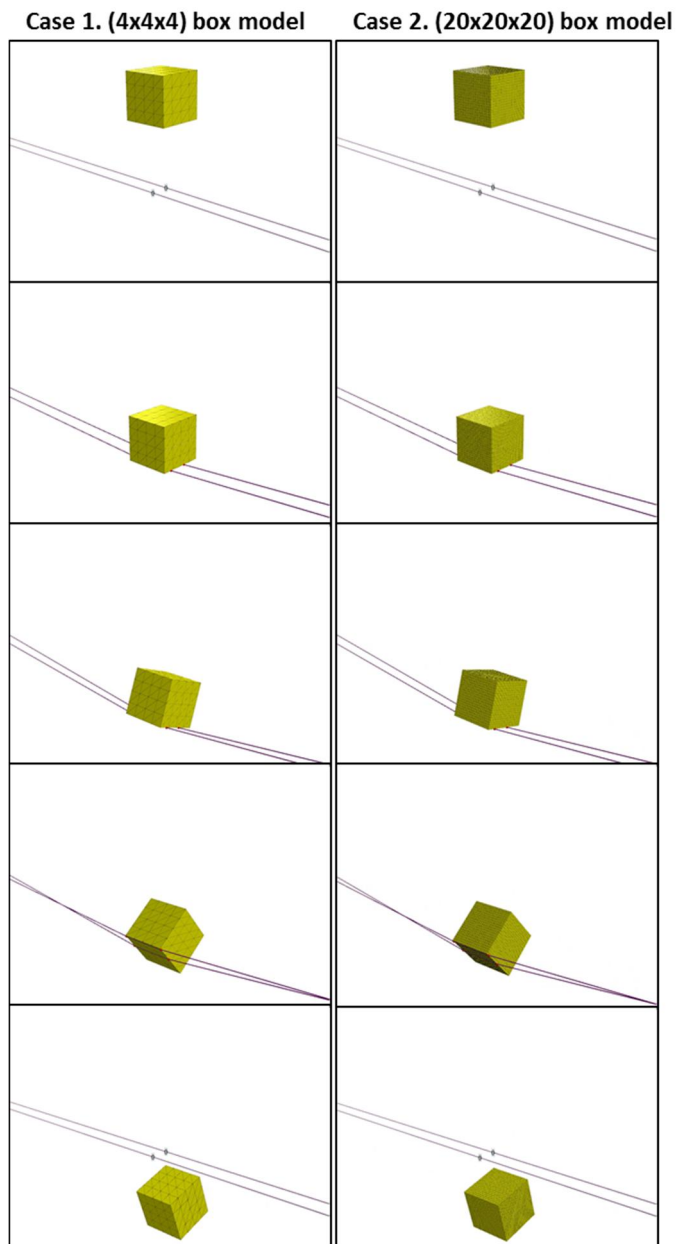


Figure 3-5. Motion of the box sliding on the wire rope.

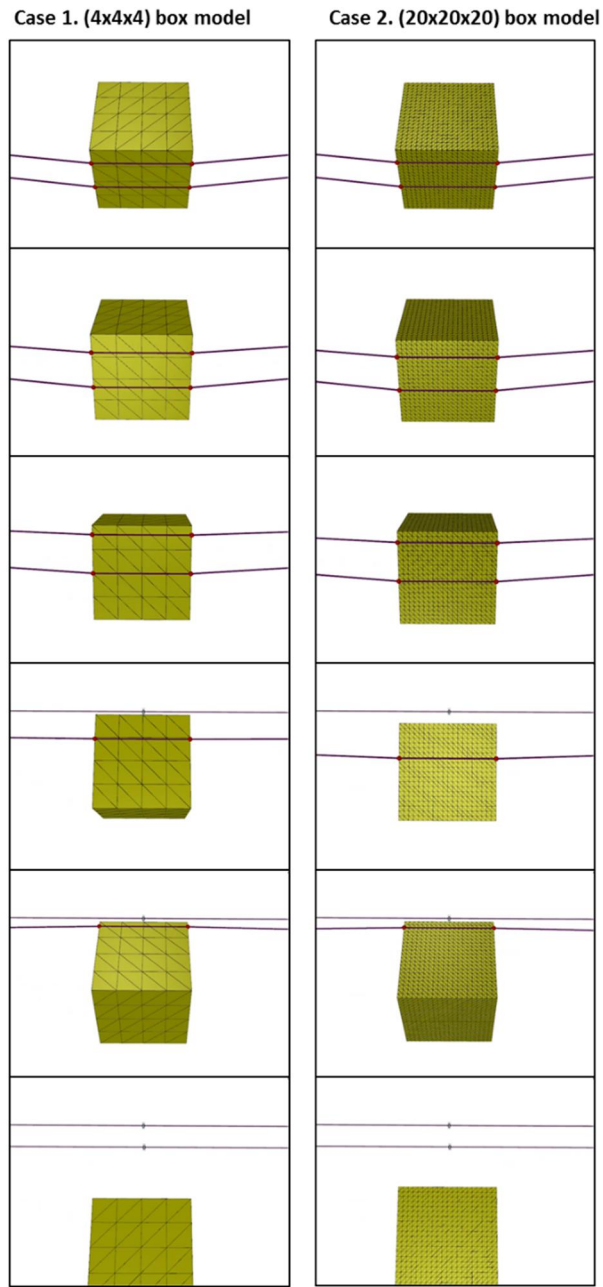


Figure 3-6. Sliding of the wire rope along the edge of the box.

As shown in Figure 3-5, the box apart from the centerline falls to the wire rope and slipped away. Figure 3-6 shows the sliding motion of the wire rope along the edge of the

box. The contact nodes move along the actual edge of the box, regardless of the composition of meshes. The motion of the box and the tension of the wire rope are depicted in the following figures.

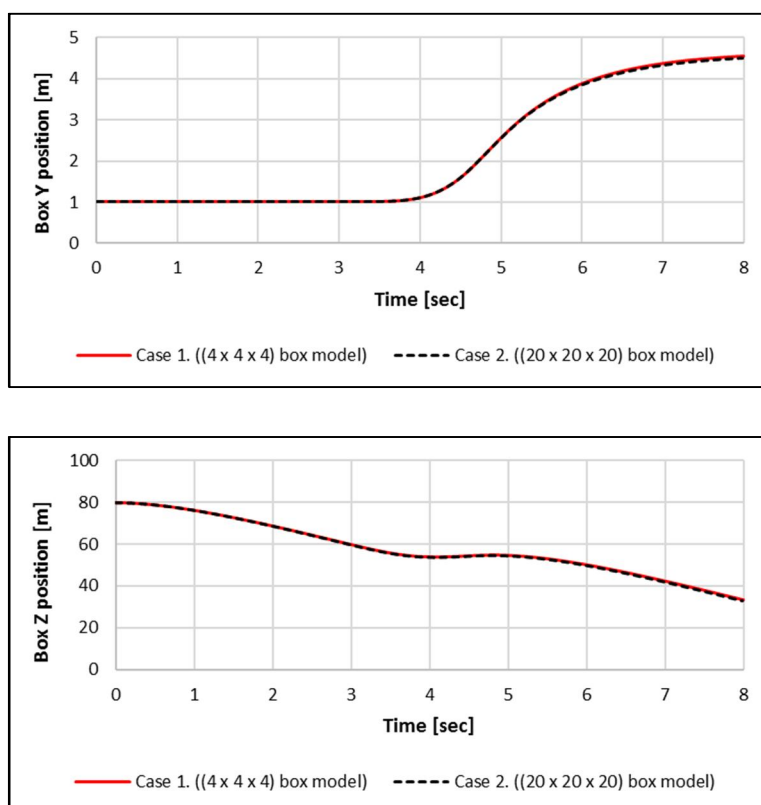


Figure 3-7. Position of the box dropped on two wire ropes.

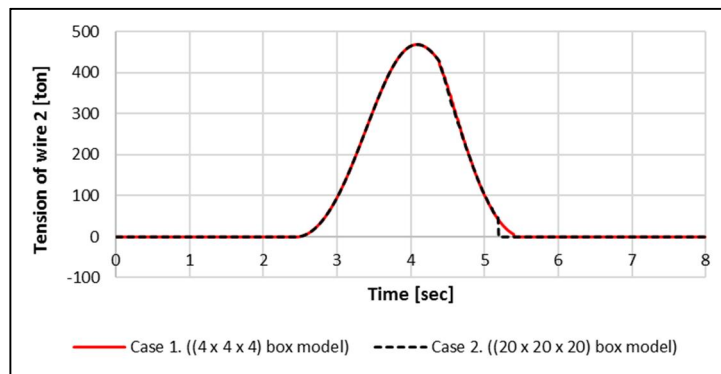
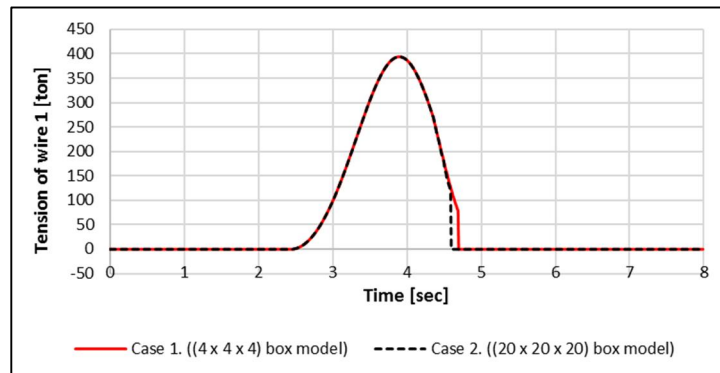


Figure 3-8. Tension of the wire ropes during the dropping of an unbalanced box.

The red solid line is the result of the box model in case 1, and the black dotted line represents the result of case 2. Figure 3-7 and Figure 3-8 show the y, z position of the box, and the tension of two wire ropes. The tension of the wire ropes increases as the box touches the wire rope, and decrease to zero after the block is detached. The motion of the box and the tension of the wire ropes are similar in both cases. The time of detachment of the box and the wire ropes is slightly different due to the sliding motion of the wire rope to other edges. It depends on the mesh composition of the box and the simulation time step. Nevertheless, the composition of the meshes in an identical model hardly affect the sliding motion of the wire ropes and the contact nodes.

3.1.3. Verification of friction

The verification of the friction model is performed in two cases, which only have sliding motion along the edge of the body and the wire rope, respectively. Then, the Coulomb friction model is adopted for comparison.

In case 1, the frictional force exerted on the wire rope during sliding along the edge of the body is verified. The simplified friction model is as shown in Figure 3-9.

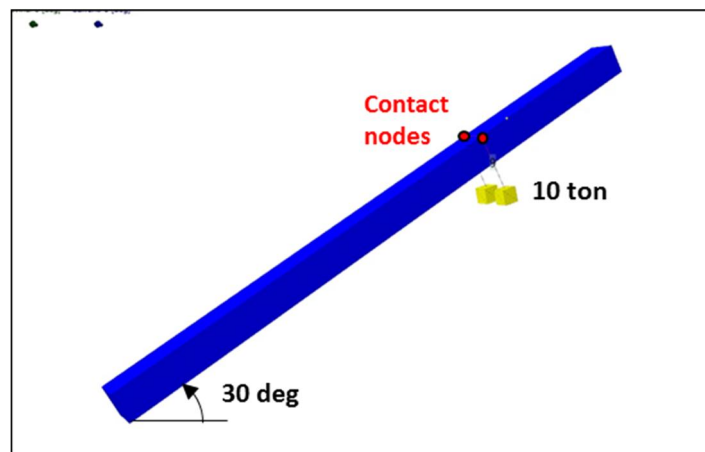


Figure 3-9. Simulation of the wire rope sliding along the edge with friction.

Two boxes are connected with a wire rope, which wraps the long rectangular beam. The weight of the boxes is 10 tons equally so that the sliding along the wire rope does not occur. The inclining angle of the rectangular beam is 30 degrees, and the wire rope connecting the boxes slides down along the long edge of the beam due to its weight. The motion of the wire rope and the boxes are illustrated in Figure 3-10.

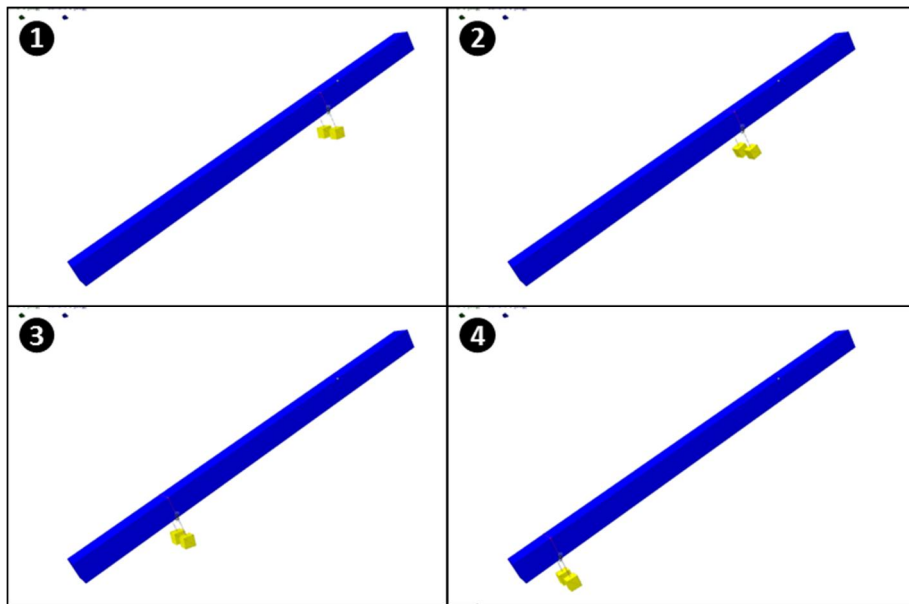


Figure 3-10. Simulation result for validating the friction along the edge.

In the Coulomb friction model, the tangential force exerted on the contact node is $-mg(\sin \theta - \mu \cos \theta)$, and the acceleration decreases linearly by the kinetic friction coefficient μ according to the following equation. The stick friction is reached when $\mu \approx 0.58$.

$$a = (g \sin \theta)(1 - \mu \sec \theta) \quad (112)$$

Case 2 tests the friction along the wire rope. The configuration of the sliding test is illustrated in Figure 3-11.

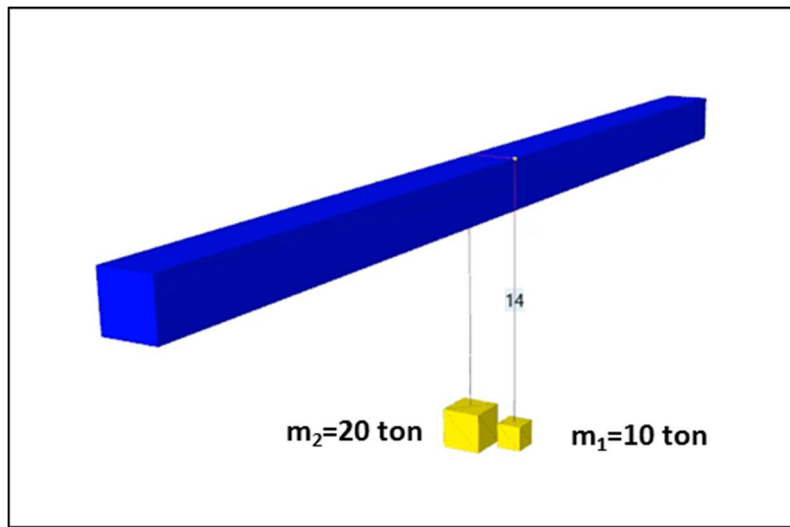


Figure 3-11. Simulation of the body sliding along the wire rope with friction.

Similar to the previous case, two boxes are connected with one wire rope, wrapping the rectangular beam. The weight of the masses is 20 tons and 10 tons, and the contact node slides along the wire rope. The tension of the wire rope without friction is $T = 2m_1m_2/(m_1 + m_2)g$, which yields $T \approx 13.33g$ in this example. If the Coulomb friction force is exerted, the following equation is obtained. The normal of the contact force is $\sqrt{2}T$ due to the 90° turn at the edge.

$$\frac{T - m_1g - \sqrt{2}T\mu}{m_1g} = \frac{m_2g - T - \sqrt{2}T\mu}{m_2g}, \quad (113)$$

where m_1 and m_2 are the weight of the boxes, and μ is the friction coefficient. The wire rope stops sliding and reaches the stick friction when $\mu \approx 0.24$. Both sides of Eq. (113) are the magnitude of the vertical acceleration of the boxes. The acceleration with no

friction is 3.3 m/s^2 . The motion of the boxes is presented in Figure 3-12.

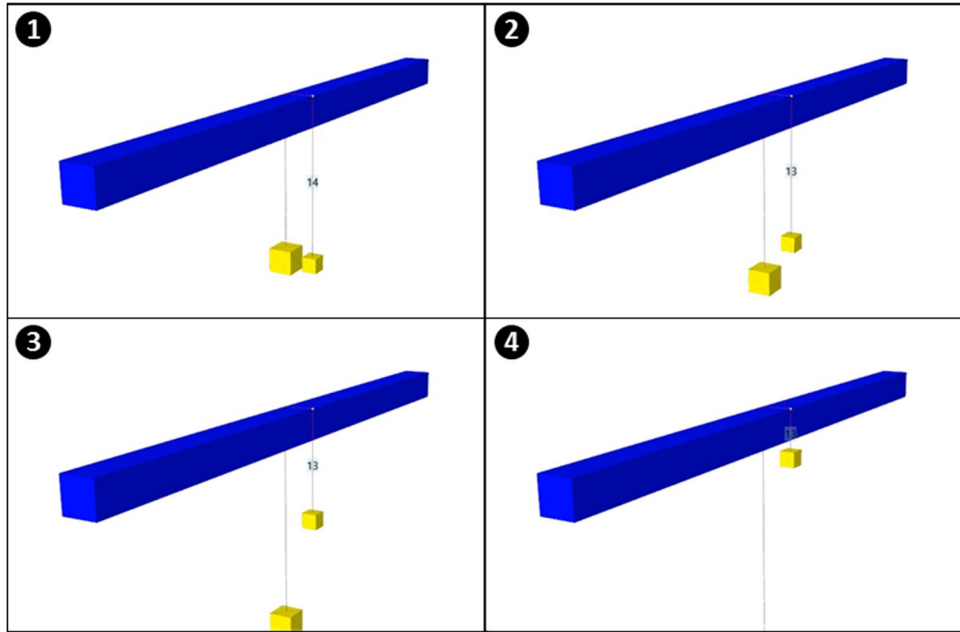


Figure 3-12. Simulation result for validating the friction along the wire rope.

In both cases, the accelerations of the boxes for different friction coefficients are calculated and compared with the result of the Coulomb friction model. In the Coulomb friction model, the friction force is proportional to the friction coefficient, and the acceleration decreases linearly as the friction coefficient increases. The results are depicted in Figure 3-13.

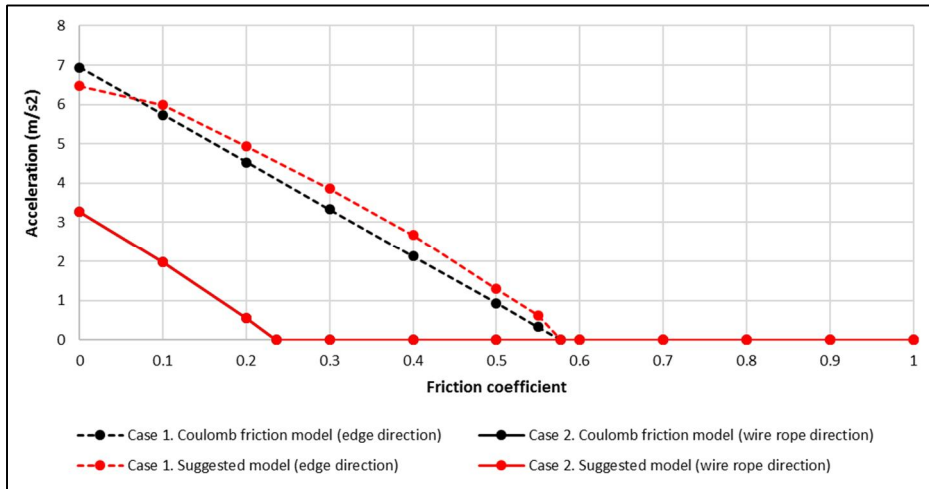


Figure 3-13. Acceleration of the boxes with different friction coefficients.

The red line represents the result of the suggested method, and the black line is that of the Coulomb friction model. In case 2, depicted with a solid line, the result of the suggested friction model along the wire rope is identical with the Coulomb friction model. On the other hand, the friction model along the edge in case 1 shows the difference from the Coulomb friction model. This is most likely because of the assumption about the motion along the edge introduced in section 2.3.3(2). As the wire rope is modeled as a constraint, instead of a flexible body with mass and inertia, the dynamic motion of the wire rope itself is difficult to obtain. The sliding motion of the wire rope and the effect of the kinetic friction force is therefore approximated using Eq. (70).

3.2. Verification of the mooring line model and interaction with the seabed

In this section, the verification of the mooring line is performed by the convergence test and the comparison with the analytic solution and the commercial software.

3.2.1. Convergence test

To determine the number of the beam elements consisting of the mooring line, the convergence test is performed. With a different number of elements, the tension of the mooring line at the fairlead and the length of the mooring line on the seabed are analyzed. The properties of the mooring line are presented in Table 3-2. Both ends of the mooring line are fixed, and the vertical and horizontal distance between them is 100 m and 26 m.

Table 3-2. Properties of the mooring line for the convergence test.

Property	Value
Length	111 m
Weight per unit length	203.9 kg/m
Axial stiffness	61,560 kN
Number of elements	10 ~ 100

The result is shown in Figure 3-14. The length of the seabed is almost the same with a different number of elements. However, the tension at the end starts to converge, as the number of the elements is more than 60.

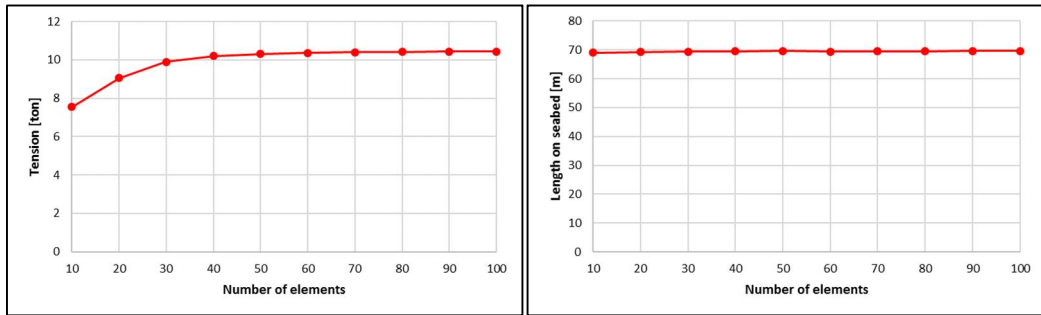


Figure 3-14. Tension and the length on the seabed of the mooring line from the convergence test.

3.2.2. Comparison with the analytic solution

To verify the accuracy of the suggested model, the analytic solution is used. The analytic solution derived in Eq. (48) calculates the profile of the catenary mooring line due to its weight. As the elasticity of the mooring line is not considered in an analytic solution, the unstretchable mooring line is used for the comparison. The properties of the mooring line in Table 3-3 are adopted from Kim et al. [65]. The angle of the slope between two ends is selected as 0, 15, 30, and 45 deg, respectively, for the comparison.

Table 3-3. Properties of the mooring line for the comparison with the analytic solution.

Property	Value
Distance between supports	1,000 m
Total unstretched length	1,026 m
Gravity per unit length	2,000 N/m
Total gravity (W)	2,052,000 N
Slope angle	0, 15, 30, 45 degree
Non-dimensional axial stiffness (EA/W)	1 ~ 300

Figure 3-15 shows the comparison result.

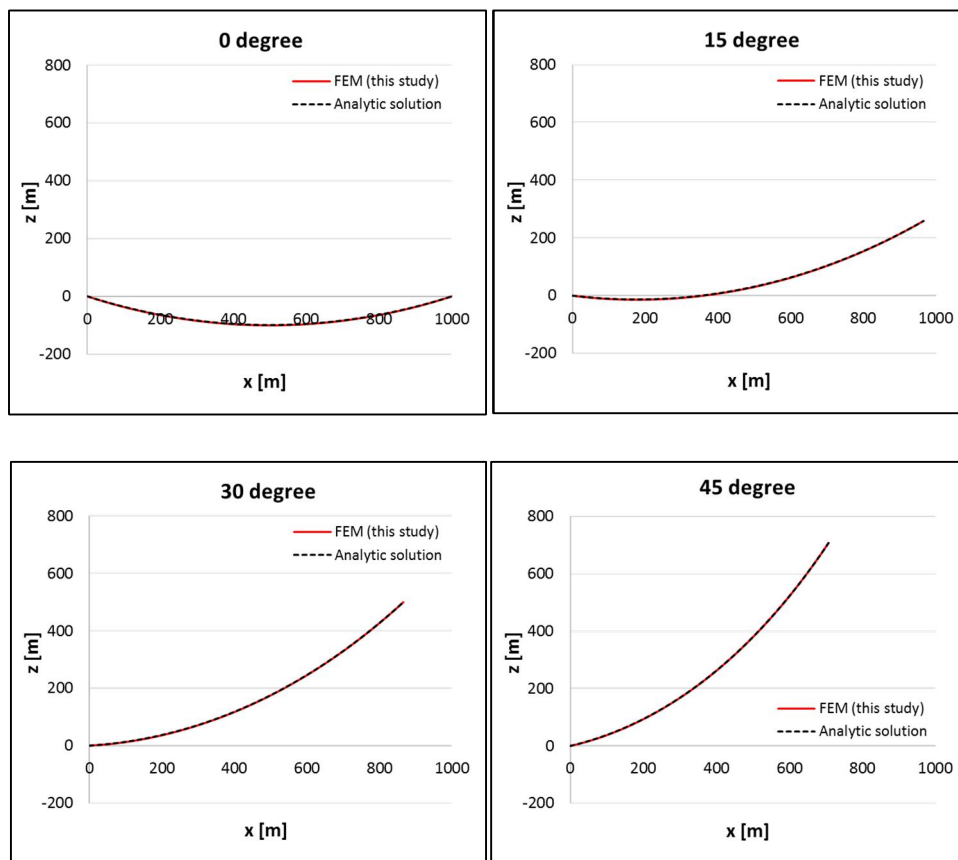


Figure 3-15. Profile of the mooring line compared with the analytic solution.

As shown in Figure 3-15, the profile of the mooring line is the same as the analytic solution at different slope angles. If the non-dimensional axial stiffness of the mooring line is given from 1 to 300, the profile of the mooring line is changed, as shown in Figure 3-16. As the axial stiffness gets smaller, the deflection becomes bigger.

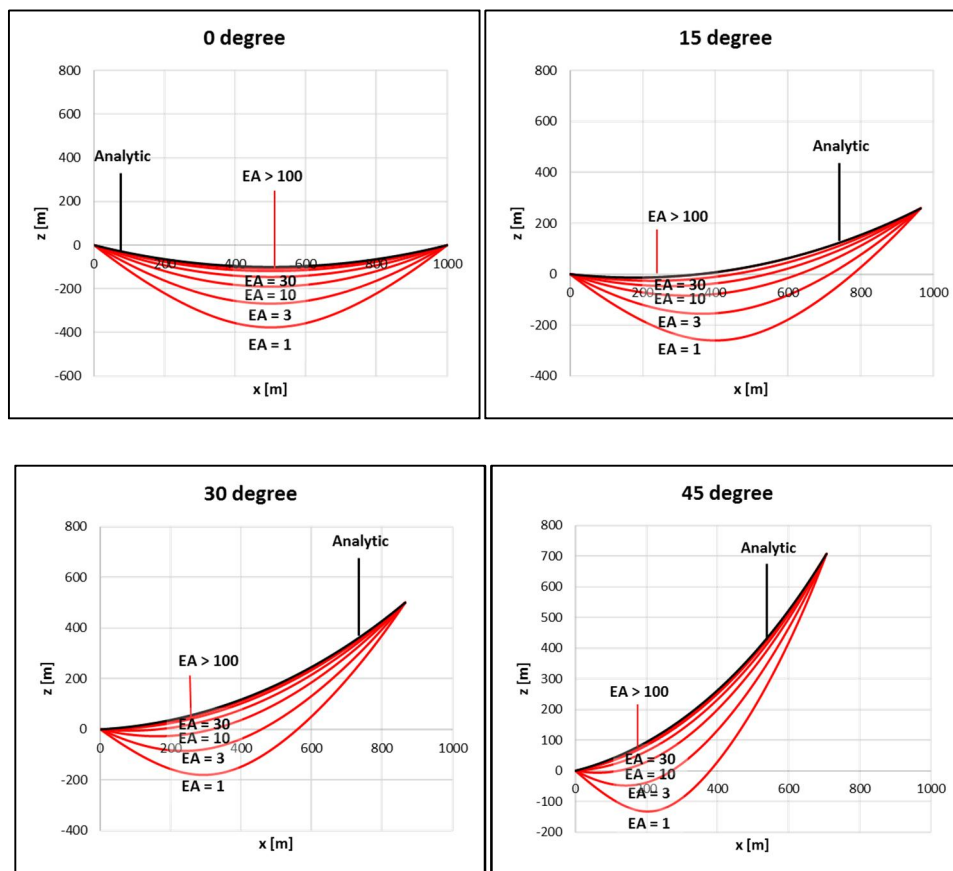


Figure 3-16. Profile of the mooring line with different axial stiffness.

3.2.3. Verification of static analysis

Through the comparison with the analytic solution, the profile of the mooring line due to its weight is verified. However, in actual applications, the axial stiffness of the mooring line cannot be neglected. Moreover, the interaction with the seabed should be considered to verify the tension and the profile of the mooring line. Therefore, the results from the commercial software, OrcaFlex, is adopted for the verification. OrcaFlex has widely used the program in the marine engineering field, especially for mooring analysis. With this program, the results of the static analysis including the length of the seabed, tension at the

fairlead, and the embedded depth of the mooring line, are compared. Fig. 21 below shows the configuration of the test cases.

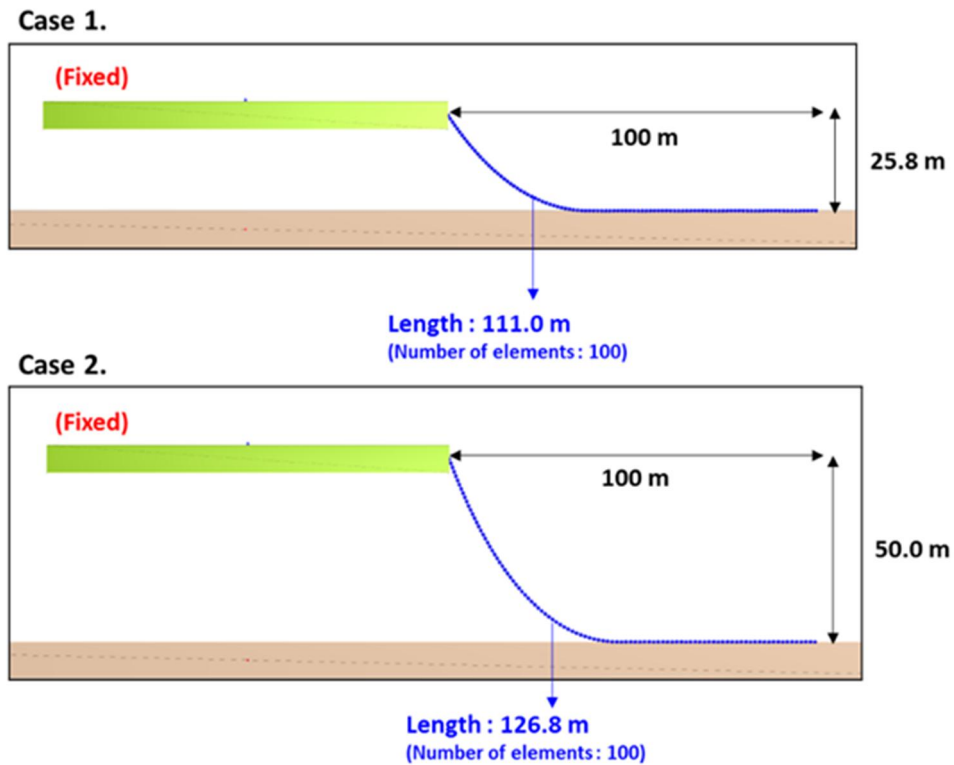


Figure 3-17. Simulation cases for the verification of static analysis with OrcaFlex.

The water depth and the length of the mooring line are selected as 25.8 m and 111.0 m, and 50.0 m and 126.8 m for each case. The number of elements is assumed to be 100 in both models. With the same input data, including the total length of the mooring line, the other values are obtained. The axial stiffness of the mooring line is set to be 61,560 kN. As presented in Table 3-4, the results are almost the same, with the error below 1 %.

Table 3-4. Result of the static analysis compared with OrcaFlex.

Property	Case 1			Case 2		
	This study	OrcaFlex	Error (%)	This study	OrcaFlex	Error (%)
Total length (input) [m]	111.0	111.0	-	126.8	126.8	-
Length on the seabed [m]	69.72	69.22	0.72	59.41	59.52	0.19
Embedded depth [m]	0.415	0.418	0.72	0.419	0.418	0.24
Tension at the fairlead [ton]	10.35	10.26	0.87	15.20	15.10	0.66

3.2.4. Verification of dynamic analysis

For the verification with the analytic solution and the static analysis compared with OrcaFlex, the system is assumed to be in a static equilibrium state. In case that the force exerted so slowly, the inertia and damping force can be neglected as in static analysis. However, for the applications, the behavior of the mooring line that changes with time should be analyzed as the floating object can have dynamic motion. Thus, the dynamic analysis was performed using the suggested model, and the result is compared with the OrcaFlex. The configuration of the test case is illustrated in Figure 3-18.

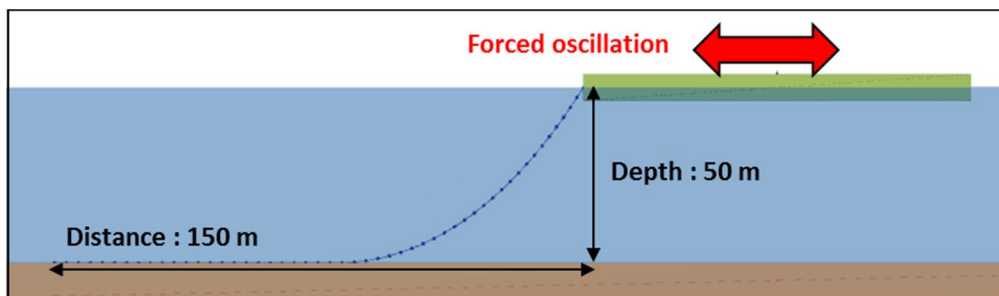


Figure 3-18. Test case for the verification of the dynamic analysis.

We assume a mooring line connected to a floating barge and the seabed at two ends. To verify the dynamic effect of the suggested mooring line, the forced oscillation is given

to the floating barge with certain periods and amplitudes. Then, the tension of the mooring line at the fairlead is investigated and compared with the result of the same model in OrcaFlex. The properties of the floating barge and the mooring line is as summarized in Table 3-5.

Table 3-5. Properties of the barge and the mooring line for dynamic analysis.

	Property	Value
Barge	Length	110 m
	Breadth	46 m
	Depth	7.5 m
	Weight	19,449 ton
Mooring line	Weight per length	203.9 kg/m
	Axial stiffness	61,560 kN
	Total unstretched length	170 m

Two cases are simulated with different oscillation periods. In case 1, the barge oscillates with an amplitude of 5 m and a period of 15.2 sec. In case 2, the period is changed to 7.6 sec. The result of both cases is depicted in Figure 3-19.

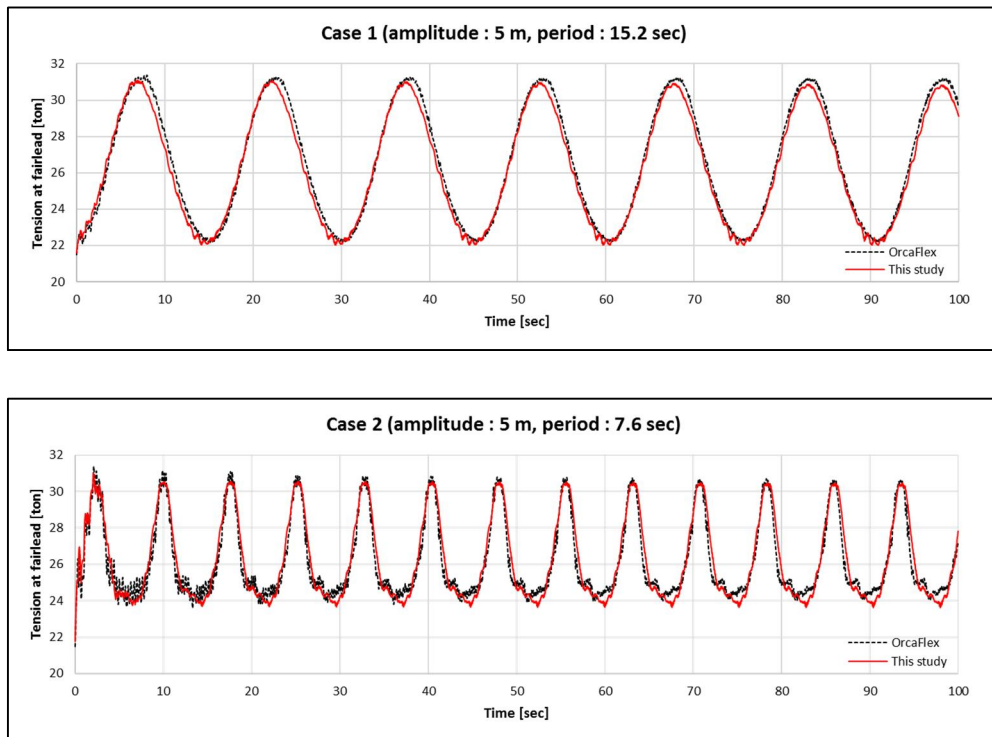


Figure 3-19. Result of the dynamic analysis compared with OrcaFlex.

Due to the oscillation of the barge, the tension of the mooring line changes. In case 1, the tension of the mooring line has a similar tendency with the motion of the barge, as the speed of the mooring line is small. In case 2, the dynamic effect of the mooring line is clearly featured as the period reduced to half. In both cases, the tension of the mooring line at the fairlead induced by the dynamic motion of the barge is identical with the result of OrcaFlex.

3.3. Verification of the inverse dynamics of the underactuated system

In the feedforward control, the inverse dynamics solver calculates the control inputs that force the target to follow the desired trajectory exactly as long as there are no external disturbances. For the verification, the feedforward control is conducted with the inverse dynamics solver for the gantry crane formulated in this study. Then, the obtained control inputs are given as the external forces to the mechanical system using DELE.

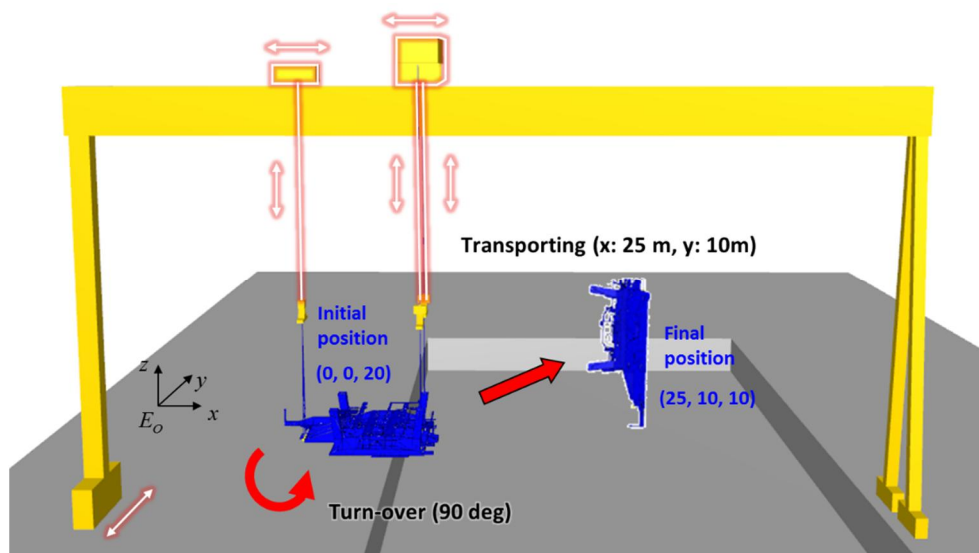


Figure 3-20. Configuration of the control of the block using gantry crane.

Figure 3-20 presents the configuration of the gantry crane and the block, and the desired trajectory that block has to follow. The transporting and turnover of the block are conducted simultaneously using two trolleys and three wire ropes connected to the hooks. The external forces are ignored in this case to verify the feedforward control method. The

desired trajectory and the actual motion of the block are shown in Figure 3-21.

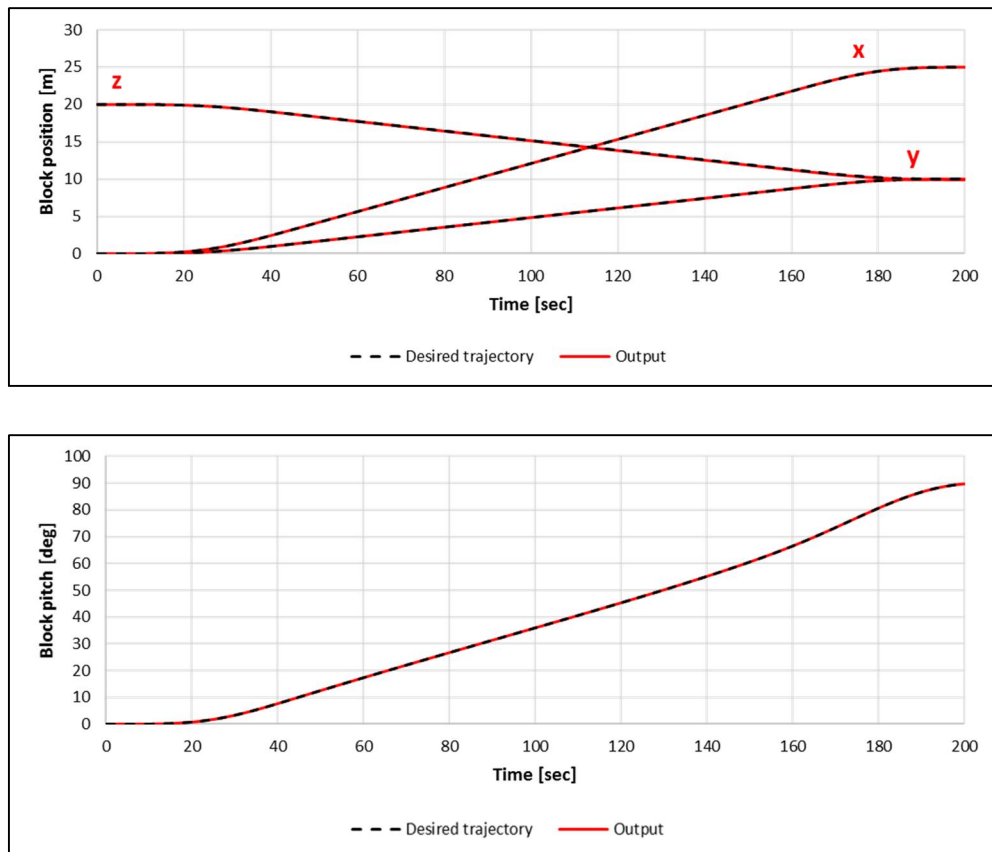


Figure 3-21. The desired and actual trajectory of the block with feedforward control.

The desired trajectory of the block is presented with dotted lines, and the actual output calculated from the mechanical plant is depicted with red solid lines. The result shows that the block tracks the target trajectory exactly. The control inputs are properly calculated in an inverse dynamics solver.

4. Applications

In this section, the suggested simulation models and control methods are applied to the block erection operations.

4.1. Block turnover using floating crane and crawler cranes

The block turnover operations using the floating crane and crawler cranes are simulated based on the multibody system dynamics, including the proposed interaction algorithm between the body and the wire rope. The configuration of the block turnover simulation is as shown in Figure 4-1.

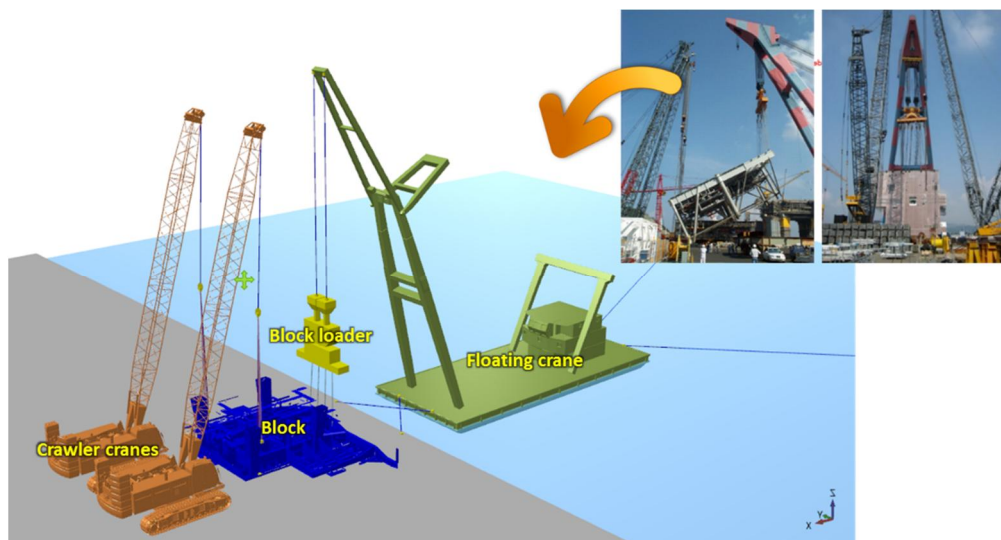


Figure 4-1. Configuration of the block turnover operation using floating crane and crawler cranes.

The floating crane and two crawler cranes lift the block on the quay together with the wire ropes attached to both ends of the block. The floating crane has one block loader

with four slings, and each crawler crane holds the block with three slings. The floating crane is moored to the quay and the seabed, and the crawler cranes are fixed to the ground. The mooring lines are modeled with massless springs. The properties of the floating barge are as summarized in Table 4-1.

Table 4-1. Properties of the floating crane in block turnover operation.

Property		Value
Barge	Length	59 m
	Breadth	22 m
	Depth	4.5 m
	Weight	3,805 ton

The principal dimensions of the block are shown in Figure 4-2. The block data was extracted from the ship CAD data, and converted into triangular mesh data. As shown, the whole block consists of a number of triangular meshes. Its weight is 348 ton, and the size is 27 m in length, 34 m in breadth, and 9 m in depth.

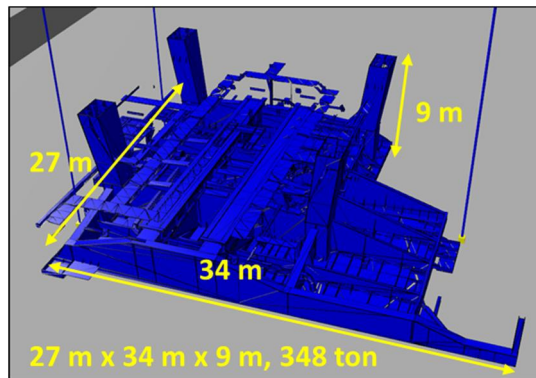


Figure 4-2. Principal dimensions of the block.

The turnover operation is composed of three phases as shown in Figure 4-3. Both

cranes hoist the wire rope up and down to rotate the block to the end position.

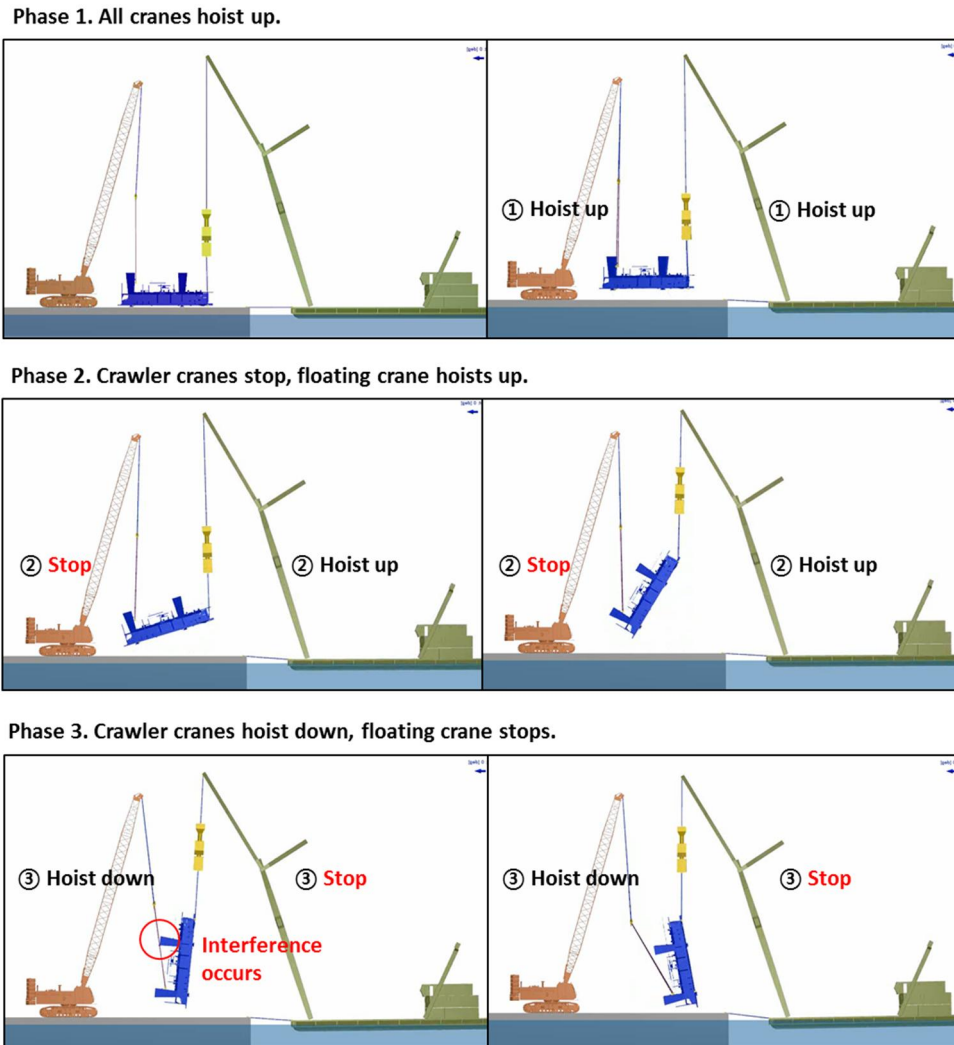


Figure 4-3. Three phases of the block turnover operation.

In phase 1, all cranes hoist up the wire rope connected to the hooks to lift the block. After lifting the block to a certain height, the crawler cranes stop hoisting, and the floating crane hoists up to rotate the block. Then, in phase 3, the crawler cranes slowly

hoist down the wire ropes until the loads become zero, while the floating crane stops hoisting. The interferences between the slings of the crawler cranes and the block occur in this phase. Finally, the floating crane holds the block rotated with 90 degrees. The actual operation has more procedures to turn over the block with 180 degrees, but only three phases stated above are considered in this simulation. The simulation cases are performed with different wave conditions, as presented in Table 4-2.

Table 4-2. Test cases for the block turnover operation

Case	Wave condition		
	Heading angle [degree]	Wave period [sec]	Wave height [m]
1	90	8	1.0
2		10	
3		12	
4		10	0.5
5			2.0

The test cases are selected by different wave period and height. From cases 1 to 3, the interferences between the block and the wire ropes and responses according to wave periods are compared. Then, the results according to the wave height are checked from cases 2, 4, and 5. The motion of the block and the wire ropes during the operation in case 2 are presented in Figure 4-4.

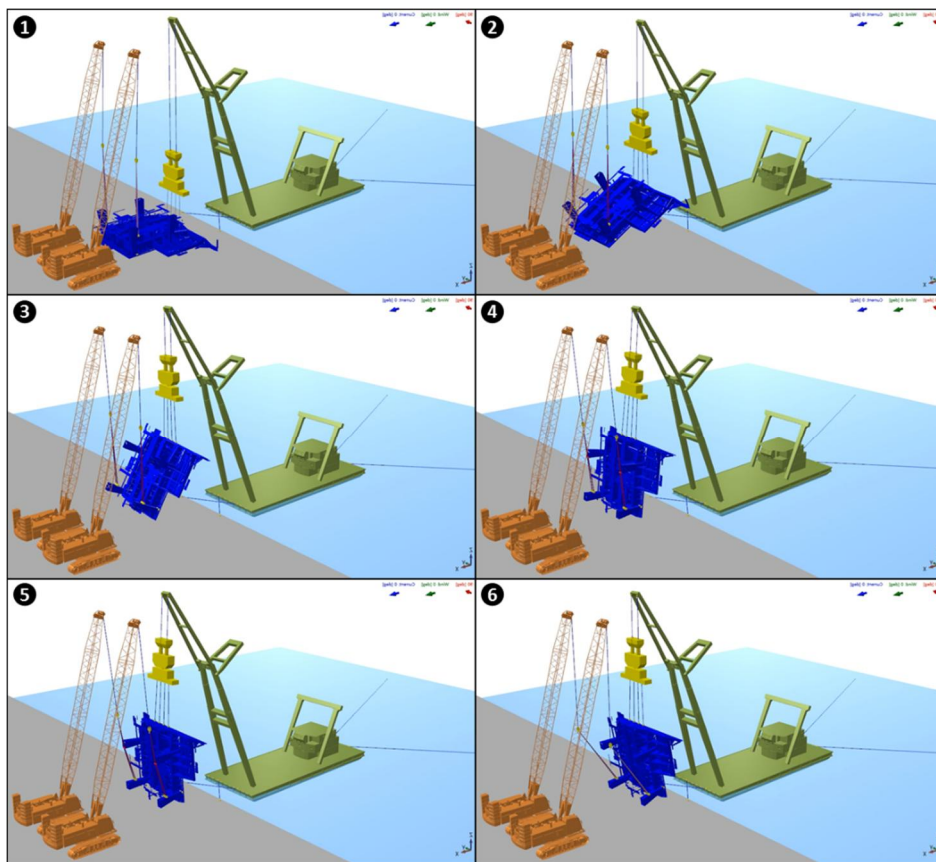


Figure 4-4. Simulation result of case 2 in block turnover operation.

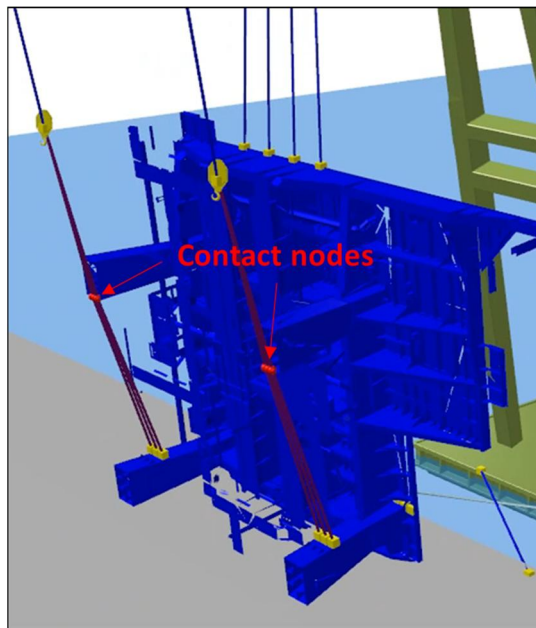


Figure 4-5. Interferences between the block and the wire ropes.

The interferences between the block and the wire ropes occur during phase 3 in every case. As shown in Figure 4-5, six contact nodes are created, one for each sling of the crawler cranes. The contact nodes are inserted into the wire rope, and the contact forces are calculated during the simulation. In case 5, which has maximum wave height, the sliding of the contact points occurs due to the motion of the block induced by a wave as presented in Figure 4-6.

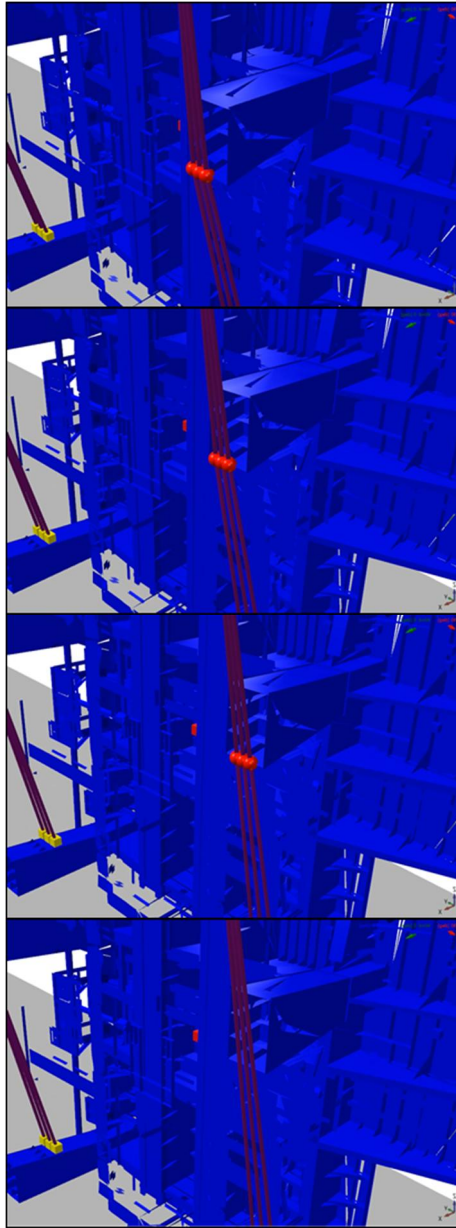


Figure 4-6. Sliding of the contact nodes in case 5.

The contact forces exerted to the block during the simulation are calculated and depicted in Figure 4-7 and Figure 4-8. The contact forces exerted on six contact nodes are separately presented.

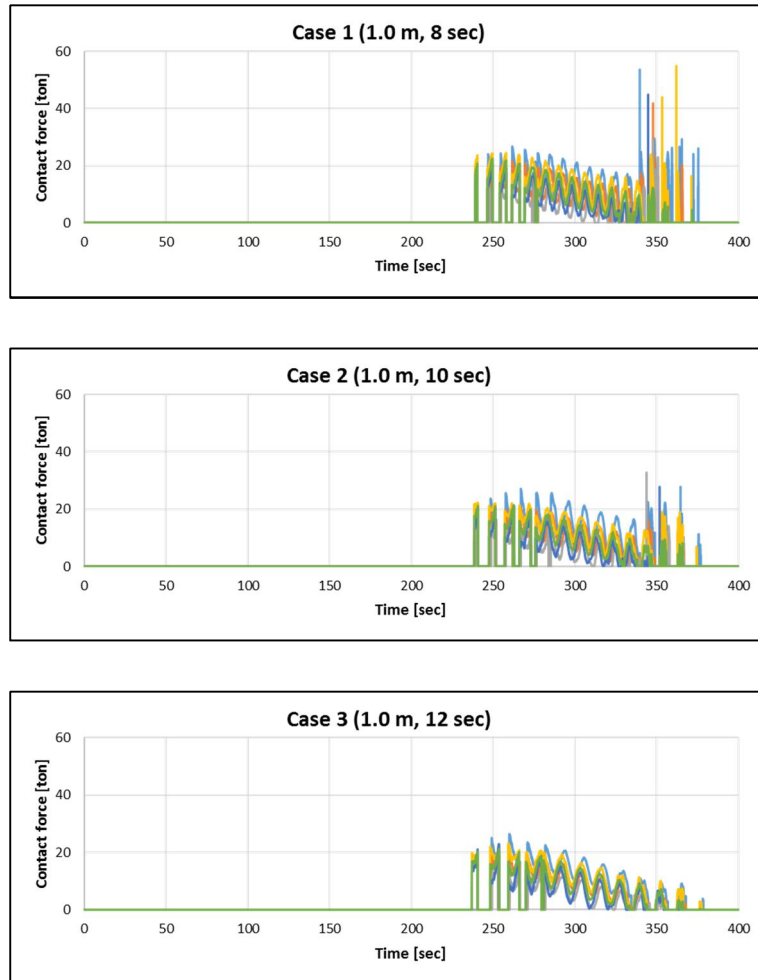


Figure 4-7. Contact forces exerted on the contact nodes in cases 1 to 3.

As the interferences between the block and the wire rope occur, the contact forces are generated. Then, the contact forces become zero as the wire ropes are detached from the body. Case 1, 2, and 3 have different wave periods, which leads to different motion of the floating crane. Shown in Figure 4-7, the time that contact occurs and the contact forces are similar at the early stage, as the wave height is the same. However, the contact forces

suddenly increase in cases 1 and 2 when the crawler cranes hoist down the wire rope. The oscillation of the floating crane becomes large due to the change of the block load, and the impact is exerted between the block and the wire rope. As the attachment and detachment of the wire rope are repeated, the sudden increase of the contact force occurs. The maximum contact force exerted on the block is 55 tons, 33 tons, and 27 tons respectively. The maximum value of the contact force increases as the wave period decreases due to resonance.

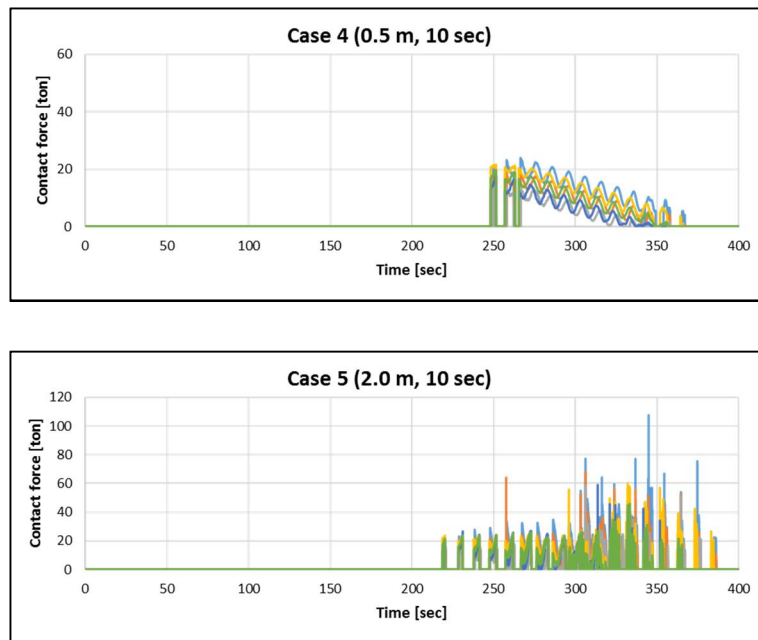


Figure 4-8. Contact forces exerted on the contact nodes in cases 4 and 5.

The contact forces under the different wave height are obtained in cases 4 and 5. In the same way, the motion of the floating crane has a large influence on the contact force. Contrary to case 1 to 3, the time that contact firstly detected is changed due to the different motion amplitudes of the floating crane. In comparison to case 2, where wave

height is 1.0 m, the contact occurs earlier in case 5 as the wave height increases, and later in case 4. Then, the impact occurs in case 5 as the wave height increases, which results in maximum contact force. Case 4 with wave height 0.5 shows the lowest value of the maximum contact force, 24 tons. In case 5, the contact force has maximum value with 108 tons. To sum up, the contact force exerted between the wire rope and the block during the block turnover operation increases with the wave height and decreases with wave period in this application.

4.2. Block lifting by a floating crane

The behavior of the floating crane lifting a block and its mooring system under an irregular wave and current are analyzed. The configuration of the floating crane and its mooring system are shown in Figure 4-9.

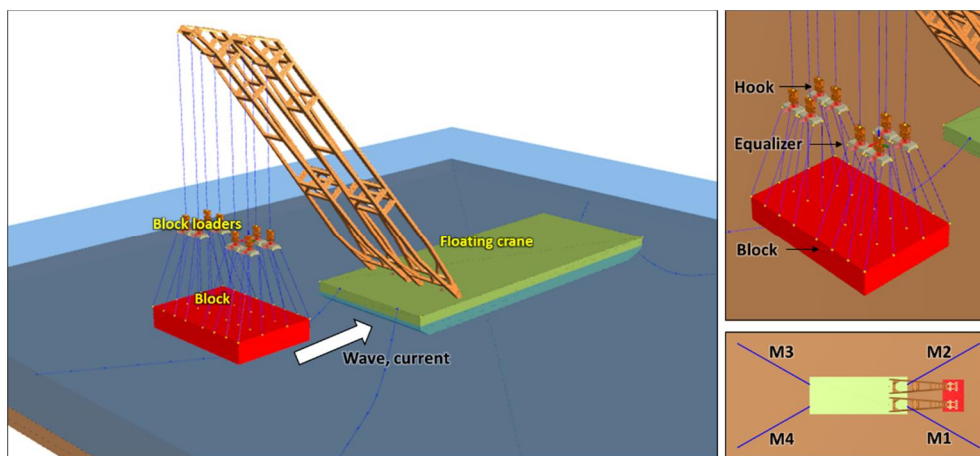


Figure 4-9. Configuration of floating crane lifting a block and its mooring system.

The floating crane is moored to the seabed with mooring lines M1 to M4. The block is connected to the boom of the floating crane with wire ropes, hooks, and equalizers. Eight hooks are connected to the boom, and a hinge joint connects the hook and the equalizer. The slings connected to the block assumed to have the same tension due to the equalizers. The properties of the mooring line and the barge are summarized in Table 4-3.

Table 4-3. Properties of the barge and the mooring line for block lifting by a floating crane.

Property		Value
Barge	Length	183 m
	Breadth	70 m
	Depth	11 m
	Weight	75,060 ton

Mooring line	Weight per length	203.9 kg/m
	Axial stiffness	205,200 kN
	Mooring depth	25 m
	Mooring distance	150 m
	Total unstretched length	161 m

With different environmental loads such as wave and current, three cases are simulated, as presented in Table 4-4. To represent the environmental conditions, we used the Beaufort scale, which is an empirical measurement relating the wind speed to the condition of the sea [66]. The Beaufort number is divided into 12 levels according to wind speed. In case 1, Beaufort number 5 is used which represents the moderate condition, and 7 in case 2, which represents moderate gale. To generate the irregular wave in the time domain, the Joint North Sea Wave Observation Project (JONSWAP) spectrum is used. The direction of the wave and the current is 0 degrees as shown in Figure 4-9.

Table 4-4. Simulation cases with different environmental conditions.

	Application	Wave condition			Current speed [knot]
		Wave type	Significant height [m]	Peak period [sec]	
Case 1	Floating crane (multibody)	Irregular (JONSWAP)	1.65	5.10	2
Case 2		Irregular (JONSWAP)	3.60	6.70	4

Under the irregular wave of moderate and gale conditions, the motion of the floating crane, and the tension of the mooring lines are depicted by the graph in Figure 4-10 and Figure 4-11.

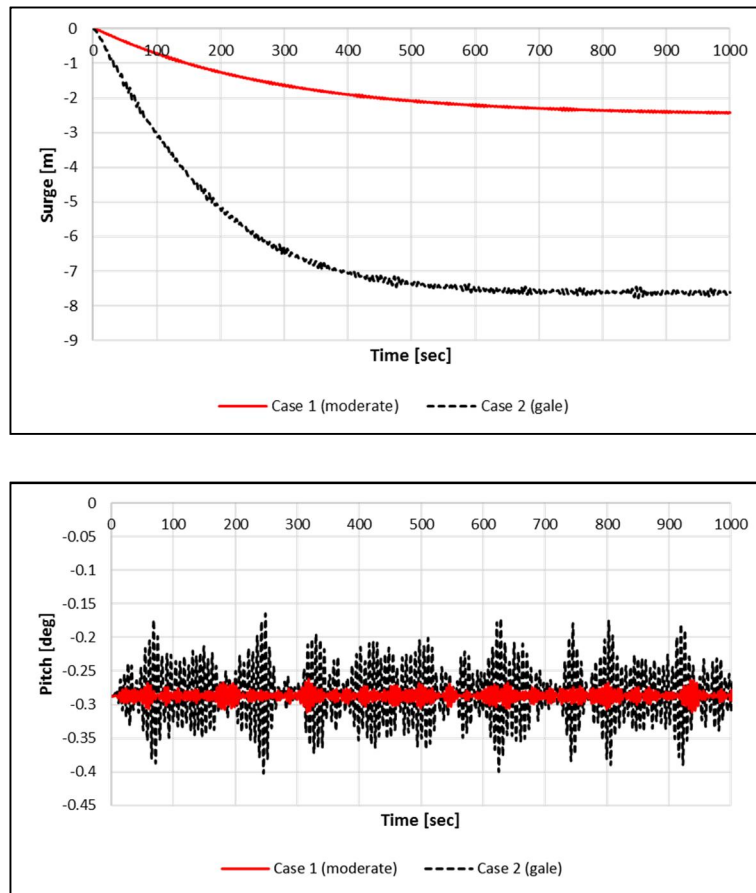


Figure 4-10. The motion of the floating crane under the irregular wave and current.

Figure 4-10 shows the irregular motion of the floating crane under the wave and current. The red solid line depicts the result of case 1, and the black dotted line is that of case 2. The motion of the floating barge and the displacement are the bigger in case 2, due to the harsh environment and high current speed. As shown in the first graph, the floating crane drifts off due to the current and reaches the equilibrium position result from the mooring force. The surge offset of the floating crane after in the equilibrium state is 2.4 m, and 7.6 m in case 1 and 2, respectively. Under the heading sea, the wave induces the pitch motion of the floating barge. The bottom graph shows the offset of the pitch

angle. The maximum pitch angle is 0.03 degrees in case 1, and 0.12 degrees in case 2. The wave, current, and the coupling effect with the block and equalizers affects the pitch motion of the floating crane. Graphs in Figure 4-11 show the tension of each mooring line.

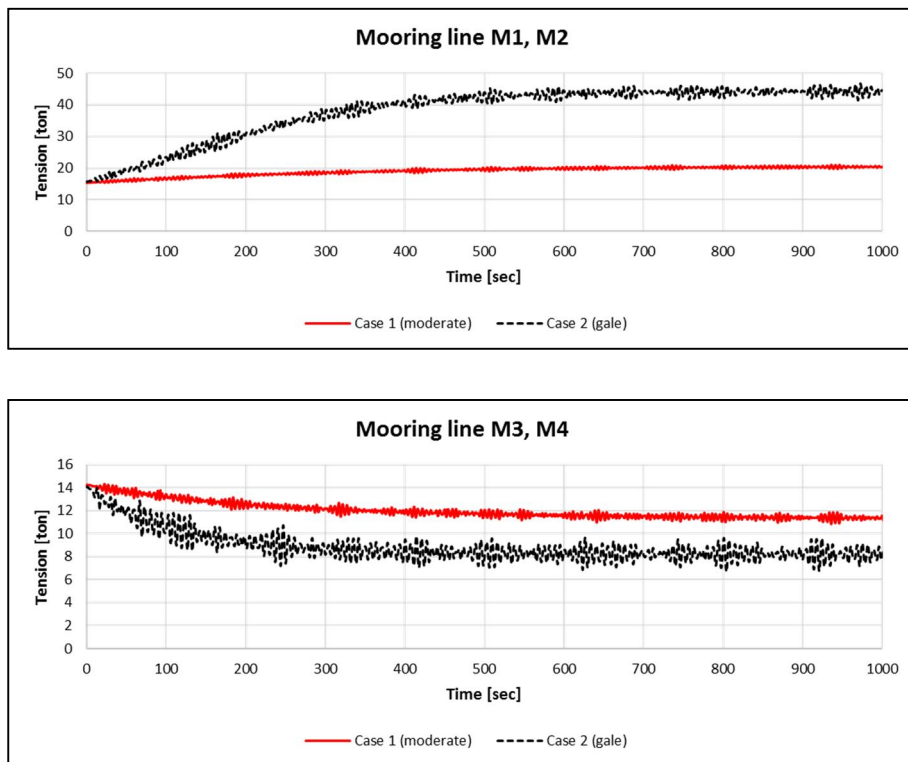


Figure 4-11. The tension of the mooring lines under the irregular wave and current.

The motion of the floating crane and the current force exerted on the mooring line itself affects the tension of the mooring lines. The initial tension of the mooring lines is approximately 15 tons. The tension of the mooring line shows the same tendency in both cases. In the heading sea environment, the floating crane drifts due to the current force. Therefore, the mooring lines connected to the bow of the floating barge are stretched, and those connected to the stern are compressed. As a result, the tension of the mooring lines

M1 and M2 increase as presented in the graph above, while the tension of mooring line M3 and M4 decrease. The tension of the mooring lines reaches the equilibrium state similarly to the surge displacement of the floating crane. The maximum tension of the mooring line for each case is 21.3 tons and 46.8 tons, respectively.

4.3. Crane control for block erection

To develop the automated crane control methods and verify them, the inverse dynamics solver is applied to two block erection simulations by a gantry crane and a floating crane. The motion of the actual mechanical system is obtained from the simulation using DELE.

4.3.1. Gantry crane control

The gantry crane model is the same as the verification example, as presented in Figure 4-12. The crane consists of a controllable crane girder and two trolleys, and three wire ropes. Three hooks and equalizers are connected to the trolley with the wire ropes. The upper trolley connects two hooks, which hold one side of the block, and the lower trolley holds the other side with one hook. The properties of the block are as shown in Figure 4-12. The weight of the block is assumed 300 tons, and the lifting capacity of the gantry crane is 900 tons.

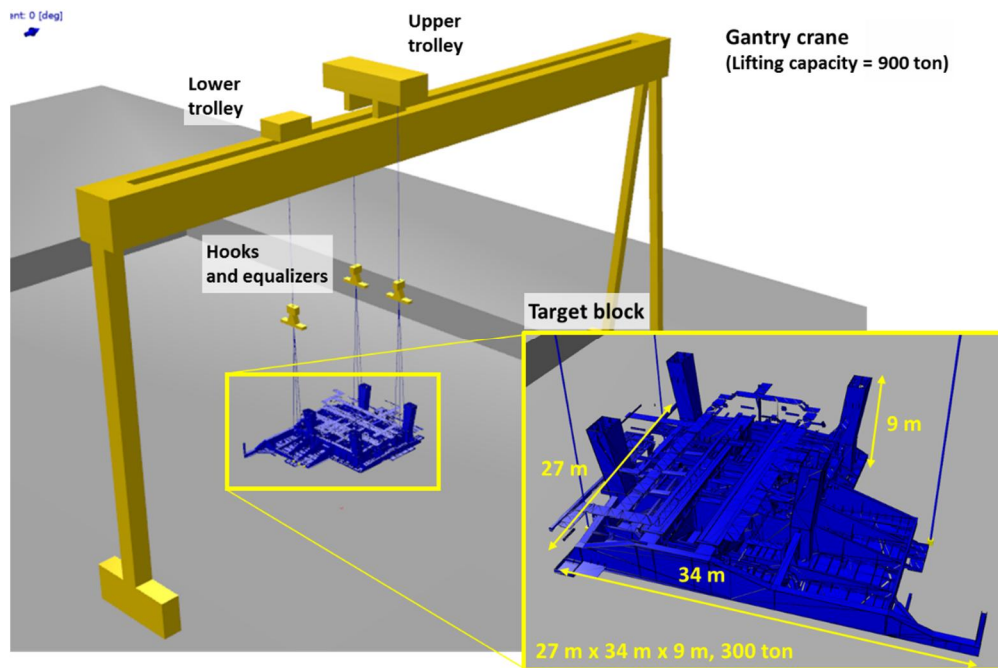


Figure 4-12. Configuration of the gantry crane and the block.

The initial and final position of the block is the same as the verification example illustrated in Figure 3-20. The initial position of the block is $(0, 0, 20)$, and the final position is $(25, 10, 10)$, rotated with 90 degrees. Therefore, the block is transported by 25 m in the x-direction and 10 m in the y-direction, and rotated by 90 degrees at the same time.

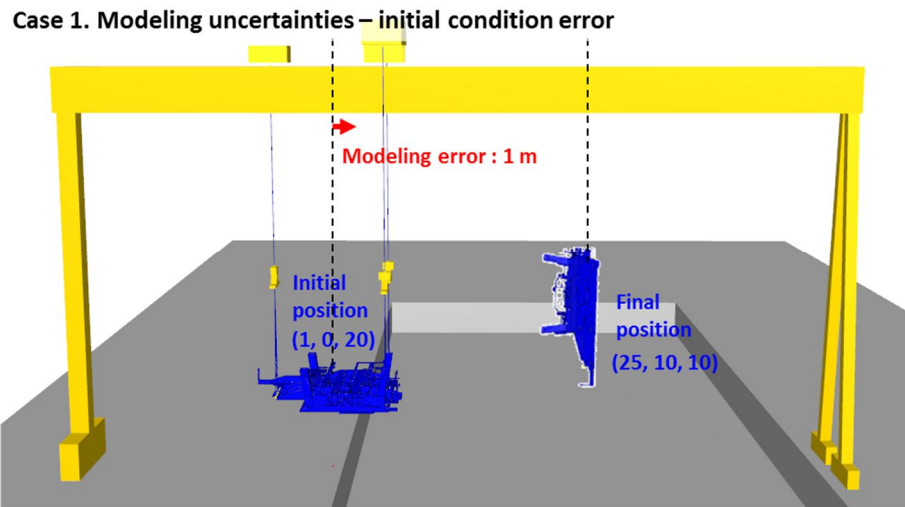


Figure 4-13. Gantry crane system with modeling uncertainties.

To investigate the effect of the control method under the modeling uncertainties and external disturbances, two cases are performed. As illustrated in Figure 4-13, the initial condition error at the position of the block exists as a modeling uncertainty in case 1. The block is initially located at the position $(1, 0, 20)$, deviated from the desired trajectory by 1 m. Then, the resultant motion of the block is as follows (Figure 4-14).

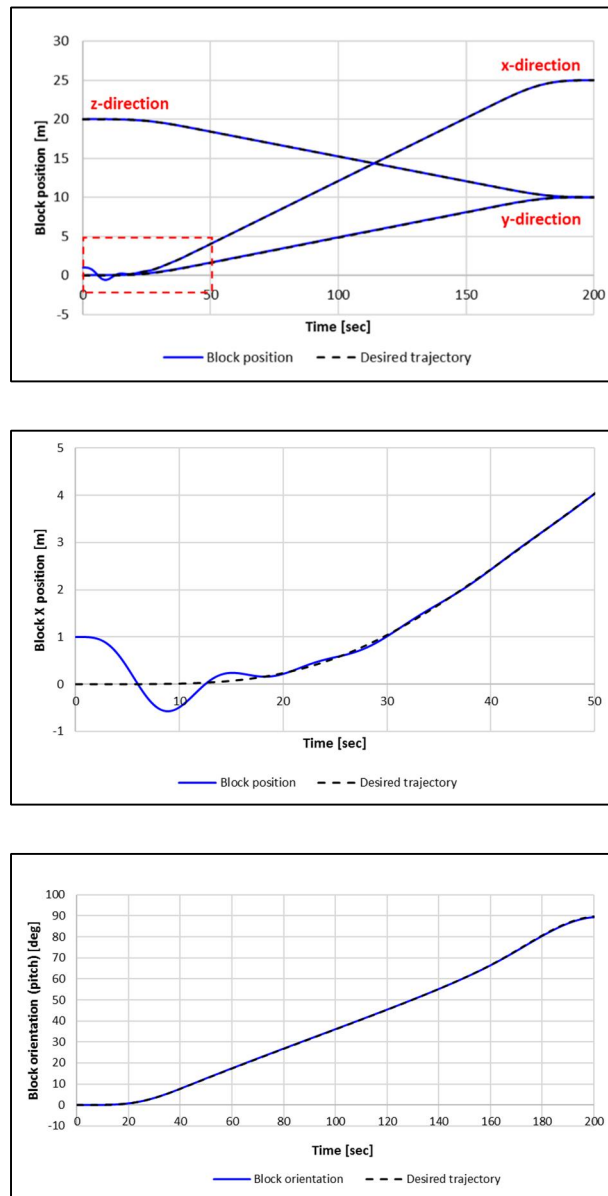


Figure 4-14. Motion of the block with modeling uncertainty.

Due to the modeling error, the block is 1 m apart from the desired trajectory in the x-direction, depicted in a dotted black line at the beginning. Then, the block is controlled to follow the target trajectory properly within 40 seconds. The rotation angle and y, z

position follows the desired value exactly with no perturbations. The inverse dynamics solver developed in this study calculates the control inputs to control the motion of the block. The control inputs are obtained as depicted in Figure 4-15.

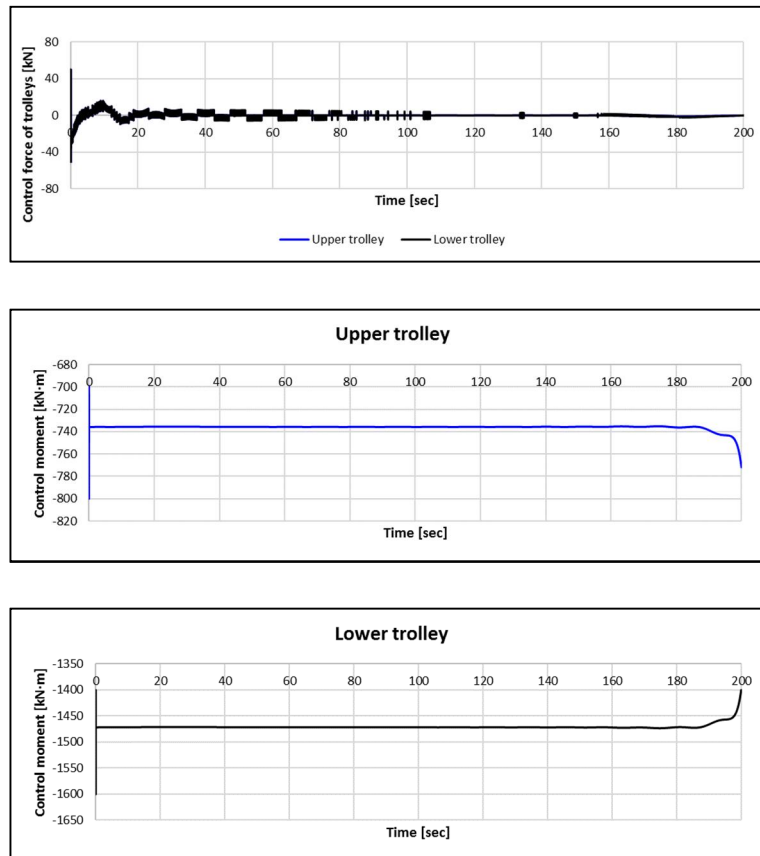


Figure 4-15. Control inputs of the gantry crane with modeling uncertainty.

The control force and moment exerted on the winch and the trolleys are the control input of this system. The control force of trolleys increases at the beginning to force the block to track the trajectory. In the actual hardware, the maximum force output of the drive system is limited. Thus, the maximum control force and the moment are also

applied to the simulation in this example. The maximum control force exerted on the trolleys is assumed 50 kN. The control inputs reach a maximum value at the beginning that block deviates from the desired trajectory, and decrease as it follows the trajectory. The control moment exerted on the winch of upper and lower trolley remains constant during the operation, as the hoisting speed is constant. Then, it changes as the block is turned over at the end because the motion of the trolleys changes the length of the wire ropes. The motion of the crane system caused by the control input is as presented in Figure 4-16.

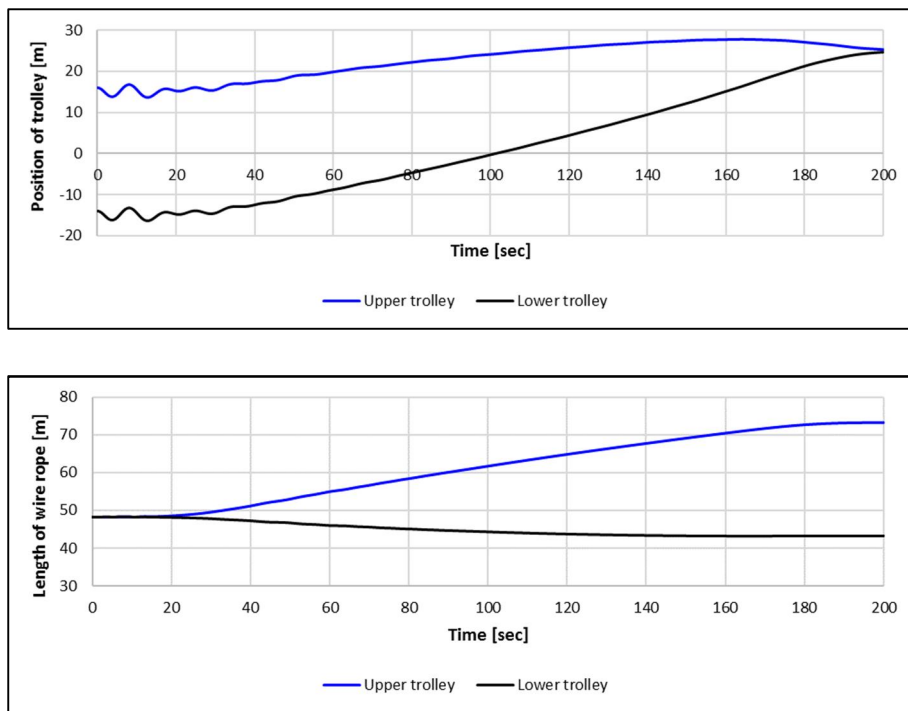


Figure 4-16. Length of the wire rope and the motion of the trolley with modeling uncertainty.

The control input is directly applied to the crane girder, trolleys, and wire ropes. As there are no external forces and modeling uncertainties in the y-direction, the crane girder

is fixed to the ground during the operation. The trolleys oscillate at the early part to control the motion of the block in the x-direction. The length of the wire ropes are changed by the control moment exerted on the winches. The length of the wire ropes changes almost linearly in the middle due to constant control moments. Then, it is smoothly controlled to turn over the block following the desired pitch angle.

In case 2, the environmental load is exerted on the block as the external force. The irregular wind is applied to the block with a mean speed of 10 m/s and a direction of 45 degrees (Figure 4-17).

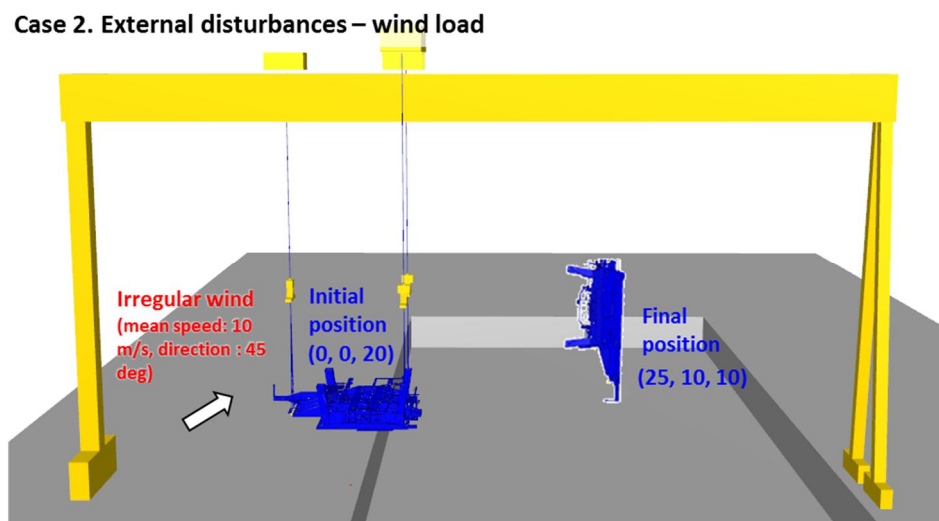


Figure 4-17. Gantry crane system with external disturbances.

The wind fluctuation is calculated from the NPD wind spectrum given by ISO 19901-1, where $U(H)$ is the mean wind speed at H above the water plane.

$$S(f) = \frac{320 \cdot \left(\frac{U(10)}{10}\right)^2 \cdot \left(\frac{H}{10}\right)^{0.45}}{\left(1 + f_m^n\right)^{\frac{5}{3n}}} \quad (114)$$

$$f_m = 172 \cdot f \cdot \left(\frac{H}{10}\right)^{\frac{2}{3}} \cdot \left(\frac{U(10)}{10}\right)^{-0.75}$$

The wind speed in the time domain can be obtained as the summation of the mean wind speed at H and the wind fluctuation. In case 2, the wind speed with a mean speed of 10 m/s is as follows in Figure 4-18.

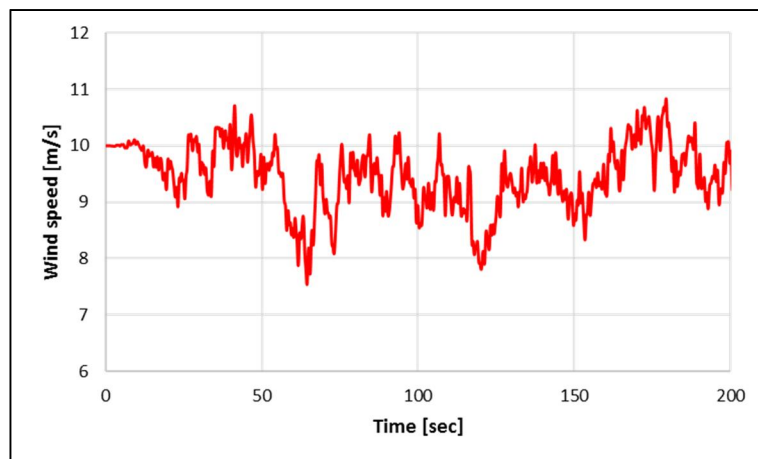


Figure 4-18. Irregular wind speed from the NPD spectrum.

Then, the wind load is calculated by the equation below.

$$\begin{aligned}
F_x &= C_x \frac{1}{2} \rho_{air} V(t)_{wind}^2 A_f \\
F_y &= C_y \frac{1}{2} \rho_{air} V(t)_{wind}^2 A_s \quad , \\
M_z &= C_N \frac{1}{2} \rho_{air} V(t)_{wind}^2 A_s L_{oa}
\end{aligned}
\tag{115}$$

where ρ_{air} is the air density, C_x , C_y , and C_N are the coefficients that are obtained by experiment, A_f and A_s is the projected frontal and side area, and $V(t)_{wind}$ is the wind speed.

The result of the simulation is as shown in Figure 4-19.

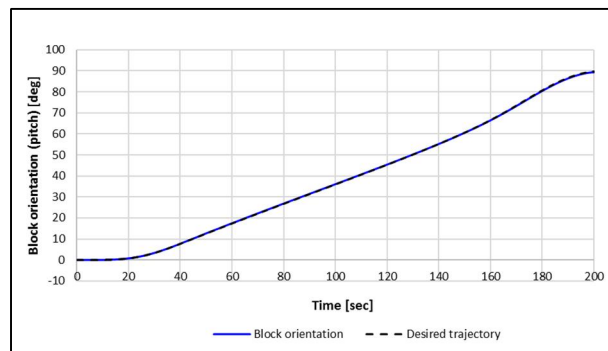
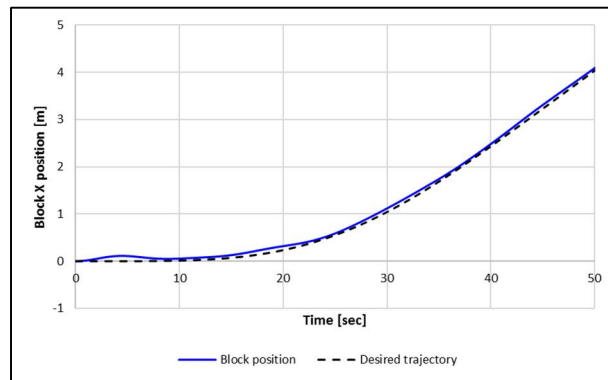
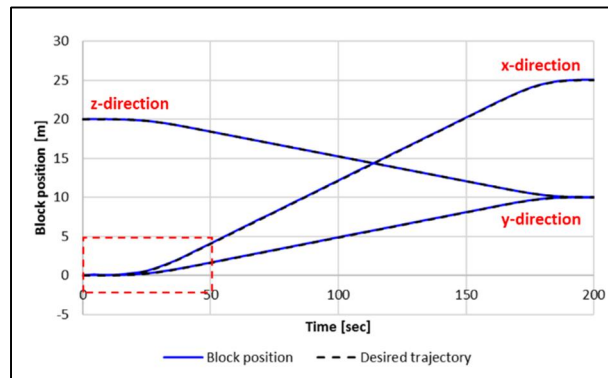


Figure 4-19. Motion of the block with wind load.

The block tracks the desired trajectory properly, and the distance error in the x-direction due to the wind load is about 7 cm, which is sufficiently small. The perturbation of the motion of the block exists due to wind, but the block follows the target trajectory

well. The control forces exerted on the trolleys and winches are presented in Figure 4-20.

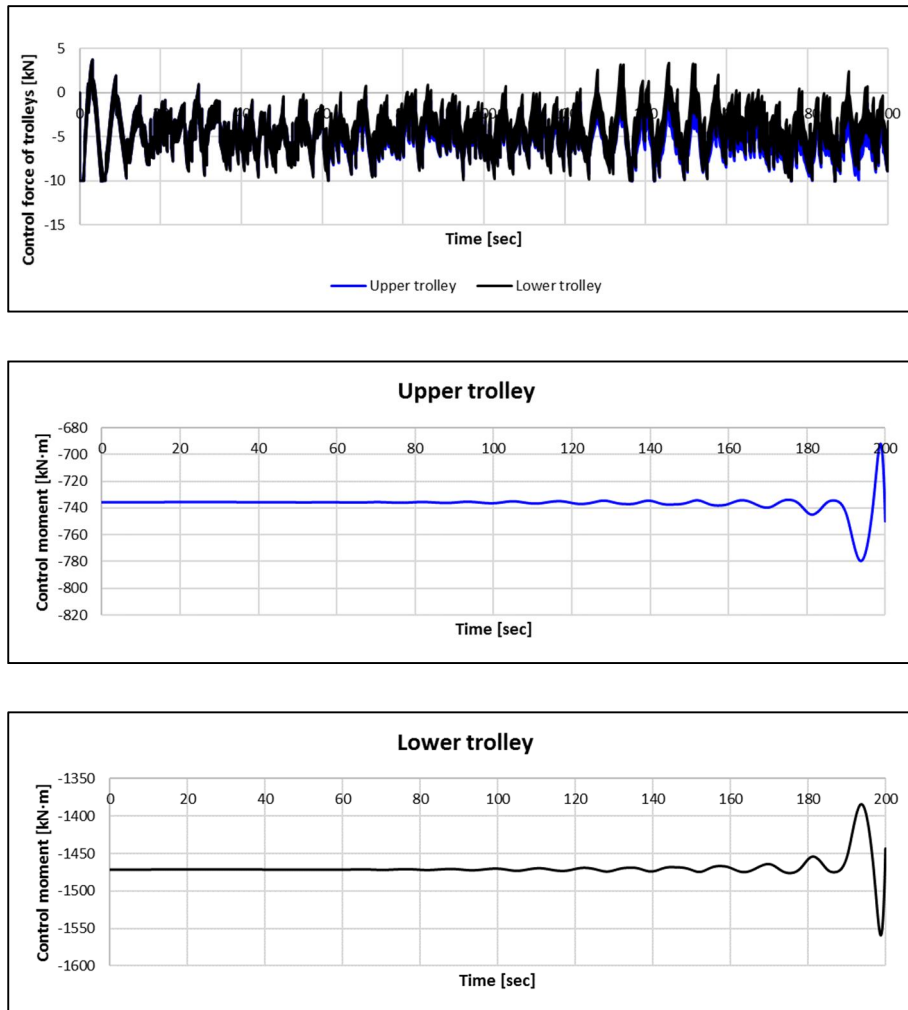


Figure 4-20. Control inputs of the gantry crane with external disturbances.

The control force and moment are applied to the crane system to control the motion of the block. As presented in the first graph in Figure 4-20, the control force is mostly negative, which implies that the direction of the control forces is opposite to x-direction to compensate for the wind force. The control moment for winches of upper and lower

trolleys also oscillates due to the external force. The oscillation of the control moment increases as the block turned over, due to the coupling with the motion of the trolleys. The length of the wire ropes and the motion of the trolleys are depicted in Figure 4-21.

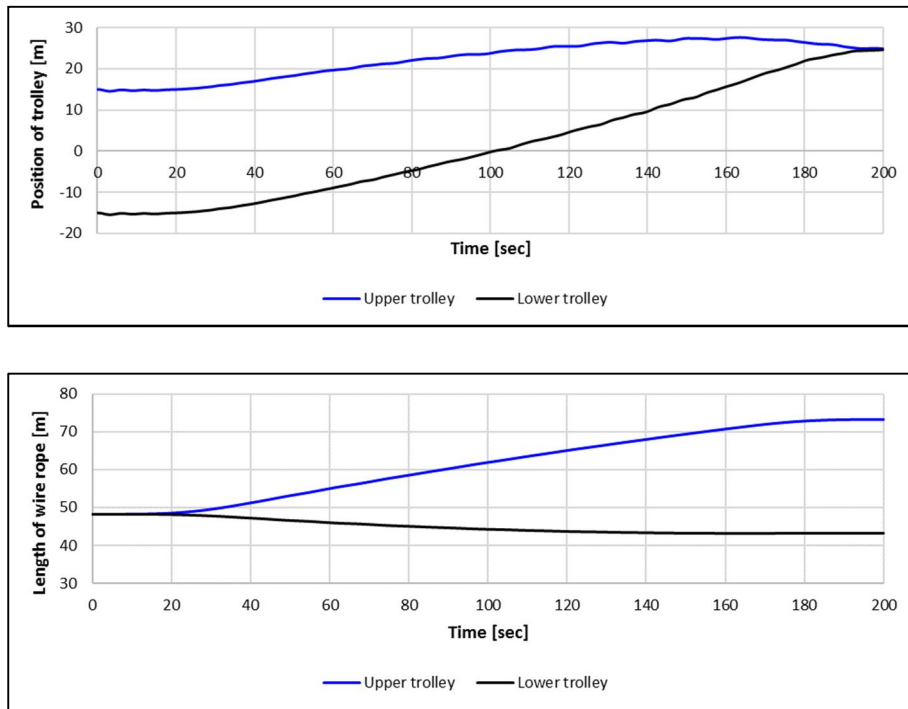


Figure 4-21. Length of the wire rope and the motion of the trolley with external disturbances.

The control input induces the motion of the crane system. The motion of the trolley has perturbations to control the block in the presence of the wind load. The position of the upper and lower trolley coincides at the end as the block rotates with 90 degrees. The wind load does not affect the length of the wire rope much similarly to case 1.

4.3.2. Floating crane control

With the same control method, the floating crane is controlled for the block erection in this section. The configuration of the floating crane and the block is illustrated in Figure 4-22.

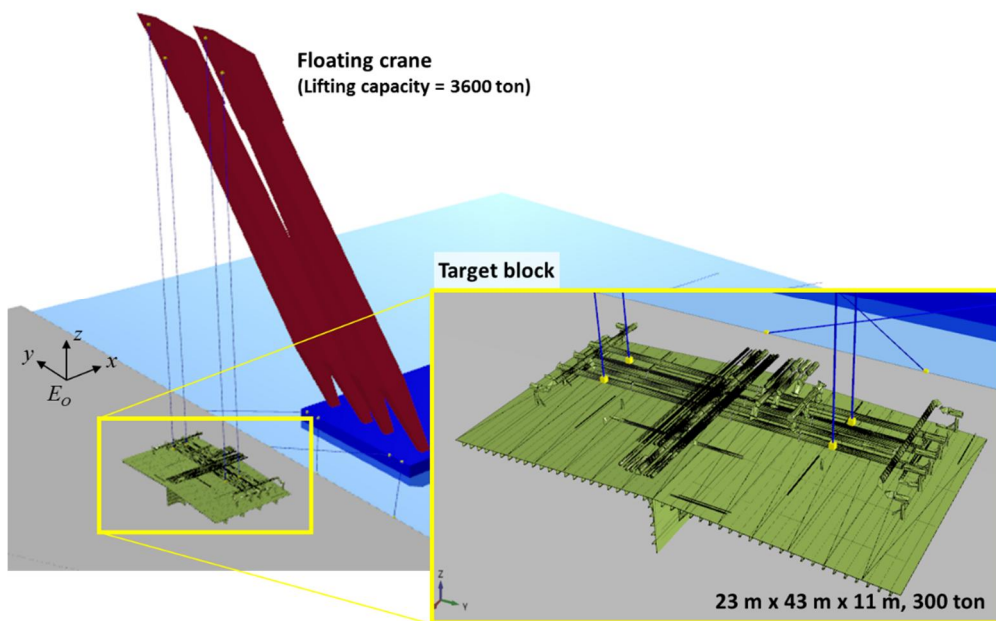


Figure 4-22. Configuration of the floating crane and the block.

The floating crane has two booms and four wire ropes to lift the target block. The length, breadth, and height of the block is 23 m, 43 m, and 11 m, and its weight is 300 ton. The lifting capacity of the floating crane is 3600 tons. The floating crane is moored to the quay and the seabed with mooring lines, which is modeled with massless springs. The properties of the floating crane are shown in Table 4-5.

Table 4-5. Properties of the floating crane for the control of block erection.

Property		Value
Barge	Length	110 m
	Breadth	46 m
	Depth	7.5 m
	Weight	18,851 ton

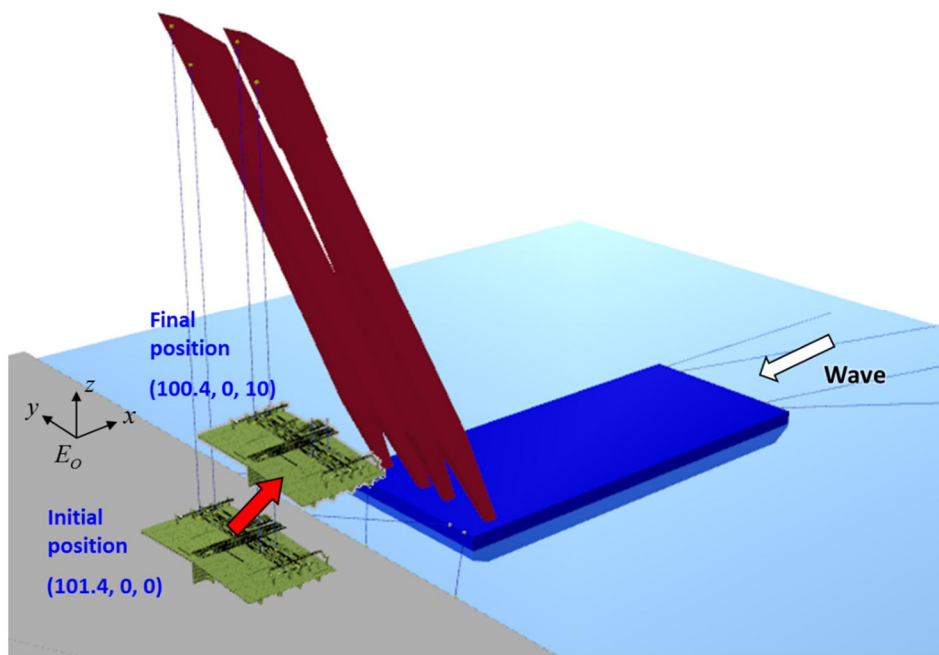


Figure 4-23. Desired trajectory of the block lifted by a floating crane.

The desired trajectory of the block is as shown in Figure 4-23. The floating crane lifts the block by 10 m, and move 1 m in the x-direction by standing the booms. The wave is applied to the floating crane from the stern. Two cases are performed with different wave conditions using Beaufort numbers 5 and 7. The irregular wave is assumed from the JONSWAP spectrum. The test cases and the wave condition are as summarized below.

Table 4-6. Test cases of the block erection control by a floating crane.

	Wave condition			Direction
	Wave type	Significant height [m]	Peak period [sec]	
Case 1	Irregular (JONSWAP)	1.65	5.10	0
Case 2	Irregular (JONSWAP)	3.60	6.70	

Under the wave condition, the heave and pitch motion of the floating crane is calculated in Figure 4-24. The surge of the crane is neglected as the mooring lines are connected to the floating barge to prevent drift.

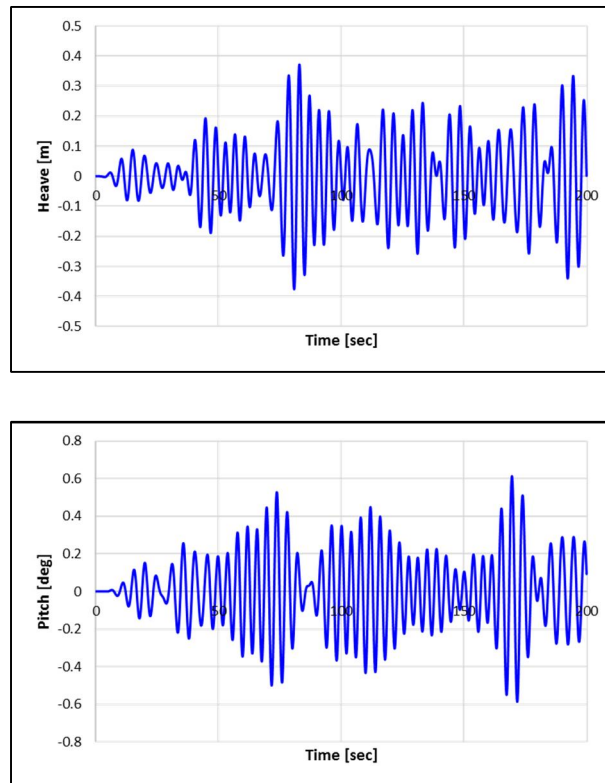


Figure 4-24. Motion of the floating crane in case 1.

The maximum heave offset and pitch angle of the floating crane are 0.38 m and 0.61 degrees. The drive system controls the motion of the block to track the desired trajectory regardless of the motion of the floating crane. The result of case 1 is depicted as a graph in Figure 4-25. The block follows the target trajectory accurately under the wave load.

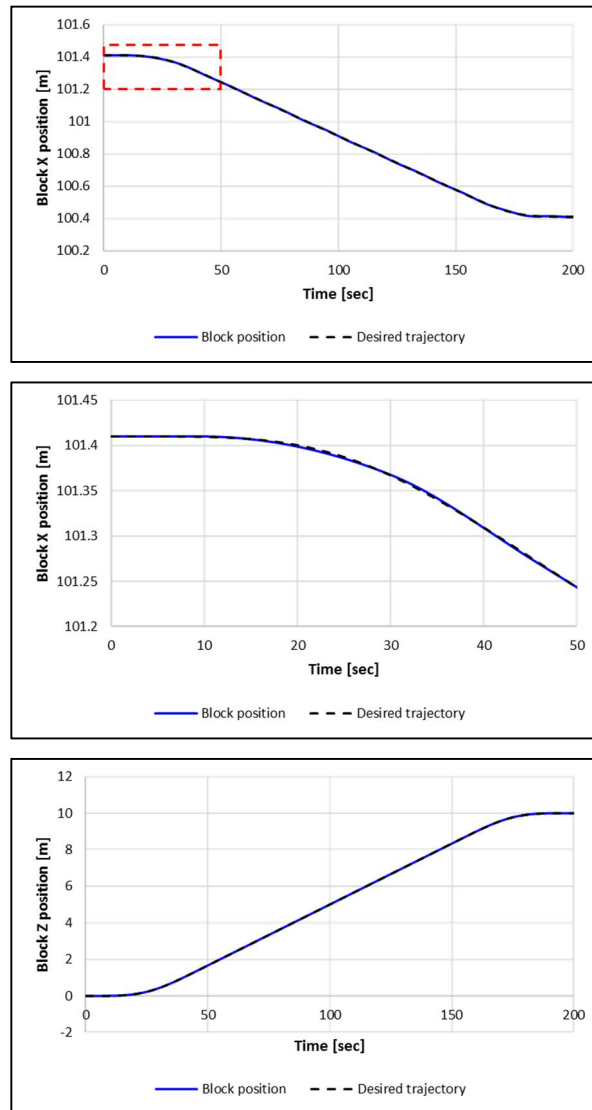


Figure 4-25. Position of the block controlled by the floating crane in case 1.

The block position along x and z-axis track the desired trajectory in moderate wave condition. As presented in the second graph in the figure above, there is a small error between the target trajectory and the actual path due to the wave, which has a maximum value of 0.003 m. The motion of the barge under the wave condition is considered as an input in the inverse dynamics solver. Then, the control force to control the angle of the boom and the length of the wire ropes are obtained. As a result, the motion of the crane system is calculated as shown in Figure 4-26 below.

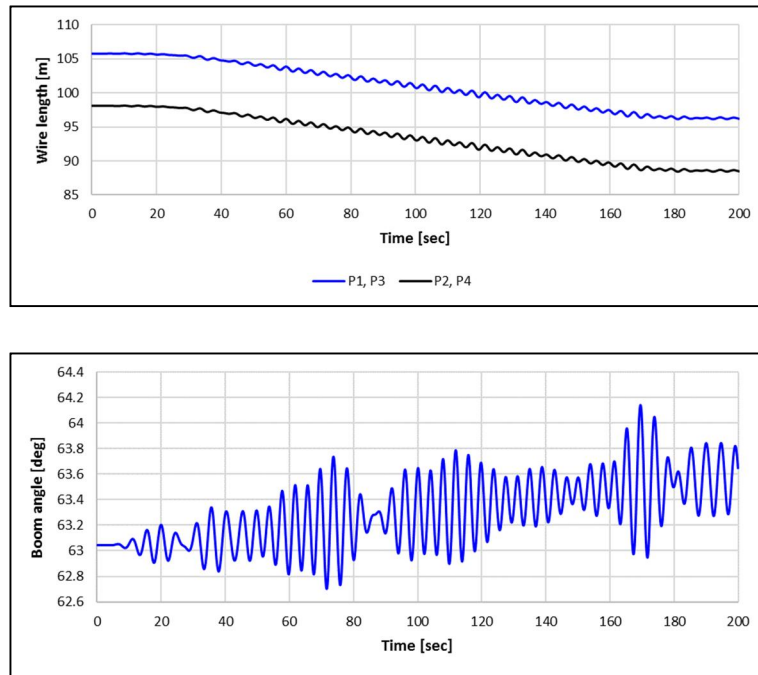


Figure 4-26. Boom angle and the length of the wire ropes of the floating crane in case 1.

The drive system oscillates to compensate for the motion due to waves to control the block. The angle of the boom controls the position of the block along the x-axis, and the length of the wire rope coupled with the boom angle restrains the position along the z-

axis. During the operation, the total tension of the wire ropes connected to the block is changed as depicted in Figure 4-27.

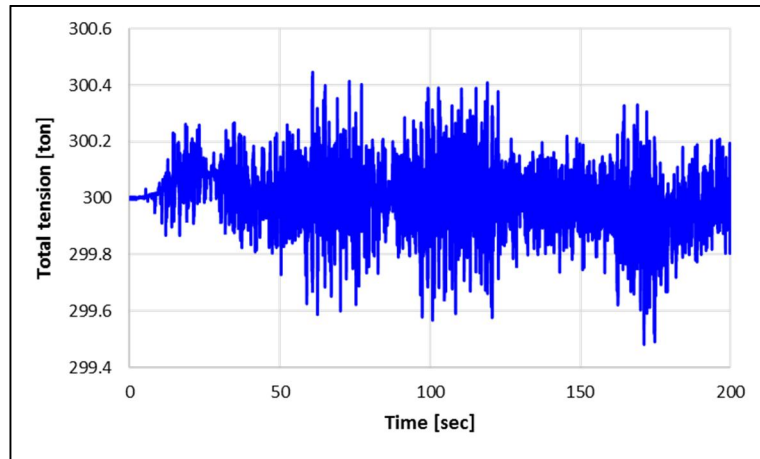


Figure 4-27. Total tension of the wire ropes connected to the block in case 1.

The weight of the block is 300 tons, and the fluctuation of the tension occurs according to the dynamic motion of the block. The maximum and minimum tension are 300.45 tons, and 299.48 tons in case 1. The dynamic amplification factor is then 1.002.

In case 2, the same control operation is assumed in a harsh environment. The heave and pitch offset of the floating crane are presented in Figure 4-28.

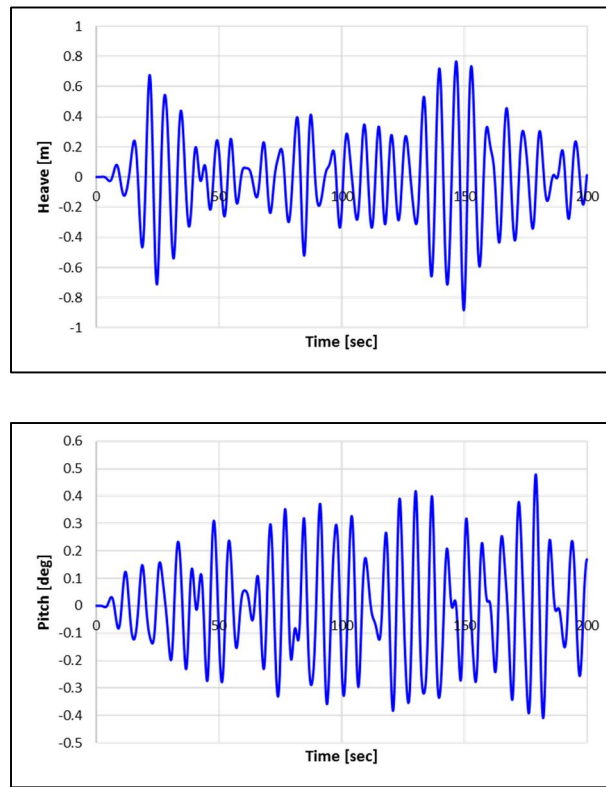


Figure 4-28. Motion of the floating crane in case 2.

In case 2, the maximum offset of heave and pitch are 0.88 m and 0.41 degrees. The heave motion is much bigger than that in case 1, as the wave height is increased. However, the pitch motion is smaller due to the resonance of the floating barge in a small wave period. In the same way, the position of the block is controlled by the drive system as shown in Figure 4-29.

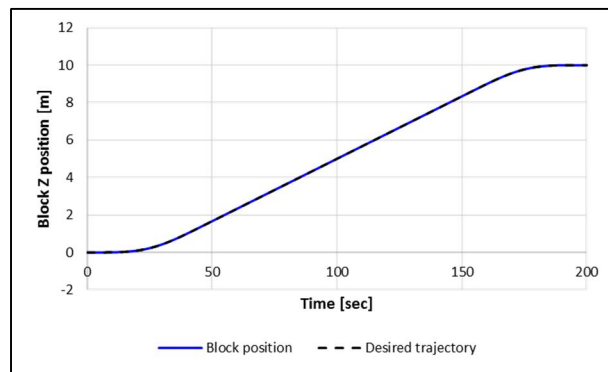
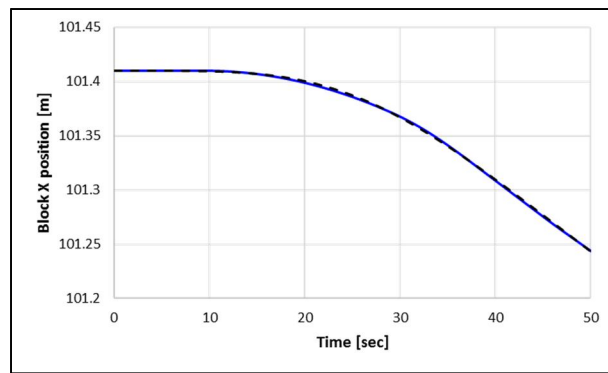
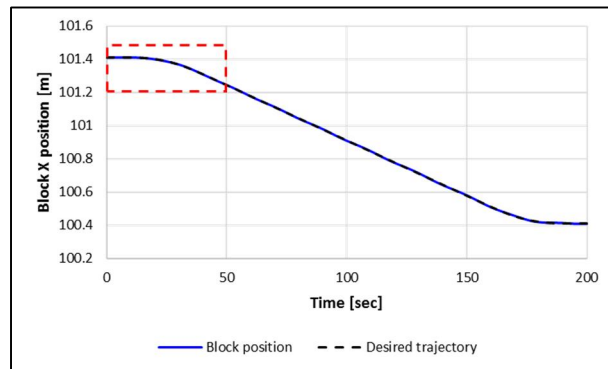


Figure 4-29. Position of the block controlled by the floating crane in case 2.

The motion of the block is precisely controlled in case 2. The maximum error between the position of the block and the desired trajectory is 0.003 m, which is almost the same as case 1. The motion of the drive system is depicted in the following graphs.

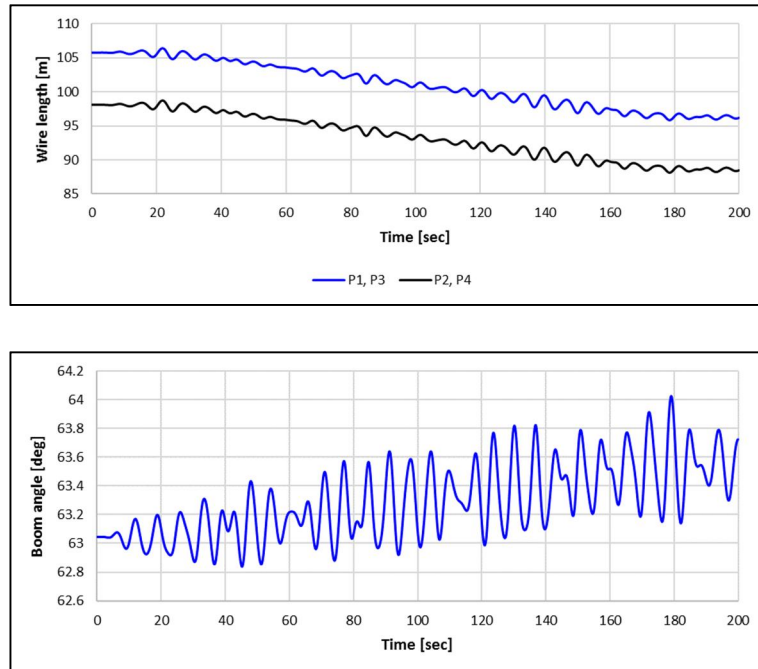


Figure 4-30. Boom angle and the length of the wire ropes of the floating crane in case 2.

As presented in Figure 4-30, the boom angle and the length of the wire ropes oscillate to compensate for the motion due to waves for the control of the block. As the heave motion of the barge in case 2 is bigger, the length of the wire rope changes with a large amplitude. The pitch angle of the barge decreases with a large wave period, which leads to a smaller range of fluctuation of the boom angle in case 2. The mooring lines prevent the drift of the floating barge due to waves. Lastly, the tension of the wire ropes is obtained as depicted in Figure 4-31.

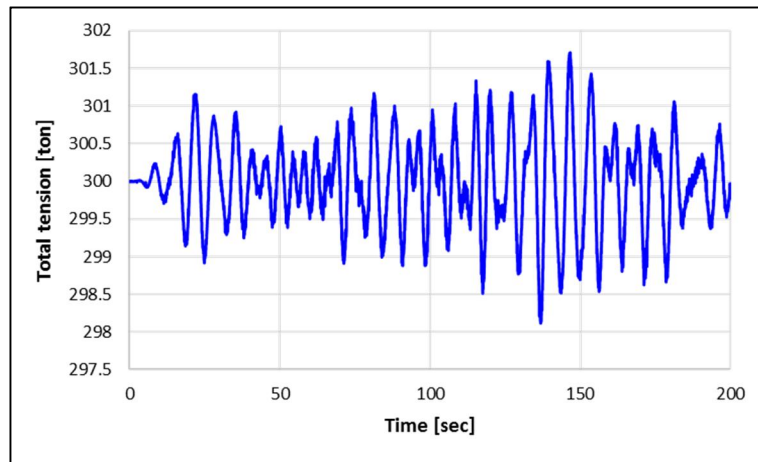


Figure 4-31. Total tension of the wire ropes connected to the block in case 2.

The maximum and minimum tension is 301.77 tons and 298.05 tons in case 2, and the dynamic amplification factor is 1.006. The tension exerted on the block has a bigger range of fluctuation in a harsh environment with bigger wave height.

5. Conclusions and future works

5.1. Summary

This study focused on advanced simulation and automated control for safe and efficient block erection operation and accurate analysis. For the physics-based simulation, which reflects actual operation, the interferences between the body and the wire rope were analyzed during the block turnover operation. The coupled analysis of the floating crane and the mooring system was also performed considering the contact with the seabed. Finally, for the automated control of the crane, the inverse dynamics solver was formulated. The modules for the simulation core, simulation components, and inverse dynamics of the physics-based simulation were developed and integrated into the existing simulation program.

Firstly, the theoretical backgrounds of the multibody dynamics were introduced for the development of the simulation core. The multibody dynamics equations for the rigid and flexible bodies were formulated using DELE, combined with ANCF. The equations of motion for 1D-beam elements were constructed to model the flexible mooring line. The kinematic constraints between the rigid bodies and 1D flexible bodies were also included for the application to the multibody system.

Two types of the wire rope model were adopted in this study to model the interferences with bodies, and to model the mooring lines. The constraint-based model was used to create the wire ropes considering interferences, which is appropriate to reflect the interaction with the bodies without much increase in the simulation cost. The stretching, bending, and torsion constraints were formulated to model the wire rope with

constraints. The mooring line model was generated by joining multiple 1D flexible beams using the analytic solution of the catenary mooring line.

We realized the interaction between the wire rope and body using contact, sliding, and friction model. In the contact model, the contact node was generated by contact detection algorithm and removed according to the calculated contact force. The sliding motion of the contact node was divided into the sliding along the wire rope and the edge of the body. Then, the motion of the wire rope and the body was calculated under the static and kinetic frictional forces. The interaction between the mooring line and the seabed was also carried out. The collision with the seabed was realized using two kinds of constraints, non-interpenetration and slope constraint, which is appropriate for the flexible mooring line model. We included static and kinetic friction with the seabed for the dynamic analysis.

For the automated control of the crane system, the characteristics of the underactuated system and the control method was presented. The trajectory tracking control of the underactuated system using the concept of servo constraint was explained for better performance. To formulate the inverse dynamics solver, including the servo constraints and the dynamic equations, the equations of motion of the drive system and the block were derived for a gantry crane and a floating crane system. Finally, the inverse dynamics solver was obtained by combining the feedforward and feedback control method. The index reduction method was adopted for stable numerical analysis.

We provided several verification examples compared with the analytic solutions or commercial software to increase the reliability of suggested methods. The test examples and methods are summarized in Table 5-1.

Table 5-1. Verification examples for suggested models.

Model		Tests		Method
Wire-body interference model	Contact model	Box dropping test	Analytic solution	Comparison of the motion of the box and the tension of the wire rope considering contact
	Friction model	Sliding along the edge	Coulomb friction model	Comparison of the acceleration with different friction coefficients
		Sliding along the wire rope		
Sliding model	Unbalanced box dropping test	.	Check if the result of the two same boxes with different mesh is the same.	
Mooring model		Convergence test	.	Convergence test of mooring line according to the number of the element
		Static analysis	Analytic solution/ OrcaFlex	Comparison of deflection, penetration depth, and tension
		Dynamic analysis	OrcaFlex	Comparison of tension at the fairlead
Inverse dynamics of the underactuated system		Control of the gantry crane	.	Check if the block tracks the desired trajectory.

Finally, four representative applications of block erection operations were provided. The block turnover operation considering interferences and block lifting by a floating crane with a mooring system are simulated for the realization of actual operation. Then, the trajectory tracking control of the block by the gantry crane and the floating crane is performed with the suggested control method. We concluded that the suggested methods solve the requirements for advanced simulation and control methods. We convinced that the developed modules integrated into the multibody dynamics program could be applied to the validation and the control of block erection operations in shipyards.

5.2. Contributions (Originality)

This study has several contributions distinguished from the other works.

5.2.1. Theoretical contributions

The multibody dynamics equations are formulated to be integrated with various flexible wire rope models. Firstly, the concept of constraint-based wire rope model is introduced, and included in DELE. The contacts between the wire rope and the rigid body are also represented by constraint equations to be solved integrated with the multibody dynamics formulation. Secondly, the multibody dynamics equations are formulated using DELE integrated with ANCF for a flexible beam element. For this, the constraint equations for the joint between the rigid and flexible bodies are derived. Furthermore, the 3rd order shape function was adopted for the beam element to consider both stretching and bending of the mooring lines. As a result, a fully coupled analysis of the multibody system and the mooring system was performed. For the automation of the block erection operation, the theoretical backgrounds of the control method for the underactuated crane system is proposed for the cranes in shipyards.

5.2.2. Numerical contributions

In this study, advanced simulation techniques are introduced that can improve the accuracy and efficiency of the existing simulation. Firstly, the interaction algorithm between the wire rope and the block is suggested. This model can realize the contact, sliding, and frictional force of wire rope efficiently, which are difficult to be considered in the massless spring model used in the traditional simulation. The suggested model requires two constraints per one wire rope at most, regardless of the number of the

segments. This enables the interference analysis of the block turnover operation, which were impossible with existing researches without a large increase in the simulation cost. For the mooring line analysis, the fully coupled analysis of the multibody system and the mooring lines are performed which does not require iteration process. Besides, the contact with the seabed was modeled mathematically by using non-interpenetration constraint and slope constraint. It can realize the contact with the seabed accurately and can be easily applied to the uneven seabed.

For the automated control method for the underactuated crane system, the inverse dynamics solver for the gantry crane and the floating crane is formulated for the trajectory tracking control. Then, the mechanical system was modeled by using DELE, which contains complex equipment in actual crane system. The control method of the gantry crane system considering trolleys, hooks, and equalizers was suggested in this study. In addition, the trajectory tracking control of the floating crane was performed, which the environmental loads directly affect the drive system.

5.2.3. Contributions for application

The accuracy and reliability of the proposed model and methods were checked in the verification examples. Then, we presented various applications of the block erection simulation using suggested methods. The result showed that the method could be properly used for the simulation to validate the actual operation. The proposed models and methods were all integrated with the existing simulation program to expand the applicability to the various kind of operation methods.

5.2.4. Other contributions

The proposed wire rope models, interaction algorithms, and control methods were all

developed as modules in C# programming language. They are integrated into the production design verification program, SyMAP, for extended applications and practical use. Thus, the suggested methods can be employed to other applications other than block erection operation and can be combined with other simulation techniques in the future.

5.3. Future works

Future research will focus on the validation and improvement of the suggested methods. The interference algorithm of the wire rope will be improved by considering the dynamics of the wire rope. Then, the suggested wire rope model will be evaluated by the comparison with the actual experimental result. Moreover, the HILS (Hardware-In-the-Loop Simulation) environment will be constructed for the validation of the suggested control method. Finally, the simulation results will be compared with actual operations through collaboration with the shipyard to validate and improve the reliability of the proposed methods.

Reference

- [1] M. Servin, C. Lacoursiere, F. Nordfelth, and K. Bodin, "Hybrid, multiresolution wires with massless frictional contacts," *IEEE trans. on Visualization and Computer Graphics*, vol. 17, no. 7, pp. 970-982, 2011.
- [2] S. Ha, N. Ku, and M.I. Roh, "Event-based scenario manager for multibody dynamics simulation of heavy load lifting operations in shipyards," *Int. J. of Naval Architecture and Ocean Eng.*, vol.8, pp. 83-101, 2016.
- [3] X. Li, M.I. Roh, and S.H. Ham, "A collaborative simulation in shipbuilding and the offshore installation based on the integration of the dynamic analysis, virtual reality, and control devices," *Int. J. of Naval Architecture and Ocean Eng.*, vol.11, pp. 699-722, 2019.
- [4] A. Jo, N. Ku, J.H. Cha, K.P. Park, and K.Y. Lee, "Simulation of contacts between wire rope and shell plate of a block for shipbuilding industry based on multibody dynamics," *Trans. of the Society of CAD/CAM Engineers*, vol.17, no. 5, pp. 324-332, 2012.
- [5] H.W. Lee, M.I. Roh, and S.H. Ham, "Block turnover simulation considering the interferences between the block and wire ropes in shipbuilding," *Automation in Construction*, vol.67, pp. 60-75, 2016.
- [6] Y.G. Tang, R.Y. Zhang, L.Q. Liu, and N. Hu, "Dynamic tension of mooring system in deep sea with finite element method," *The Ocean Engineering*, vol. 27, pp. 10-15, 2009.
- [7] O.M. Faltinsen, *Sea loads on ships and offshore structures*. Cambridge University Press, New York, 1990.
- [8] T.S. Walton and H. Polachek, *Calculation of nonlinear transient motion of cables (technical report)*. David Taylor Model Basin, Washington, D.C., 1959.
- [9] N. Khan and K. Ansari, "On the dynamics of a multicomponent mooring line," *Computers & Structures*, vol. 22, pp. 311-334, 1986.
- [10] G. Ma, L. Sun, Y. Kang and L. Xu, "Effects of different influence factors on static and dynamic analysis of mooring line," *International Journal of Engineering and Technology*, vol. 7, no. 2, pp. 95-102, 2015.
- [11] K.J. bathe, *Finite element procedures*. 2nd Edition, Prentice Hall, Watertown, 2014.
- [12] H.W. Lee, M.I. Roh, and S.H. Ham, "Coupled analysis method of a mooring system and a floating crane based on flexible multibody dynamics considering

- contact with seabed,” *Ocean Engineering*, vol.163, pp. 555-569, 2018.
- [13] H.J. Tang, C.C. Huang, and W.M. Chen, “Dynamics of dual pontoon floating structure for cage aquaculture in a two-dimensional numerical wave tank,” *Journal of Fluids and Structures*, vol.27, pp. 918-936, 2011.
- [14] S.H. Ham, M.I. Roh, H.W. Lee, J.W. Hong, and H.R. Lee, “Development and validation of a simulation-based safety evaluation program for a mega floating crane,” *Advances in Engineering Software*, vol.112, pp. 101-116, 2017.
- [15] B.W. Kim, H.H. Sung, J.H. Kim, and S.Y. Hong, “Comparison of linear spring and nonlinear FEM methods in dynamic coupled analysis of floating structure and mooring system,” *Journal of Fluids and Structures*, vol.42, pp. 205-227, 2013.
- [16] J.E. Guiterrez-Romero, J. Garcia-Espinosa, B. Servan-Camas, and B. Zamora-Parra, “Non-linear dynamic analysis of the response of moored floating structures,” *Mar. Struct.*, vol.49, pp. 116-137, 2016.
- [17] D.I. Jeong, S.H. Shin, and N. Ku, “Study on the FEM analysis of mooring line for floating multibody system,” *In: Proceedings of the Twenty-Seventh International Ocean and Polar Engineering Conference*, pp. 927-931, 2017.
- [18] D.T. Liu, and W.P. Guo, “Tracking control for an underactuated two-dimensional overhead crane,” *Journal of Applied Research*, vol.10, pp. 597-606, 2012.
- [19] F. Bakhtiari-Nejad, M. Nazemizadeh, and H. Arjmand, “Tracking control of an underactuated gantry crane using an optimal feedback controller,” *Int. J. of Automotive and Mechanical Engineering*, vol.7, pp. 830-839, 2013.
- [20] R. Mehra, S. Satpute, F. Kazi, and N.M. Singh, “Geometric-PBC based control of 4-DOF underactuated overhead crane system,” *In: 21st International Symposium on Mathematical Theory of Networks and Systems*, pp. 1232-1237, 2014.
- [21] Y. Sun, W. Li, D. Dong, X. Mei, and H. Qiang, “Dynamics analysis and active control of a floating crane,” *Tehnicki vjesnik*, vol.22, no.6, pp. 1383-1391, 2015.
- [22] M. Nam, J. Kim, J. Lee, J. Kim, D. Lee, and J. Lee, “Cooperative control system of the floating cranes for the dual lifting,” *Int. J. Naval Architecture and Ocean Engineering*, vol.10, no.1, pp. 95-102, 2018.
- [23] A.A. Shabana, *Computational dynamics*. John Wiley & Sons, New York, 1994.
- [24] F.M.L. Amirouche, *Computational methods in multibody dynamics*. Prentice Hall, 1992.
- [25] A.A. Shabana, *Dynamics of multibody systems*. Cambridge University Press, New York, 1998.
- [26] A.A. Shabana, “Flexible multibody dynamics: review of past and recent developments,” *Multibody System Dynamics*, vol. 1, pp. 189-222, 1997.
- [27] C. Lacoursière, “Ghosts and machines : regularized variational methods for interactive simulations of multibodies with dry frictional contacts,” Umeå

- university, 2007.
- [28] W.J. Book, "Recursive Lagrangian dynamics of flexible manipulator arms," *The International Journal of Robotic Research*, vol. 3, pp. 87-101, 1984.
 - [29] K. Changizi and A.A. Shabana, "A recursive formulation for the dynamic analysis of open loop deformable multibody systems," *Journal of Applied Mechanics*, vol. 55, no. 3, pp. 687-693, 1988.
 - [30] M.S. Pereira and P.L. Proenca, "Dynamic analysis of spatial flexible multibody systems using joint co-ordinates," *International Journal for Numerical Methods in Engineering*, vol. 32, no. 8, pp. 1799-1812, 1991.
 - [31] R. Featherstone, *Rigid body dynamics algorithms*. Springer, New York, 2008.
 - [32] J. M. Wendlandt and J. E. Marsden, "Mechanical integrators derived from a discrete variational principle," *Phys. D Nonlinear Phenom.*, vol. 106, no. 3-4, pp. 223-246, Aug. 1997.
 - [33] J. E. Marsden and M. West, "Discrete mechanics and variational integrators," *Acta Numer. 2001*, vol. 10, pp. 357-514, 2001.
 - [34] A. Lew, "Variational time integrators in computational solid mechanics," vol. 2003, 2003.
 - [35] S. H. Ham, M. I. Roh, H. W. Lee, and S. Ha, "Multibody dynamic analysis of a heavy load suspended by a floating crane with constraint-based wire rope," *Ocean Eng.*, vol. 109, pp. 145-160, 2015.
 - [36] F. Crivelli, *The Störmer-Verlet method*. Swiss Federal Institute of Technology, Zurich, 2008.
 - [37] E. Hairer, C. Lubich, and G. Wanner, "Geometric numerical integration illustrated by the Störmer-Verlet method," *Acta Numer.*, vol. 12, 2003.
 - [38] J. Baumgarte, "Stabilization of constraints and integrals of motion in dynamical systems," *Comput. Methods Appl. Mech. Eng.*, 1972.
 - [39] E. Eich and M. Hanke, "Regularization methods for constrained mechanical multibody systems," *ZAMM - J. Appl. Math. Mech. / Zeitschrift für Angew. Math. und Mech.*, vol. 75, no. 10, pp. 761-773, 1995.
 - [40] O.A. Bauchau, *Flexible multibody dynamics*. Springer, New York, 2011.
 - [41] M. Berzeri and A. A. Shabana, "Development of simple models for the elastic forces in the absolute nodal co-ordinate formulation," *J. Sound Vib.*, vol. 235, no. 4, pp. 539-565, 2000.
 - [42] A. A. Shabana, *Dynamics of multibody systems*. Cambridge University Press, 2005.
 - [43] S.H. Ham, "Integrated simulation method based on multibody dynamics for production design verification in ships and offshore structures," Seoul National

University, 2018.

- [44] S.H. Ham, M.I. Roh, and J.W. Hong, "Dynamic effect of a flexible riser in a fully connected semisubmersible drilling rig using the absolute nodal coordinate formulation," *J. Offshore Mech. Arct. Eng.*, vol. 139, 2017.
- [45] K.P. Park, S.H. Ham, and C.Y. Lee, "Application and validation of production planning simulation in shipbuilding," *Ocean Engineering*, vol. 114, pp. 154-167, 2016.
- [46] B. Ronen, "Faking dynamics of ropes and springs," *IEEE Comput. Graph. Appl.*, vol. 17, pp. 31-39, 1997.
- [47] C.E. Smith, *Applied mechanics, statics*. Wiley, 1982.
- [48] T. Möller and B. Trumbore, "Fast, minimum storage ray-triangle intersection," *Journal of Graphic Tools*, vol. 2, no. 1, pp. 21-28, 1997.
- [49] J.I. Gobat and M.A. Grosenbaugh, "Time-domain numerical simulation of ocean cable structures," *The Ocean Engineering*, vol. 33, pp. 1373-1400, 2006.
- [50] F.P. Bowden and D. Tabor, *The friction and lubrication of solids*. Clarendon Press, 2001.
- [51] P. Song, P. Kraus, and V. Kumar, "Analysis of rigid body dynamic models for simulation of system with frictional contacts," *Journal of Applied Mechanics*, vol. 68, pp. 118-128, 2001.
- [52] C.K. Choi and H.H. Yoo, "A dry friction model to realize stick for simulation of the system with friction and accuracy verification of the friction model," *Trans. Korean Soc. Noise Vib. Eng.*, vol. 22, no. 8, pp. 748-755, 2012.
- [53] R. Taylor and P. Valent, *Design guide for drag embedment anchors*. Naval Civil Engineering Laboratory (USA), TN No N-1688, 1984.
- [54] W. Blajer, R. Seifried, and K. Kolodziejczyk, "Servo-constraint realization for underactuated mechanical systems," *Arch. Appl. Mech.*, vol. 85, pp. 1191-1207, 2015.
- [55] Y. Yang, *Numerical methods for the inverse dynamics simulation of underactuated mechanical systems*. KIT Scientific Publishing, 2017.
- [56] Y. Liu and H. Yu, "A survey of underactuated mechanical systems," *IET Control Theory and Applications*, vol. 7, no. 7, pp. 921-935, 2013.
- [57] A. Zelei and G. Stepan, "Case studies for computed torque control of constrained underactuated systems," *Mechanical Engineering*, vol. 56, no. 1, pp. 73-80, 2012.
- [58] W. Blajer and K. Kolodziejczyk, "Control of underactuated mechanical systems with servo-constraints," *Nonlinear Dyn.*, vol. 50, pp. 781-791, 2007.
- [59] R. Seifried and W. Blajer, "Analysis of servo-constraint problems for underactuated multibody systems," *Mech. Sci.*, vol. 4, pp. 113-129, 2013.

- [60] S.H. Ham, M.I. Roh, and H.W. Lee, "Simulation of load lifting with equalizers used in shipyards," *Automation in Construction*, vol. 61, pp. 98-111, 2016.
- [61] R. Altmann and J. Heiland, "Simulation of multibody systems with servo constraints through optimal control," *Multibody System Dynamics*, vol. 40, pp. 75-98, 2017.
- [62] T. Heyden and C. Woernle, "Dynamics and flatness-based control of a kinematically undetermined cable suspension manipulator," *Multibody System Dynamics*, vol. 16, pp. 155-177, 2006.
- [63] W. Blajer and K. Kolodziejczyk, "A geometric approach to solving problems of control constraints: Theory and a DAE framework," *Multibody System Dynamics*, vol. 11, pp. 343-364, 2004.
- [64] U.M. Ascher and L.R. Petzold, *Computer methods for ordinary differential equations and differential-algebraic equations*. SIAM: Society for Industrial and Applied Mathematics 1998.
- [65] B.W. Kim, H.G. Sung, S.Y. Hong, and H.J. Jung, "Finite element nonlinear analysis for catenary structure considering elastic deformation," *Comput. Model. Eng. Sci.*, vol. 63, pp. 29-45, 2010.
- [66] J.M.J. Journee and W.W. Massie, *Offshore Hydrodynamics*. Lecture Note, Delft University of Technology, Denmark, 2001.

국문 초록

블록 탑재 자동화 및 시뮬레이션 고도화를 위한 와이어 로프 접촉 모델 및 크레인 제어 방법

선박 및 해양구조물은 여러 개의 블록을 탑재하여 건조된다. 블록의 탑재 작업을 수행 시 안전을 위해 사전에 물리 기반 시뮬레이션을 통해 발생할 수 있는 위험성을 미리 파악하는 것이 요구된다. 또한, 실제 작업의 제어는 수작업으로 이루어지는데, 보다 안전하고 효율적인 탑재 작업을 위해 크레인의 제어 자동화 방법에 대한 연구가 필요하다. 본 연구에서는 기존의 시뮬레이션에서 모사할 수 없었던 와이어 로프와 블록 간의 간섭이나 해상 크레인과 계류 시스템 (mooring system) 의 연계 해석에 대하여 연구를 수행한다. 그리고 블록 탑재 자동화를 위한 복잡한 장비를 포함한 크레인의 제어 방법을 제안하였다.

블록 탑재 작업의 물리 기반 시뮬레이션 수행 시 필요한 중요한 요소 중 하나는 다물체계 (multibody) 동역학을 기반으로 한 거동 해석이다. 여러 개의 강체 (rigid body) 들이 관절 (joint) 로 연결되어 이루어진 크레인의 운동 해석 뿐만 아니라, 계류 라인과의 완전한 연계 해석을 위해 유연체 (flexible body)

와의 통합된 운동방정식을 구성하는 것이 필요하다. 이를 위해 DELE 를 선택하여 1 차원 빔 (beam) 과 강체 간의 관절을 비롯한 통합 운동 방정식을 유도하였다.

블록을 탑재하기 위해서 사용되는 크레인은 여러 개의 와이어 로프를 통해 블록을 지탱하며, 해상 크레인의 경우 계류 라인을 통해 위치를 유지하게 된다. 따라서, 탑재 작업 시 일어나는 다양한 현상을 모사하기 위해서는 와이어 로프 및 유연체에 대한 정확하고 효율적인 모델링이 필수적이다. 탑재 시 블록과의 간섭을 고려하기 위해서 구속 조건 기반 와이어 로프 (constraint-based wire rope) 모델을 도입했다. 이를 통해 실제 와이어 로프의 특성인 인장, 구부러짐, 그리고 비틀림을 모델링할 수 있으며, 물체와의 접촉이나 도르래 등과 같은 복잡한 현상도 효율적으로 표현할 수 있다. 계류 라인의 경우, 자체의 동적 거동과 무게에 의한 영향을 고려하기 위해 1 차원 빔으로 나타낸 유연체로 모델링하였다.

본 연구에서는 앞에서 제안한 와이어 로프 모델을 통해 작업 중 일어날 수 있는 타 물체와의 상호 작용을 모델링하였다. 블록의 턴오버 작업에서 블록과 와이어 로프 간의 간섭 및 마찰과 같은 상호 작용을 고려하기 위해서 접촉, 슬라이딩, 마찰 모델로 이루어진 알고리즘을 제안하였다. 먼저, 접촉 모델에서는

와이어 로프와 블록 간의 접촉을 탐지하고 접촉 점에서의 힘을 계산한다. 슬라이딩 모델에서는 접촉이 일어난 경우 와이어 로프 방향, 그리고 물체의 엣지 (edge) 방향으로 미끄러지는 거동을 각각 모사하며, 마찰 모델을 통해 정지 마찰력과 운동 마찰력의 영향을 계산한다. 한편, 유연체로 모델링된 계류 라인과 해저면의 접촉은 계류 라인의 위치와 기울기를 제한하는 두 종류의 구속 조건을 통해 모델링하였다.

본 연구에서는 블록 탑재 작업의 크레인 자동 제어를 위한 방법을 제시하였다. 블록의 궤적 추종 제어 (trajectory tracking control) 을 위해 servo constraint 라는 개념을 도입하였으며, 이를 복잡한 크레인 시스템에 적용할 수 있는 index reduction 방법을 적용하였다. 그리고 이를 갠트리 크레인과 해상크레인에 적용하여 후크 (hook) 및 이퀄라이저 (equalizer) 가 모두 포함된 복잡한 시스템의 제어를 위한 방법을 제시하였다.

제안한 모델의 유효성을 검증하기 위해 각 모델을 해석해 및 타 상용 소프트웨어의 결과와 비교하였다. 블록과 와이어 로프의 간섭 알고리즘은 각 모델을 해석해 등을 통해 검증하였으며, 계류 라인은 상용 소프트웨어인 OrcaFlex 와의 비교를 수행하였다. 그리고 제안한 제어 알고리즘을 통해 블록이 주어진 궤적을 잘 추종하는지 확인하였다.

제안한 모델들은 각각 자체적인 모듈로써 개발이 되었으며, 이는 기존의 다물체계 동역학 기반 해석 프로그램에 통합되었다. 이를 사용하여 블록의 간섭을 고려한 턴오버 작업, 해상크레인과 계류 시스템의 연계 해석을 통한 블록의 리프팅 작업, 그리고 갠트리 크레인과 해상크레인의 자동 제어를 통한 블록 탑재 작업의 해석을 수행하였다. 각각의 해석을 통해 본 연구에서 개발한 모듈들이 성공적으로 적용될 수 있음을 확인하였다. 향후에는 실험이나 HILS 환경 구축 등을 통해 개발한 모델의 추가적인 검증을 수행할 계획이다.

Keywords: 블록 탑재 작업; 크레인; 물리 기반 시뮬레이션; 다물체 동역학; 제약 조건 기반 와이어 로프; 간섭; 마찰 접촉; 계류 시스템; 해저면 접촉; Underactuated system; 제어;

Student number: 2014-22655